DIPLOMARBEIT
Master's Thesis

Coupling multiscale X-ray physics and micromechanics for composition and elasticity determination from micro-CT data, by example of femur from OVX and sham rats

Verbindung von Röntgenphysik und Mikromechanik zwecks Bestimmung von Zusammensetzung und Elastizität von Knochen aus Mikro-CT Bildern, am Beispiel von Oberschenkeln von OVX- und Sham-Ratten

ausgeführt zum Zwecke der Erlangung des akademischen Grades
eines Diplom-Ingenieurs/ einer Diplom-Ingenieurin

unter der Leitung von

(Betreuer/-in) Univ.Prof. Dipl.-Ing. Dr.techn. Christian Hellmich
und
Dipl.-Ing. Viktoria Vass

Inst.Nr.: E202

Institut für Mechanik der Werkstoffe und Strukturen

eingereicht an der Technischen Universität Wien
Fakultät für Bauingenieurwesen

von

(Verfasser/-in) Patricia Sofie Hasslinger
Matr.Nr.: 0636931
Gentzgasse 129/1/42, 1180 Wien

Wien, am 05.03.2015

Abstract

Post-menopausal osteoporosis is a progressiv skeletal disorder expressed by pathophysiological alterations in the bone tissue resulting from a lack of oestrogen. Particularly in the early stages of menopause, these changes can be mimicked by the 'OVX rat model' inducing the hormone deficiency by ovariectomy (OVX). Due to its high resolution, micro-computed tomography (micro-CT) has become a major tool in quantifying the impairment of bone mass and microarchitecture in rodents of preclinical studies. Those histomorphometric analyses of the bone structure are usually based on the statistical evaluation of the three-dimensional CT "images".
The method used in this work directly connects the obtained grey values to scientifically established X-ray attenuation coefficients, and additionally considers the heterogeneous conditions within the voxel, which in case of bone tissue consists of the elementary compounds, water, mineral and organics. Taking into account given mineral-to-organic ratios of a previous osteoporosis-study, the X-ray energy applied during the CT scans can be identified, which concludes to the spatial distribution of the elementary compounds within the voxel and the voxel-specific bone densities. These results serve as input parameters for a multiscale homogenization scheme which, allowing for the respective stiffnesses of the bone's single constituents, as well as their morphologies, leads to the voxel-specific elastic material properties. This analytical method might further enhance a standardised, precise evaluation of the bone structure in respect to post-menopausal osteoporosis research.

Kurzfassung

Postmenopausale Osteoporose ist eine progressive skeletale Erkrankung, die auf Abnahme des Östrogenspiegels zurückzuführen ist und sich durch pathophysiologische Veränderungen im Knochengewebe ausdrückt. Insbesondere in früheren Stadien der Menopause können diese durch das 'OVX rat model' beschrieben werden, welches den Hormonmangel durch Ovariektomie (OVX) induziert. Um den Abbau der Knochenmasse und der Mikroarchitektur in Nagetieren präklinischer Studien zu erfassen, wird aufgrund der hohen Auflösung die Micro-Computertomographie (Mikro-CT) herangezogen. Die statistische Auswertung der dreidimensionalen CT "Bilder" bildet hierbei üblicherweise die Grundlage für die histomorphologischen Analysen der Knochenstruktur.
Die in dieser Arbeit angewandte Methode verknüpft die erhaltenen Grauwerte mit wissenschaftlich etablierten, materialspezifischen Röntgenstrahlabschwächungen und berücksichtigt überdies die heterogenen Bedingungen innerhalb eines Voxels, der sich im Knochengewebe aus den elementaren Bestandteile, Wasser, Mineral und organischer Substanz, zusammensetzt. Unter zusätzlicher Verwendung von gegebenen Verhältnissen zwischen Mineral und organischer Substanz aus einer vorhergehenden Osteoporose-Studie, kann die Röntgenstrahlenergie während der Scanvorgänge identifiziert werden, die auf die räumliche Verteilung der elementaren Komponenten innerhalb des Voxels und die voxel-spezifischen Knochendichten rückschließen lässt. Diese Ergebnisse dienen als Eingangsparameter für ein Multiskalen-Homogenisierungsschema, das unter Berücksichtigung der Steifigkeiten der einzelnen Knochen-Komponenten und ihrer Morphologie letztendlich auf die voxel-spezifischen elastischen Materialeigenschaften führt. Diese analytische Methode mag eine gute Ausgangsbasis für eine standardisierte, präzise Bewertung der Knochenstruktur hinsichtlich Osteoporose-Forschung schaffen.

Acknowledgement

First and foremost, I express my sincere gratitude to my supervisor Univ.-Prof. Dipl.-Ing. Dr.techn. Christian Hellmich, who has supported me throughout the thesis with his knowledge and guidance. Besides, Dipl.-Ing. Viktoria Vass contributed significantly to the development of this thesis and was always on hand with help and advice. In addition, I am thankful to Dr. Romane Blanchard and Dipl.-Ing. Alexander Dejaco for providing the basis for my calculations.
However, this research was only made possible through the collaboration with Assoc.-Prof. Dr. Paolo Gargiulo from Landspitali University Hospital Iceland, and with Dr. Gissur Örlygsson from Innovation Center Iceland, who furnished the CT images and always replied to my requests very fast and in great detail.
Considering the choice of the topic, I am very thankful to my boyfriend who is working in the medical field and encouraged me to pursue a thesis at the 'Institute for mechanics of materials and structures' bringing my focus as a civil engineering student into the biomedical field which always fascinated me.
In addition, special thanks is due to my parents for their emotional and financial support, in particular to my father who motivated me to seize a technical field of study and always let me benefit from his knowledge, and to my mother who literally 'opened new doors' for me. Finally, I wish to thank my two brothers, especially my older one, whom I always admired for mastering his life so effortlessly.

Table of Contents

1 Introduction **1**

2 Paper entitled 'Coupling multiscale X-ray physics and micromechanics for composition and elasticity determination from micro-CT data, by example of femur from OVX and sham rats', to be submitted to the International Journal for Computational Methods in Engineering Science and Mechanics **3**

2.1 Abstract 4

2.2 Introduction 5

2.3 Materials and Methods 7

2.3.1 Animal model and sample preparation 7

2.3.2 Micro-CT evaluation procedure I: Conversion of CT grey values to energy-dependent attenuation coefficients, based on air and water characteristics 8

2.3.3 Micro-CT evaluation procedure II: Identification of applied X-ray energy and of extracellular bone mass density, based on intravoxel attenuation average rule 11

2.3.4 Micro-CT evaluation procedure III: Translation of voxel-specific composition into voxel-specific elastic properties 15

2.4 Results 18

2.5 Discussion 30

3 Summary and future outlook **32**

A Figures of all rat stacks **35**

B Analysis of variance (ANOVA) **41**

C Matlab Codes **42**

C.1 Attenuation coefficients of air, water, collagen and hydroxyapatite as functions of the X-ray energy 42

C.2 Probability density functions of the attenuation-related grey values of the sham rats 46

C.3 Probability density functions of the attenuation-related grey values of the OVX rats 48
C.4 Applied X-ray energy, a and b values and densities and attenuation coefficients of bone 50
C.5 Probability density functions of the attenuation coefficients of the sham and OVX rats 55
C.6 Voxel-specific volume fractions 57
C.7 Voxel-specific elastic properties for sham and OVX rats 60
C.7.1 Calculation of the bone stiffness of the ultrastructure 68
C.7.2 Homogenization of wet collagen 70
C.7.3 Homogenization of fibrils 71
C.7.4 Homogenization of extrafibrillar space 72
C.7.5 Homogenization of ultrastructure 74
C.8 Color images for the maps of f_{HA} (sham and OVX rats) 75
C.9 Color images for the maps of E_1 (sham and OVX rats) 79
C.10 Color images for the maps of E_3 (sham and OVX rats) 83
C.11 Color images for the maps of G_{12} (sham and OVX rats) 87
C.12 Color images for the maps of ν_{12} (sham and OVX rats) 91
C.13 Color images for the maps of ν_{13} (sham and OVX rats) 95

Bibliography **99**

List of Figures

1 Probability density function of attenuation-related grey values of a sham rat femur 8

2 X-ray attenuation coefficients of air, water, collagen and hydroxyapatite as functions of the photon energy, according to NIST-database on `http://physics.nist.gov/PhysRefData/XrayMassCoef/cover.html` (Hubbell and Seltzer, 1996); Searle, 1934; Eastoe, 1955; Bolz and Tuve, 1973; Lees, 1987 9

3 Identification of the applied applied X-ray energy and of its role as argument in the concave function for the water volume fraction in the "average" bone voxel, as given in Eq. (11) 13

4 Multiscale homogenization scheme of the bone ultrastructure: four-scale micromechanical model: (a) RVE of wet collagen; (b) RVE of mineralized fibril; (c) RVE of extrafibrillar space; (d) RVE of extracellular bone matrix – bone ultrastructure; (e_1, e_2: transverse material directions; e_3: axial material direction) (Morin and Hellmich, 2014) . 15

5 Probability density functions of attenuation-related grey values: (a)-(j) sham rat 1-10 19

6 Probability density functions of attenuation-related grey values: (a)-(j) OXV rats 1-10 20

7 Probability density functions of attenuation coefficients: (a)-(j) sham rats 1-10 22

8 Probability density functions of attenuation coefficients: (a)-(j) OVX rats 1-10 23

9 (a), (b) Line constants a and b relating grey values to attenuation coefficients, as functions of the photon energy (c) Water volume fractions in the "average" bone voxel, as functions of the photon energy . 24

10 Voxel-specific material parameters of sham rat 6: (a) Volume fractions, (b) Stiffness tensor components, (c) Young's and shear moduli, (d) Poisson's ratios 25

11 Voxel-specific material parameters of OVX rat 6: (a) Volume fractions, (b) Stiffness tensor components, (c) Young's and shear moduli, (d) Poisson's ratios 26

12 Distribution of the mineral volume fraction and of the material parameters within the distal femur of sham rat 6 under specification of the bone threshold, landmark and maximum values 28
13 Distribution of the mineral volume fraction and of the material parameters within the distal femur of OVX rat 6 under specification of the bone threshold, landmark and maximum values 29
14 Stiffness tensor at the apparent photon energy against grey values: (a)-(j) sham rats 1-10 35
15 Stiffness tensor at the apparent photon energy against grey values: (a)-(j) OVX rats 1-10 36
16 Young's and shear moduli at the apparent photon energy against grey values: (a)-(j) sham rats 1-10 37
17 Young's and shear moduli at the apparent photon energy against grey values: (a)-(j) OVX rats 1-10 38
18 Poisson's ratios at the apparent photon energy against grey values: (a)-(j) sham rats 1-10 39
19 Poisson's ratios at the apparent photon energy against grey values: (a)-(j) OVX rats 1-10 40

List of Tables

1 Landmark and threshold grey values of the sham rats 18
2 Landmark and threshold grey values of the OVX rats 18
3 Line constants a and b, as well as attenuation coefficients and densities of the bone tissue at the photon energy of 14 [keV] (sham) 18
4 Line constants a and b, as well as attenuation coefficients and densities of the bone tissue at the photon energy of 14 [keV] (OVX) 21
5 Material parameters $E_{excel,1}$, $E_{excel,3}$ and $G_{excel,12}$ in [GPa], and $\nu_{excel,12}$ and $\nu_{excel,13}$ in [-] of the bone threshold, landmark and maxium values for the sham rats 27
6 Material parameters $E_{excel,1}$, $E_{excel,3}$ and $G_{excel,12}$ in [GPa], and $\nu_{excel,12}$ and $\nu_{excel,13}$ in [-] of the bone threshold, landmark and maxium values for the OVX rats 27
7 ANOVA for the most frequently occurring mineral volume fraction of sham and OVX rats 41
8 ANOVA for the bone grey values $GV > GV_{thr}$ of sham and OVX rats 41
9 ANOVA for the most frequently occurring bone grey values of sham and OVX rats 41
10 ANOVA for the most frequently occurring bone attenuation-coefficient of sham and OVX rats 41
11 ANOVA for the most frequently occurring axial Young's moduli of sham and OVX rats 41

1 Introduction

Osteoporosis is a progressive skeletal disorder characterised by a systematic impairment of bone mass and microarchitecture causing an increasing bone fragility. The changes of bone tissue occur as a result of oestrogen de-ficiency and therefore predominantly affect post-menopausal women (Müller, 2005; Sambrook and Cooper, 2006; Rachner et al., 2011; Govindarajan et al., 2014; Liu et al., 2014).
During the early stages of post-menopausal osteoporosis, the ovarian hormone deficiency-induced bone loss can be mimicked by the ovariectomized (OVX) rat model which - due to similar pathophysiological features - is the most prevalent and, considering their short generation time, the most efficient animal model for osteoporosis research, besides mice (Kalu, 1991; Thompson et al., 1995; Francisco et al., 2011).
Due to technical advances in scanner equipment which enabled increasing spatial and temporal resolution, the micro-computed tomography (micro-CT) has become a major tool in preclinical investigations of osteoporosis in small animals, especially in vivo and in vitro (Holdsworth and Thornton, 2002; Kapadia et al., 1998; Schambach et al., 2010). The high resolution of the three-dimensional CT "images" provides access to an accurate assessment of the bone structure in the rodents.
In the course of an OVX-study the measured parameters derived from the histomorphometry of the investigated bone usually include the bone mineral density (BMD) and the bone mineral content (BMC) and/or the bone/tissue volume (BV/TV), the trabecular separation (Tb.Sp), the trabecular number (Tb.N), the trabecular thickness (Tb.Th), the structure model index (SMI) and the connectivity density (ConnD) (Fanti et al., 1998; Laib et al., 2000; Borah et al., 2001; Wang et al., 2001; Lesclous et al., 2004; Campbell et al., 2008; Saito et al., 2009; Donnelly, 2011; Francisco et al., 2011; Böcker et al., 2014; Govindarajan et al., 2014; Yang et al., 2014).
The underlying image data processing is usually based on a statistical evaluation of the grey values by defining material thresholds and landmarks (Taleb-Ahmed et al., 2003; Tabor and Latała, 2014). However, these voxel-specific grey values are actually in linear relation with the X-ray attenuation coefficient of the material defining the particular voxel (Skyscan, 2010; Fritsch et al., 2011). The X-ray attenuation coefficient describes the decrease of X-ray beam intensity per length of pervaded matter and is a function of the X-ray energy. Consequently, intersection and slope defining the linear relation between grey values and attenuation coefficients depend on the applied X-ray energy during the scanning as well (Czenek et al., 2014).

With a novel method introduced by Czenek et al. (2014), both line parameters can be gained from two of the altogether three grey value landmarks assigned to the identified materials, air, water and bone, taking up most of the scanned spatial area, and their respective attenuation coefficients published by the National Institute of Standards and Technology (Hubbell and Seltzer, 1996). Applying the volume average rule for the X-ray attenuation coefficient of a composite material (Jackson and Hawkes, 1981,Crawley et al., 1988; Hellmich et al., 2008) to the bone tissue consisting of the elementary components, hydroxyapatite, collagen and water (Blanchard et al., 2013), and utilization of the mean mineral to organic ratios either for the sham rats or the OVX rats, given in Kim et al.'s ashing experiments (2009) on femurs, delivers the volume fractions of water as functions of the X-ray energy. The clue exerted for the interpretation of these obtained concave curves, each representing a different CT scan, is that at their maxima one unique value for the X-ray energy exists, yielding scalar quantities for the intersection and the slope (Czenek et al., 2014).

These findings enable us to access voxel-specific volume fractions and bone densities, and hence the voxel-specific mechanical behaviour by employing the Mori-Tanaka homogenization scheme (Mori and Tanaka, 1973; Benveniste, 1987) from the nanostructure with its elementary components exhibiting known elastic properties and morphologies, up to the ultrastructural scale predetermined by the prevalent voxel size of the three-dimensional CT "images" (Hellmich et al., 2004a; Fritsch and Hellmich, 2007; Fritsch et al., 2009a; Morin and Hellmich, 2014).

This method investigates the pathophysiological alterations within the bone ultrastructure due to osteoporosis by evaluation of the bone densities and material parameters of the OVX rats compared to their sham-operated counterparts.

2 Paper entitled 'Coupling multiscale X-ray physics and micromechanics for composition and elasticity determination from micro-CT data, by example of femur from OVX and sham rats', to be submitted to the International Journal for Computational Methods in Engineering Science and Mechanics

Patricia Hasslinger[a], Viktoria Vass[a], Alexander Dejaco[a], Romane Blanchard[a,b], Gissur Örlygsson[c], Paolo Gargiulo[d,e], Christian Hellmich[a]

[a]*Institute for Mechanics of Materials and Structures, Vienna University of Technology, Austria*
[b]*Institute of Musculoskeletal Science, University of Melbourne, Australia*
[c]*Department of Materials, Biotechnology and Energy, Innovation Center Iceland*
[d]*Department of Sience, Landspitali University Hospital, Iceland*
[e]*REModel Lab, The Blood bank, Landspitali University Hospital, Iceland*

Contributions of authors:

Patricia Hasslinger co-developed the method, conducted the research, performed the computations, illustrated and documented the results.

Viktoria Vass, Alexander Dejaco, and Romane Blanchard supported the programming development; Viktoria Vass also supported method development and paper writing.

Gissur Örlygsson and Paolo Gargiulo provided suggested research topic and provided microCT data.

Christian Hellmich supervised the research progress, co-developed the method, and supported result documentation and paper writing.

2.1 Abstract

Bone micro-CT scanning may not only serve as key to morphometric analyses revealing characteristics of collectives comprising a large amount of voxels, but this highly popular imaging technique also provides information on chemical and mechanical characteristics of the matter contained in each and every voxel representing bone tissue. For the latter goal, we here combine basics of X-ray physics, such as the energy- and chemistry-dependence of attenuation coefficients and the average rule they obey to, with results from ashing and drying tests performed on whole bones (Kim et al., 2009). This provides voxel-specific mineral, organic, and water volume fractions within 8 micron sized voxels representing femora from 10 sham and 10 OVX rats. Additional use of a micro elastic model (Morin and Hellmich, 2014) delivers rat-specific maps of transversely isotropic elastic components, across the scanned organs. The new method delivers very realistic bone mass densities as independent results, and reveals that certain OVX protocols, such as the one used herein, do not successfully induce osteoporosis-related phenotypes.

2.2 Introduction

Micro-CT imaging has become a key tool in biomedical studies, as they allow for high-resolution, non-destructive investigation of the inner structure of organs, and it has been particularly embraced for studying bone in health, disease, and tissue-engineering-supported regeneration (Laib et al., 2000; Buie et al., 2007; Cancedda et al., 2007; Jones et al., 2007). Standardly, such images are evaluated on the basis of morphometric measures such as bone volume over total volume (BV/TV), trabecular spacing (Tr.Sp.), trabecular number (Trab.N.), or cortical thickness (Ct.Th.) (Buie et al., 2007). Alternatively, micro-CT images provide a basis for Finite Element models (Jaecques et al., 2004). In this context, the question about the material properties to be assigned to the bone elements arises. The most straightforward approach consists of assigning constant properties to all bone elements (Van Rietbergen et al., 1995; Van Rietbergen et al., 1999). On the other hand, more sophisticated approaches account for the dependence of elastic properties on the local material density (Renders et al., 2008; Baca et al., 2008); the latter being approximated by the X-ray attenuation-related grey values of the voxels making up the three dimensional image stack. Corresponding „CT-density"-versus-elasticity relations, however, stay empirical in nature, depending strongly on the settings of the used instruments. Therefore, numerous formulations rather than a generally agreed-on concept, are discussed in the open literature (Wirtz et al., 2000; Cong et al., 2011). During the last seven years, a new strategy for deriving CT-elasticity relations has been proposed and continuously refined (Hellmich et al., 2008; Yosibash et al., 2008; Scheiner et al., 2009; Vuong and Hellmich, 2011; Dejaco et al., 2012; Blanchard et al., 2013; Czenek et al., 2014). Thereby, such relations are not guessed any more, but derived from fundamental laws of X-ray physics and continuum micromechanics, in combination with additional knowledge on the chemistry of the scanned objects. As a common feature of all the aforementioned approaches, the spatial average rule for X-ray attenuation coefficients (Jackson and Hawkes, 1981; Crawley et al., 1988) is employed to retrieve, from the attenuation-related, voxel-specific grey values, voxel-specific compositional information on the matter filling the voxels. Thereafter, this compositional information is used as input for micromechanical models (Hellmich et al., 2004b; Fritsch et al., 2006; Fritsch and Hellmich, 2007; Fritsch et al., 2009b) which translate material composition into elastic properties. Naturally, these meth-

ods appear the more powerful the fewer input informations are needed beyond the standard clinical or micro-CT images themselves. A particularly delicate issue in this context is the normally undisclosed X-ray energy used for scanning, which however, does effect the measurement of X-ray intensities, the basis of the entire suite of processing steps leading in the end to 3D CT images. It is the focus of the present paper, extending a recent contribution in the field of ceramic bone materials to natural bone tissue (Czenek et al., 2014), by example of micro-CT images of femoral bones of OVX and sham rats. With the chemically determined OVX- as well as sham-specific mineral-to-organic ratios determined through ashing experiments by Kim et al. (2009), as the only additional input needed, we derive, in the following, from stacks of OVX and sham rat femur micro-CT images, spatial distributions of mineral, organic, and water contents at micrometer-resolution, together with corresponding elastic properties - together with the X-ray energy used for these images. The paper is completed by discussing the results with respect to earlier findings, including the potentials and limitations of OVX-treatment for osteoporosis simulation in rat models.

2.3 Materials and Methods

2.3.1 Animal model and sample preparation

The micro-CT images used in the present study visualize femurs of 10 ovariectomized (OVX) female Sprague-Dawley rats, and 10 sham-operated rats serving as controls. At the age of six months, the rats were anaesthetized through an injection of 0.2 ml per 100 g body weight, of Hypnorm and Dormicum diluted in water at volume ratios of 1:1:2. Afterwards, they were subject to a "single midline dorsal skin incision" (Hoegh-Andersen et al., 2004), followed by muscle cutting in order to provide access to the ovaries. Thereafter, both ovaries were removed from the rats belonging to the OVX group, while the ovaries were left within the rats of the control group. Then, the muscles were closed by means of one to two stitches on each side, and the skin was sutured through three to four stitches. Six weeks post surgery, the rats were asphyxiated by carbon dioxide, and sacrificed by exsanguination after at least 14 hours of fasting. The femurs were then excised, freed from flesh, and wrapped in saline soaked gauze. They were stored in plastic tubes at $-20°C$ for the time period until CT scanning. For the latter, the bones were first thawed in a refrigerator, and then embedded in a watery solution with 0.9 g NaCl and 0.1 g NaN_3 per 100 ml solution, enclosed in a plastic cylinder. Thereafter, the samples were X-ray scanned in a Phoenix Nanotom S (General Electric Measurement and Control), at a source voltage of 110 kV and a source current of 150 μA, without employing any X-ray filter. Thereby, the scanning modalities were as follows: magnification: 6.25, voxel size: 8.00 μm, rotation step: 0.36°, exposure time: 2000 ms, tube mode: 0, frame averaging number: 3, 1 frame skipped. The obtained projection images were used to reconstruct the investigated three-dimensional objects, by means of the Radon transform as algorithmized in the software datos|x-reconstruction by phoenix|x-ray (Radon, 1917; Beyerer and Puente León, 2002). VGStudio Max 2.0 from Volume Graphics allowed for extraction of stacks of 800 images slices with identical pixel number, visualizing the space from the distal end of the femur to the knee joint.

2.3.2 Micro-CT evaluation procedure I: Conversion of CT grey values to energy-dependent attenuation coefficients, based on air and water characteristics

The X-ray attenuation-related grey values (GV) assigned to the 8 micron sized voxels making up an image stack visualizing bones of one rat, are binned into histograms, which are then normalized, so as to provide probability density functions, as exemplarily shown in Figure 1.

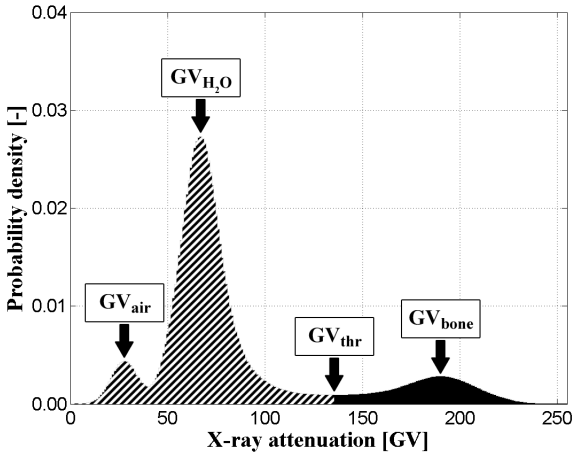

Figure 1: Probability density function of attenuation-related grey values of a sham rat femur

As a rule, these functions exhibit three maxima or peaks, being related to the voxels which are most frequently occurring in the image stack compartments visualizing air, the aforementioned watery solution, and solid bone tissue. These grey values are denoted as GV_{air}, GV_{H_2O}, and GV_{bone}. The increasing density of the matter filling the aforementioned compartments implies $GV_{air} < GV_{H_2O} < GV_{bone}$. The minimum value between GV_{H_2O} and GV_{bone}, denoted as threshold value (GV_{thr}), is used to distinguish the solid bone voxels from all other voxels. These voxels, fulfilling $GV > GV_{thr}$, are subject to the following evaluation procedure described in 2.3.3.

Before, the linear relation between the voxel-specific grey values and the voxel-specific X-ray attenuation coefficients μ, which depend on the chemical composition of the matter filling the voxel and the used photon energy ε, needs to be specified. In other words, the slope $a(\varepsilon)$ and the intersection $b(\varepsilon)$ in the relation (Skyscan,

2010; Fritsch et al., 2011; Blanchard et al., 2013; Czenek et al., 2014)

$$\mu(\varepsilon) = a(\varepsilon) \times GV + b(\varepsilon) \tag{1}$$

need to be determined. Therefore, Eq. (1) is specified for the voxels characterized by GV_{air} and GV_{H_2O}, respectively. This leads to the following system of equations for the unknowns $a(\varepsilon)$ and $b(\varepsilon)$

$$\begin{aligned} \mu_{air}(\varepsilon) &= a(\varepsilon) \times GV_{air} + b(\varepsilon) \\ \mu_{H_2O}(\varepsilon) &= a(\varepsilon) \times GV_{H_2O} + b(\varepsilon) \end{aligned} \tag{2}$$

whereby the attenuation coefficients for air and water, $\mu_{air}(\varepsilon)$ and $\mu_{H_2O}(\varepsilon)$, follow from the respective mass attenuation coefficients μ/ρ available in the database of the National Institute of Standards and Technology (NIST) (Hubbell and Seltzer, 1996) upon input of their chemical compositions [see (Bolz and Tuve, 1973) for air], and from the mass densities ρ_{air}=0,0012 g/cm^3 (Searle, 1934) and ρ_{H_2O}=1 g/cm^3, see Figure 2.

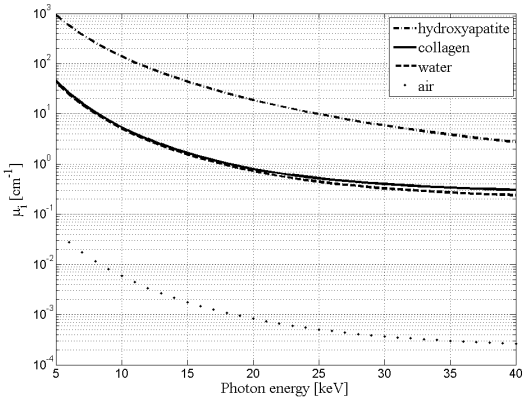

Figure 2: X-ray attenuation coefficients of air, water, collagen and hydroxyapatite as functions of the photon energy, according to NIST-database on `http://physics.nist.gov/PhysRefData/XrayMassCoef/cover.html` (Hubbell and Seltzer, 1996); Searle, 1934; Eastoe, 1955; Bolz and Tuve, 1973; Lees, 1987

Solving the system of Eq. (2) for the unknowns $a(\varepsilon)$ and $b(\varepsilon)$ delivers

$$\begin{aligned} a(\varepsilon) &= [\mu_{H_2O}(\varepsilon) - \mu_{air}(\varepsilon)]/[GV_{H_2O} - GV_{air}] \\ b(\varepsilon) &= [GV_{H_2O} \times \mu_{air}(\varepsilon) - GV_{air} \times \mu_{H_2O}(\varepsilon)]/[GV_{H_2O} - GV_{air}] \end{aligned} \tag{3}$$

The coefficient functions $a(\varepsilon)$ and $b(\varepsilon)$ allow for translation of any grey value found in

the micro-computer tomographs of the investigated rat femurs into corresponding X-ray attenuation coefficients - provided the photon energy is known. Its identification will be dealt with next.

2.3.3 Micro-CT evaluation procedure II: Identification of applied X-ray energy and of extracellular bone mass density, based on intravoxel attenuation average rule

Following the strategy outlined in (Czenek et al., 2014), the photon energy determination rests on an equation which follows from equalizing two independent mathematical expressions for the most frequently occurring X-ray attenuation coefficient in the bone tissue compartment of the investigated images stacks, denoted as μ_{bone}. The first expression stems straightforwardly from specification of Eq. (1) for GV_{bone}, resulting in

$$\mu_{bone}(\varepsilon) = a(\varepsilon) \times GV_{bone} + b(\varepsilon) \tag{4}$$

The second expression is derived from the average rule for the attenuation coefficient μ (Jackson and Hawkes, 1981; Crawley et al., 1988; Hellmich et al., 2008)

$$\mu(\varepsilon) = \sum_{i}^{N_c} \mu_i(\varepsilon) \times f_i \tag{5}$$

whereas μ_i represents the X-ray attenuation coefficient of material constituent i and f_i stands for the corresponding volume; index i runs from 1 through N_C, the total number of constituents within the voxel characterized by attenuation coefficient μ.

The 8x8x8 μm^3-sized bone tissue voxels contain the three elementary components of bone: hydroxyapatite (HA), organics (denoted by suffix "org" - mainly collagen), and water (Buckwalter et al., 1995). Specification of Eq. (5) for these particular constituents yields Eq. (6) (Blanchard et al., 2013)

$$\begin{aligned} \forall\, GV > GV_{thr}: \quad \mu(\varepsilon) \quad &= \quad \mu_{HA}(\varepsilon) \times f_{HA} + \mu_{org}(\varepsilon) \times f_{org} + \mu_{H_2O}(\varepsilon) \times f_{H_2O} \\ &\text{with} \quad f_{HA} + f_{org} + f_{H_2O} = 1 \end{aligned} \tag{6}$$

The attenuation coefficients $\mu_i(\varepsilon)$ are retrieved from the NIST data base (Hubbell and Seltzer, 1996). Based on the chemical formulae of hydroxyapatite and water, $Ca_5(PO_4)_3(OH)$ (Landis, 1995; Fritsch and Hellmich, 2007, Clarke, 2008) and H_2O, this electronic data base delivers their mass attenuation coefficients $(\mu(\varepsilon)/\rho)_i$, $i = HA,\ H_2O,\ col$, so that use of the mass densities ρ_{HA}=3 g/cm^3 (Gong et al., 1964; Lees, 1987) and ρ_{H_2O}=1 g/cm^3 yields the functions depicted in Figure 2. In order to approximate the complex organic matter making up the extracellular bone matrix, we employ the mass density $\rho_{org} = 1,41$ g/cm^3 (Katz and Li, 1973; Lees, 1987),

together with the chemical formula of the amino acid glycine, $C_2H_5NO_2$, which is representative for collagen (Eastoe, 1955; Lodish et al., 2000). The latter, in turn, makes up 90 % of the organic matter in bone (Urist et al., 1983; Lees, 1987; Buckwalter et al., 1995).

The volume fractions f_{HA}, f_{org}, and f_{H_2O} are expected to vary from voxel to voxel within the bony compartments of the investigated rats, and except for Eq. $(6)_2$, no further relation among them can be given. The picture changes, however, if we consider spatial average values over the entire bony compartments rather than local voxel-specific values.

In fact, Kim et al. (2009) performed drying experiments on rat femoral bones, giving access to the organic and mineral weight of the organs, in combination with ashing experiments at 550 degrees Celsius. According to Gong et al. (1964) ashing at such a high temperature leads to volatilizing of not only the entire organic portions of the bones, but also of a certain portion of the mineral, amounting to 1.8 % of the mineral left after the burning process as ash. Accordingly, the experiments of Kim et al. (2009) yield mineral-to-organic mass ratios $\mathcal{R}$ amounting to 0.634 for sham rats, and to 0.618 for OVX rats. Hence, the mineral and organic volume fractions averaged over the bony compartments, which we denote by f_{HA}^{bone} and f_{org}^{bone}, fulfill

$$f_{HA}^{bone} = \mathcal{R} \times \frac{\rho_{org}}{\rho_{HA}} \times f_{org}^{bone} \tag{7}$$

In the following, we approximate the spatial averages over the bony compartments by quantities occurring in the most frequent bone voxel (which would be an identity rather than an approximation for the case of a Gaussian distribution of bony voxels around the peak GV_{bone} seen in Figure 1), so that Eq. (7) would also characterize this most frequently occurring bone tissue voxel. Eq. (7) implies constant volume fractions within the solid subvolume of the most frequently occurring solid voxel,

$$\begin{aligned} f_{HA}^{solid} &= \frac{f_{HA}^{bone}}{f_{HA}^{bone}+f_{org}^{bone}} = \mathcal{R} \times \frac{\rho_{org}}{\rho_{HA}} \times \frac{1}{\mathcal{R}\times\frac{\rho_{org}}{\rho_{HA}}+1} \\ f_{org}^{solid} &= 1 - f_{HA}^{solid} = \frac{1}{\mathcal{R}\times\frac{\rho_{org}}{\rho_{HA}}+1} \end{aligned} \tag{8}$$

These volume fractions give access to an only energy-dependent attenuation coefficient $\mu_{solid}(\varepsilon)$ of the solid matter found in the most frequently occurring bony voxel,

by means of specification of the average rule (5) for two constituents, $i = HA, org$

$$\mu_{solid}(\varepsilon) = f_{HA}^{solid} \times \mu_{HA}(\varepsilon) + \left(1 - f_{HA}^{solid}\right) \times \mu_{org}(\varepsilon) \tag{9}$$

Applying now the attenuation rule again to the entire voxel considered as a mixture of the aforementioned solid and of water, we arrive at

$$\mu_{bone}(\varepsilon) = f_{H_2O}^{bone} \times \mu_{H_2O}(\varepsilon) + \left(1 - f_{H_2O}^{bone}\right) \times \mu_{solid}(\varepsilon) \tag{10}$$

Identification the latter expression with Eq. (4) yields a relation giving access to the X-ray energy ε

$$\begin{array}{l} a(\varepsilon) \times GV_{bone} + b(\varepsilon) \;\; = \;\; f_{H_2O} \times \mu_{H_2O}(\varepsilon) + \left(1 - f_{H_2O}\right) \times \mu_{solid}(\varepsilon) \\ f_{H_2O} = \frac{a(\varepsilon) \times GV_{bone} + b(\varepsilon) - \mu_{solid}(\varepsilon)}{\mu_{H_2O}(\varepsilon) - \mu_{solid}(\varepsilon)} \end{array} \tag{11}$$

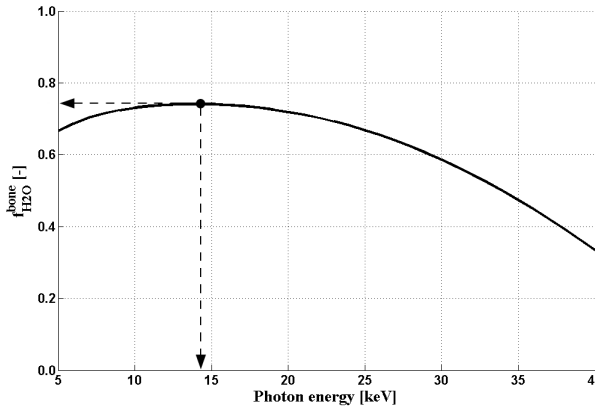

Figure 3: Identification of the applied applied X-ray energy and of its role as argument in the concave function for the water volume fraction in the "average" bone voxel, as given in Eq. (11)

Given the concave nature of this function $f_{H_2O}^{bone} = f_{H_2O}^{bone}(\varepsilon)$ (see Figure 3), the inverse relation $\varepsilon(f_{H_2O})$ assigns, as a rule, to each value of $f_{H_2O}^{bone}$, none or two values for ε, and there exists only one single value for $f_{H_2O}^{bone}$, which is assigned to precisely one value of ε. As only one (average) X-ray energy was used for the CT image stack production, the aforementioned water volume fraction is the one actually occurring - it appears as maximum in the function $f_{H_2O}^{bone}(\varepsilon)$ as defined through Eq. $(11)_2$. The value for ε related to this maximum is the sought, actually used X-ray energy, denoted as $\overline{\varepsilon}$.

This value gives access to the constituent volume fractions occurring in the "aver-

age" bone voxel: the "average" volume fraction of water follows from evaluation of Eq. $(11)_2$ for $\varepsilon = \overline{\varepsilon}$; the remaining voxel volume is filled by mineral and organics, see Eq. $(6)_2$, so that simultaneous use of Eq. $(8)_2$ yields

$$\begin{aligned} f_{org}^{bone}(\overline{\varepsilon}) &= f_{org}^{solid} \times (1 - f_{H_2O}^{bone}(\overline{\varepsilon}) \\ f_{HA}^{bone}(\overline{\varepsilon}) &= 1 - f_{org}^{bone}(\overline{\varepsilon}) - f_{H_2O}^{bone(\overline{\varepsilon})} \end{aligned} \tag{12}$$

These compositional characteristics of the "average" bony voxel holds the key to determination of the properties of any voxel belonging to the bony compartment of the investigated micro-CT image stack: In this context, we follow earlier contributions (Roschger et al., 2008) considering that variations in the attenuation coefficients from one voxel to its neighbors reflect changes in mineralization degree; and that mineral precipitation consumes the ions from the watery solution while not affecting the organic matter within the voxels (Lees, 2003; Morin et al., 2013). Accordingly, we set the organic volume fraction of all bony voxels equal to the f_{org}^{bone}, and determine the voxel-specific mineral and water volume fractions from specialization of Eq. (6) for $\varepsilon = \overline{\varepsilon}$ and for f_{org}^{bone}, yielding

$$\begin{aligned} f_{HA} &= \frac{a(\overline{\varepsilon}) \times GV + b(\overline{\varepsilon}) - f_{org}^{bone}(\overline{\varepsilon}) \times \mu_{org}(\overline{\varepsilon}) - \left(1 - f_{org}^{bone}(\overline{\varepsilon})\right) \times \mu_{H_2O}(\overline{\varepsilon})}{\mu_{HA}(\overline{\varepsilon}) - \mu_{H_2O}(\overline{\varepsilon})} \\ f_{H_2O} &= \frac{a(\overline{\varepsilon}) \times GV + b(\overline{\varepsilon}) - f_{org}^{bone}(\overline{\varepsilon}) \times \mu_{org}(\overline{\varepsilon}) - \left(1 - f_{org}^{bone}(\overline{\varepsilon})\right) \times \mu_{HA}(\overline{\varepsilon})}{\mu_{H_2O}(\overline{\varepsilon}) - \mu_{HA}(\overline{\varepsilon})} \\ f_{org} &= f_{org}^{bone}(\overline{\varepsilon}) \end{aligned} \tag{13}$$

These volume fractions then also allow for voxel-specific determination of the bone tissue mass density, according to

$$\rho_{bone}(\overline{\varepsilon}) = \rho_{HA} \times f_{HA}(\overline{\varepsilon}) + \rho_{org} \times f_{org}^{bone} + \rho_{H_2O} \times f_{H_2O}(\overline{\varepsilon}) \tag{14}$$

2.3.4 Micro-CT evaluation procedure III: Translation of voxel-specific composition into voxel-specific elastic properties

Next, the voxel-specific volume fractions (13) serve as input for an experimentally validated poro-micro-elastic model for extracellular bone matrix (Morin and Hellmich, 2013), cast within the framework of continuum micromechanics (Zaoui, 2002); Dormieux et al., 2006). According to this framework, the elasticity of a piece of matter, located in a material volume called representative volume element - RVE, depends on the elasticity of more or less homogeneous subvolumes within the RVE, called material phases, as well as on their shapes, interactions, and volume fractions. In this line, every voxel is regarded as RVE, with mechanically relevant microstructural characteristics as depicted in Figure 4.

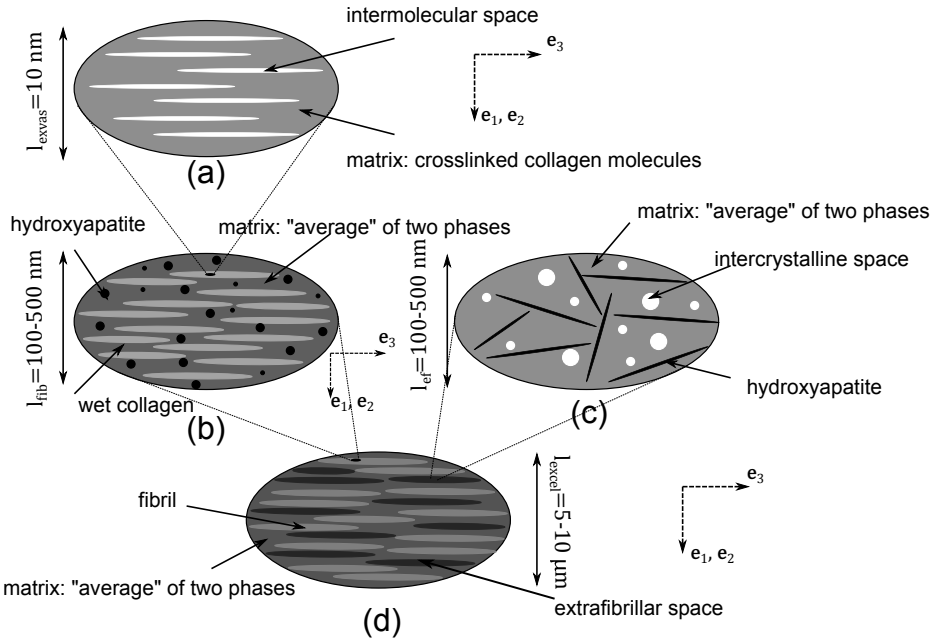

Figure 4: Multiscale homogenization scheme of the bone ultrastructure: four-scale micromechanical model: (a) RVE of wet collagen; (b) RVE of mineralized fibril; (c) RVE of extrafibrillar space; (d) RVE of extracellular bone matrix – bone ultrastructure; (e_1, e_2: transverse material directions; e_3: axial material direction) (Morin and Hellmich, 2014)

In more detail, a voxel represents a piece of extracellular bone matrix, hosting two material phases with elongated cylindrical shape: "mineralized collagen fibrils" and "porous polycrystal in extrafibrillar space". According to the separation-of-scales principle (Zaoui, 2002; Drugan and Willis, 1996), the lineal dimensions of these

phases, i.e. their diameters amounting to some hundred nanometers, need to be much smaller then those of the RVE, namely 8 μm as described in 2.3.1. These phases are entangled and intertwined so that the mathematical relations between phase volume fractions, phase stiffnesses and the elastic properties of the overall RVE follow from a self-consistent homogenization scheme (Hershey, 1954; Morin and Hellmich, 2013)

$$\mathbb{C}_{excel} = \left\{ f_{fib}\mathbb{C}_{fib}\left[\mathbb{I} + \mathbb{P}_{cyl}^{excel} : (\mathbb{C}_{fib} - \mathbb{C}_{ultra})\right]^{-1} + f_{ef}\mathbb{C}_{ef}\left[\mathbb{I} + \mathbb{P}_{cyl}^{excel} : (\mathbb{C}_{ef} - \mathbb{C}_{ultra})\right]^{-1} \right\} : \left\{ f_{fib}\left[\mathbb{I} + \mathbb{P}_{cyl}^{excel} : (\mathbb{C}_{fib} - \mathbb{C}_{ultra})\right]^{-1} + f_{ef}\left[\mathbb{I} + \mathbb{P}_{cyl}^{excel} : (\mathbb{C}_{ef} - \mathbb{C}_{ultra})\right]^{-1} \right\}^{-1} \quad (15)$$

where f_{fib} and f_{ef} denote the volume fractions of the fibrils and the extrafibrillar space (they can be determined from the volume fractions of mineral, organics, and water, as detailed further below), $\mathbb{I}$ denotes the fourth-order identity tensor, with components $I_{ijkl} = 1/2 \times (\delta_{ik}\delta_{jl} + \delta_{il}\delta_{jk})$, whereas the Kronecker delta δ_{ij} is 1 for i = j and zero otherwise, and P_{cyl}^{excel} is the morphology or Hill tensor, accounting for the cylindrical shape of the phases embedded in a fictitious matrix with the elastic properties of the extracellular RVE; and C_{fib} and C_{ef} are the elasticity tensors of the fibrillar and the extrafibrillar space, respectively. They follow from yet additional homogenization steps related to RVEs at lower scales, as depicted in Figure 4.

At these lower scales, "universal", i.e. tissue-independent, phase properties (Hellmich et al., 2004a; Hellmich et al., 2004b; Fritsch and Hellmich, 2007; Morin et al., 2013; Morin and Hellmich, 2014) are encountered at the level of the mechanical elementary constituents: hydroxyapatite, collagen, and water with non-collageneous organics. The elasticity of the hydroxyapatite phase follows from ultrasonic tests of Katz and Ukraincik (1971); that of molecular collagen can be retrieved from Brillouin light scattering tests of Cusack and Miller (1979); while the elasticity of water is known from acoustic tests, such as the ones of Del Grosso and Mader (1972).

The phase volume fractions within all these RVEs can be retrieved, on the basis of general bone composition rules described elsewhere (Hellmich and Ulm, 2002; Vuong and Hellmich, 2011; Morin et al., 2013; Morin and Hellmich, 2013) from the extracellular volume fractions of collagen, mineral, and bone fluid; thereby the mineral volume fraction follows $(13)_1$, volume fraction of collagen amounts to 90 % of the organic volume fraction of 13_3 (Urist et al., 1983); and the rest of the voxel

is filled by bone fluid - water with non-collageneous organic components.

In this contribution, we present the voxel-specific stiffness tensors in terms of the engineering components called Young's and shear moduli, and Possion's ratios (Vuong and Hellmich, 2011). They are based on the compliance tensor, which is the inverse of the stiffness tensor,

$$\mathbb{D}_{excel} = \mathbb{C}_{excel}^{-1} \tag{16}$$

The compliance tensor components then give access to the Young's moduli in transverse and longitudinal directions according to

$$E_{excel,1} = \frac{1}{D_{excel,1111}} \qquad \text{and} \qquad E_{excel,3} = \frac{1}{D_{excel,3333}} \tag{17}$$

to the Poisson's ratios according to

$$\nu_{excel,12} = -D_{excel,1122} \times E_1 \qquad \text{and} \qquad \nu_{excel,13} = -D_{excel,1133} \times E_3 \tag{18}$$

and to the shear modulus according to

$$G_{excel,12} = \frac{E_{excel,1}}{2 \times (1 + \nu_{excel,12})} \tag{19}$$

2.4 Results

All histograms derived from the 20 investigated micro-CT stacks exhibit clearly three peaks, related to air, water, and "average" bone tissue, respectively, see Figures 5 and 6. The histogram-based evaluation of the 10 sham rat micro-CT image stacks delivered air-related grey values between 29 and 33, water-related values between 66 and 71, and "average" bone-related values between 185 and 193, see Table 1. The histogram-based evaluation of the 10 OVX rat micro-CT image stacks delivered air-related grey values between 29 and 33, water-related values between 65 and 72, and "average" bone-related values between 183 and 193, see Table 2.

Table 1: Landmark and threshold grey values of the sham rats

Samples	**1**	**2**	**3**	**4**	**5**	**6**	**7**	**8**	**9**	**10**	**mean**	**STD**
GV_{air}	29	32	29	33	30	32	29	33	31	30	31	1.62
GV_{H_2O}	68	69	69	67	70	66	68	70	69	71	69	1.49
GV_{thr}	134	139	136	134	135	133	128	134	135	138	135	2.99
GV_{bone}	191	188	192	185	186	190	188	187	193	190	189	2.62

Table 2: Landmark and threshold grey values of the OVX rats

Samples	**1**	**2**	**3**	**4**	**5**	**6**	**7**	**8**	**9**	**10**	**mean**	**STD**
GV_{air}	33	30	31	29	31	30	32	29	31	32	31	1.32
GV_{H_2O}	71	68	72	65	72	66	68	69	72	72	70	2.68
GV_{thr}	140	132	136	134	137	128	132	133	134	139	135	3.60
GV_{bone}	193	184	187	183	190	188	186	186	185	193	188	3.50

Table 3: Line constants a and b, as well as attenuation coefficients and densities of the bone tissue at the photon energy of 14 [keV] (sham)

Samples	**1**	**2**	**3**	**4**	**5**	**6**	**7**	**8**	**9**	**10**	**mean**	**STD**
a	0.048	0.051	0.047	0.055	0.047	0.055	0.048	0.051	0.049	0.046	0.050	0.003
b$\cdot(-1)$	1.390	1.617	1.355	1.815	1.402	1.760	1.390	1.667	1.525	1.366	1.529	0.174
μ_{bone}	7.778	7.894	7.630	8.370	7.302	8.701	7.634	7.793	7.982	7.307	7.839	0.436
ρ_{bone}	1.288	1.293	1.281	1.317	1.265	1.333	1.281	1.288	1.298	1.265	1.291	0.021
f_{HA}	0.114	0.116	0.111	0.126	0.105	0.132	0.111	0.115	0.1181	0.1051	0.1154	0.0084
f_{org}	0.145	0.148	0.141	0.159	0.133	0.167	0.141	0.145	0.1496	0.1331	0.1461	0.0107
f_{H_2O}	0.741	0.736	0.748	0.715	0.762	0.701	0.748	0.741	0.7322	0.7618	0.7385	0.0191

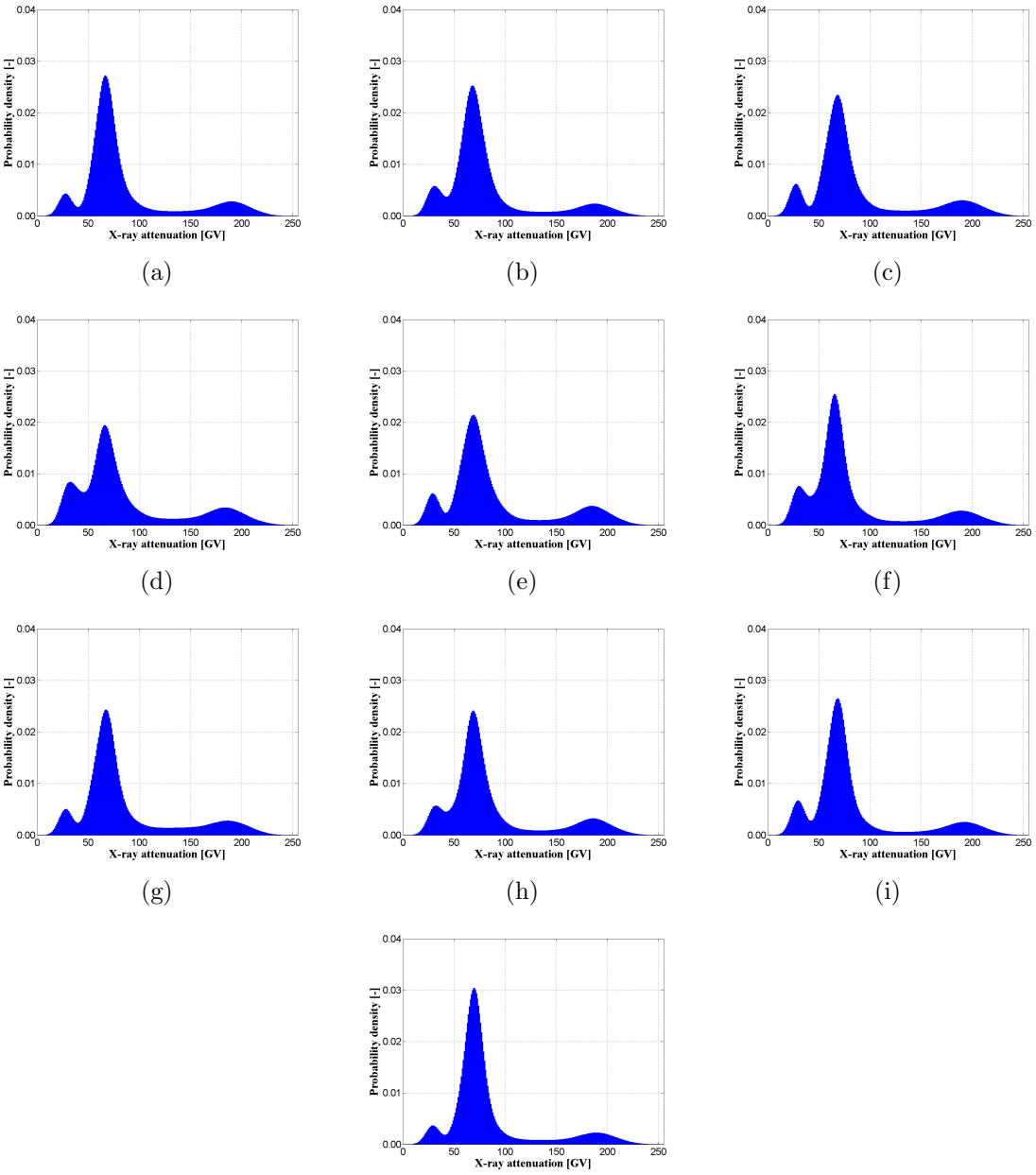

Figure 5: Probability density functions of attenuation-related grey values: (a)-(j) sham rat 1-10

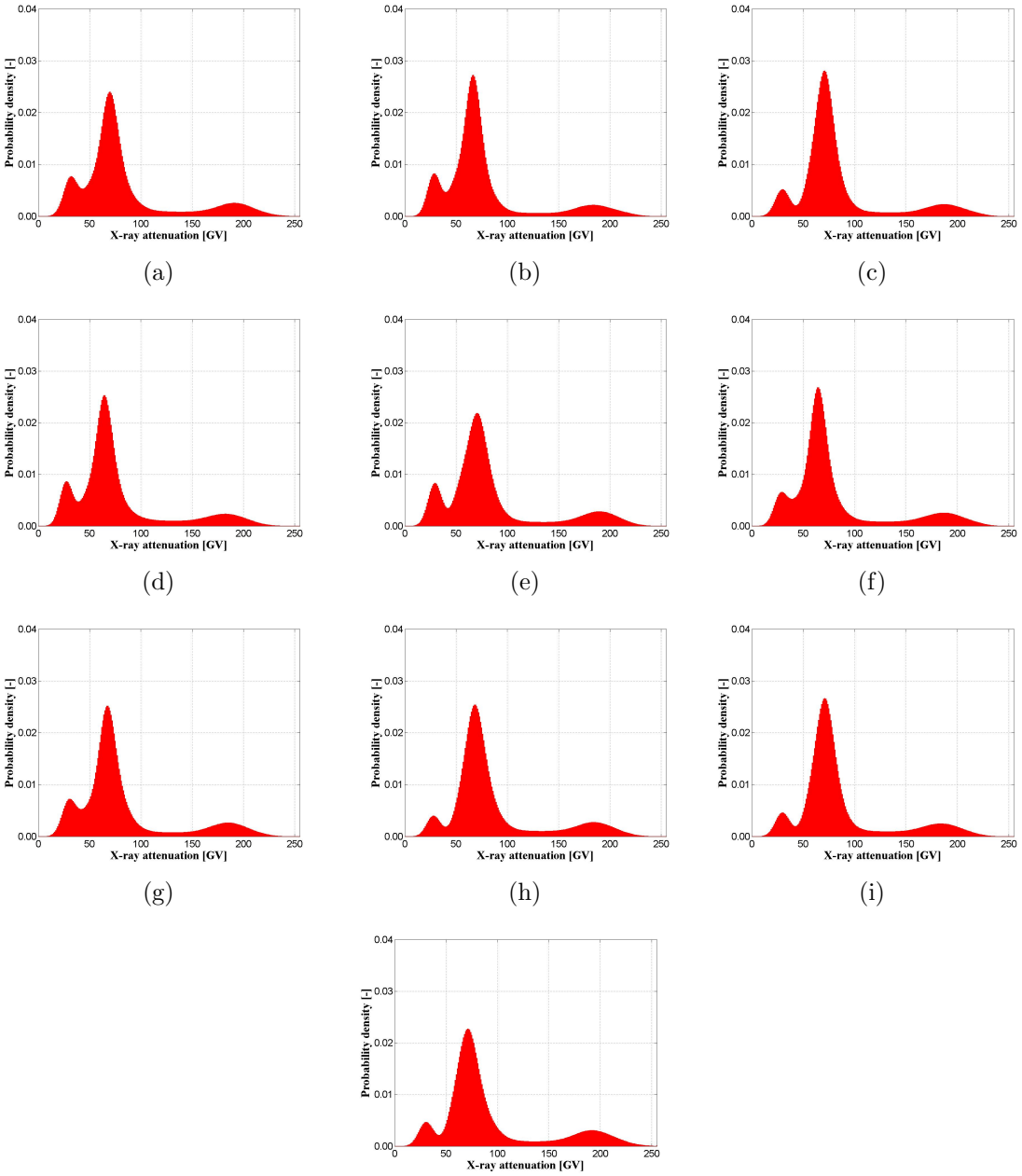

Figure 6: Probability density functions of attenuation-related grey values: (a)-(j) OXV rats 1-10

Table 4: Line constants a and b, as well as attenuation coefficients and densities of the bone tissue at the photon energy of 14 [keV] (OVX)

Samples	**1**	**2**	**3**	**4**	**5**	**6**	**7**	**8**	**9**	**10**	**mean**	**STD**
a	0.049	0.049	0.046	0.052	0.046	0.052	0.052	0.047	0.046	0.047	0.049	0.003
b·(−1)	1.623	1.476	1.413	1.506	1.413	1.558	1.662	1.355	1.413	1.4953	1.492	0.099
μ_{bone}	7.884	7.588	7.124	8.010	7.261	8.217	8.010	7.349	7.033	7.536	7.601	0.412
ρ_{bone}	1.297	1.282	1.259	1.303	1.266	1.313	1.303	1.270	1.255	1.280	1.283	0.020
f_{HA}	0.116	0.111	0.102	0.119	0.104	0.123	0.119	0.160	0.100	0.110	0.111	0.008
f_{org}	0.157	0.149	0.137	0.160	0.141	0.165	0.160	0.143	0.135	0.148	0.149	0.011
f_{H_2O}	0.727	0.741	0.762	0.721	0.755	0.712	0.721	0.751	0.766	0.743	0.740	0.019

Obviously, there are some variations from one image stack to another, but those are relatively small - and even smaller is the difference between OVX- and sham rat-related images. Corresponding reconstructions of X-ray energy-dependent slope and intersect parameter functions $a(\varepsilon)$ and $b(\varepsilon)$ according to Eq. (3) deliver quite similar, yet not identical functions, see Figures 9(a) and (b). Similarly small changes are seen in the image-specific functions (11), based on (10), (9), and (8), see Figure 9(c).

The maxima of these functions, identifying the used X-ray energy, however, are even identical: $\overline{\varepsilon} = 14$ keV. Hence, virtually no variations in the photon spectrum emitted in the scanner are detectable. This energy value, when used in the functions depicted in Figure 9(a,b), allows for identification of image-specific slope and intersect parameters $a(\overline{\varepsilon})$ and $b(\overline{\varepsilon}$, see Table 3 for sham rats, and Table 4 for OVX rats.

Use of these parameters in Eq. (1) allows for determination of voxel-specific attenuation coefficients, as depicted in the form of histograms in Figure 7 for sham rats and in Figure 8 for OVX rats.

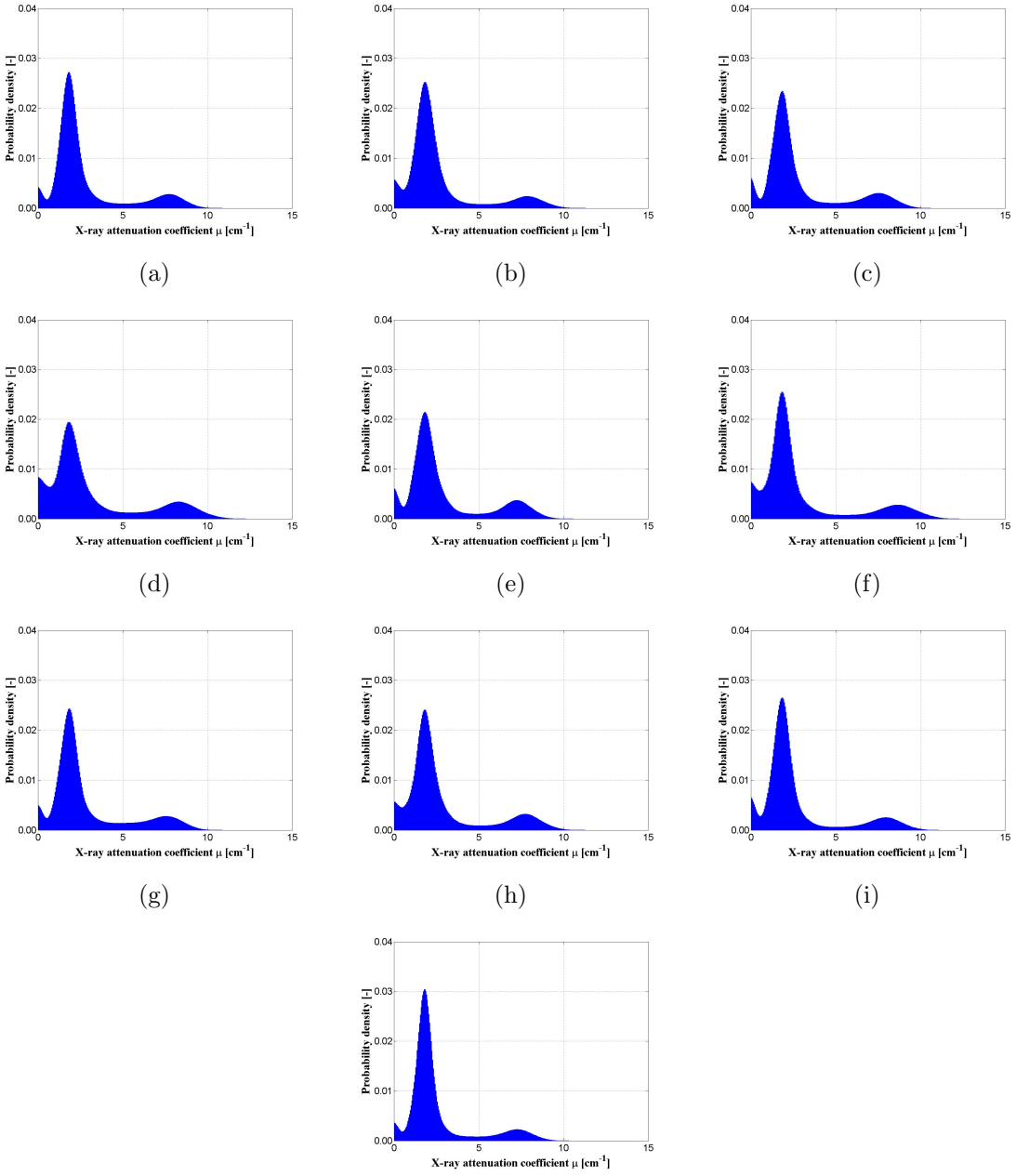

Figure 7: Probability density functions of attenuation coefficients: (a)-(j) sham rats 1-10

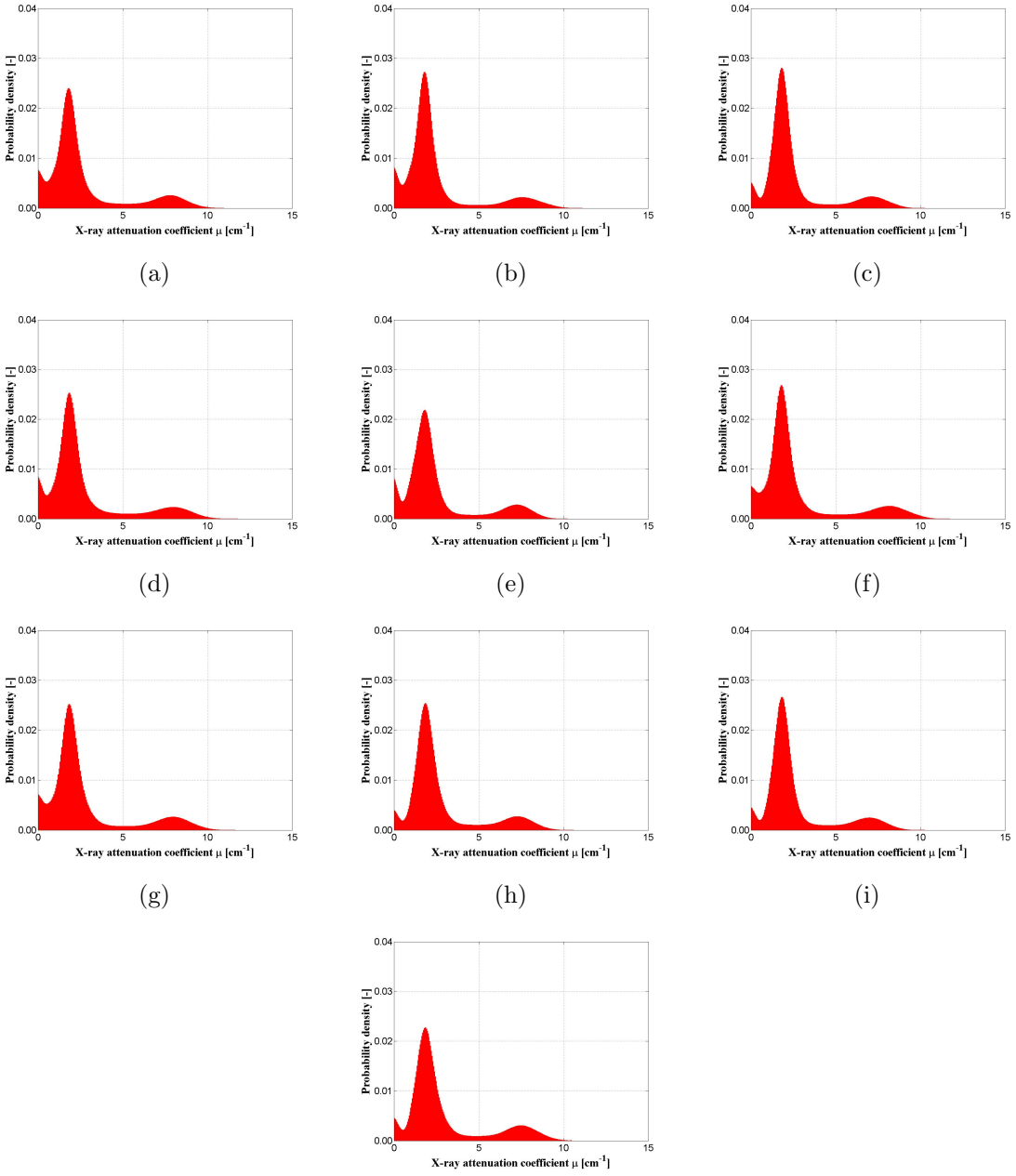

Figure 8: Probability density functions of attenuation coefficients: (a)-(j) OVX rats 1-10

The corresponding most frequently occurring attenuation coefficients in the bony compartments of each of the 20 investigated image stacks vary between 7.3 cm^{-1} and 8.7 cm^{-1} in sham rats (see Table 3) and between 7.0 cm^{-1} and 8.2 cm^{-1} in OVX rats (see Table 4).

Hence, there are not only image stack-related variations in user-specific parameters a and b, but also in the actual, user-independent attenuation behavior of the "average" voxels representing different rats, be they within one of the groups (OVX or sham), or across these groups. The same holds true for the "average" volume fractions of mineral, organics, and water, as well as for "average" mass densities found in the bony voxels, as is evident from Tables 3 and 4 as well.

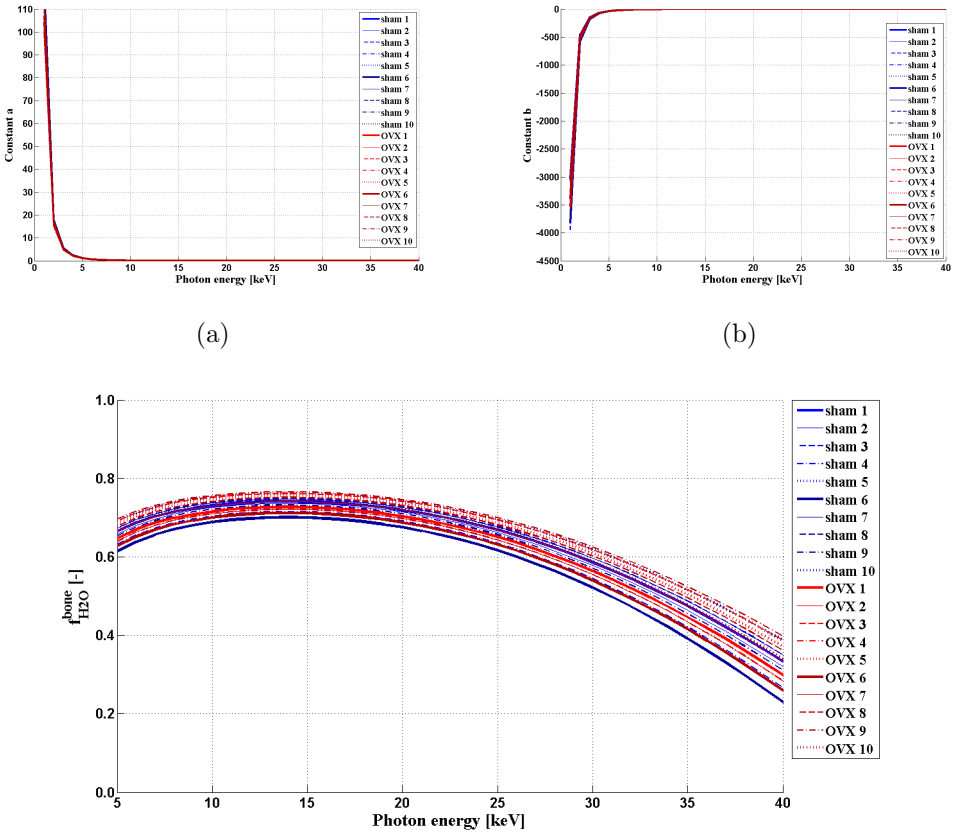

(a) (b)

(c)

Figure 9: (a), (b) Line constants a and b relating grey values to attenuation coefficients, as functions of the photon energy (c) Water volume fractions in the "average" bone voxel, as functions of the photon energy

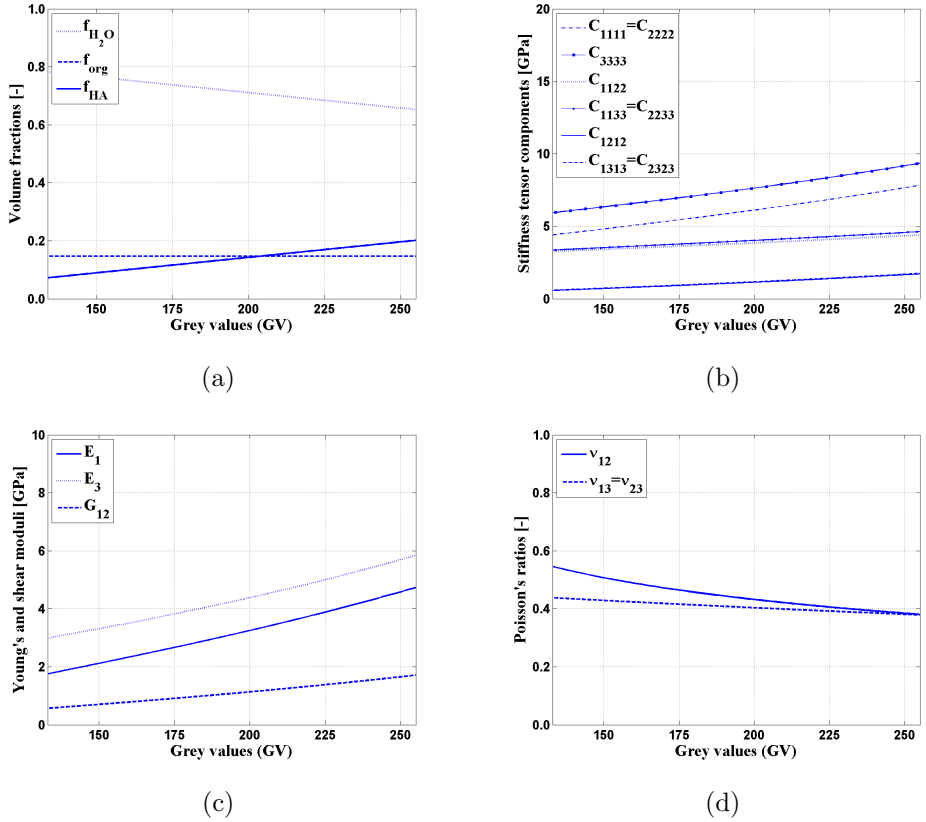

Figure 10: Voxel-specific material parameters of sham rat 6: (a) Volume fractions, (b) Stiffness tensor components, (c) Young's and shear moduli, (d) Poisson's ratios

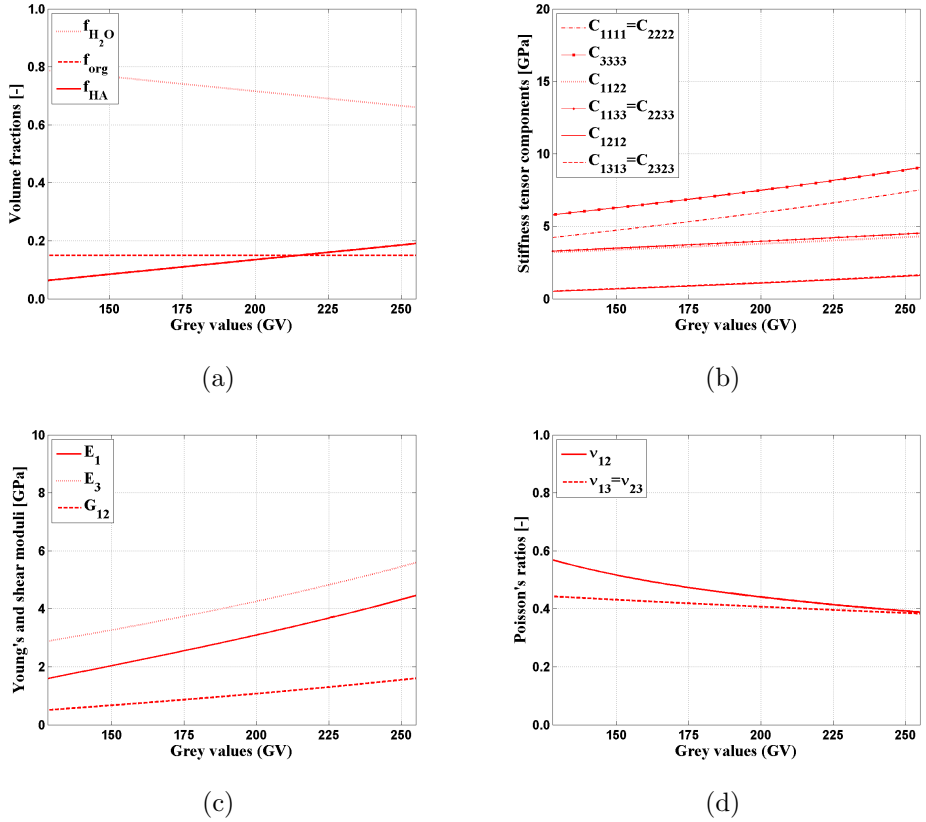

Figure 11: Voxel-specific material parameters of OVX rat 6: (a) Volume fractions, (b) Stiffness tensor components, (c) Young's and shear moduli, (d) Poisson's ratios

The corresponding elastic properties according to Eqs. (17), (18) and (19), as well as the volume fractions of the mineral are illustrated as maps in Figures 12 and 13, while respective average values are given in Tables 5 and 6.

Table 5: Material parameters $E_{excel,1}$, $E_{excel,3}$ and $G_{excel,12}$ in [GPa], and $\nu_{excel,12}$ and $\nu_{excel,13}$ in [-] of the bone threshold, landmark and maxium values for the sham rats

Samples	**1**	**2**	**3**	**4**	**5**	**6**	**7**	**8**	**9**	**10**	**mean**	**STD**
$E^{range}_{excel,1}$	1.555	1.699	1.542	1.756	1.506	1.756	1.443	1.582	1.587	1.513	1.594	0.108
	2.627	2.675	2.567	2.872	2.436	3.012	2.569	2.634	2.711	2.437	2.654	0.180
	3.992	4.209	3.861	4.700	3.839	4.730	3.993	4.183	4.085	3.717	4.131	0.344
$E^{range}_{excel,3}$	2.821	2.943	2.811	2.992	2.780	2.992	2.729	2.844	2.848	2.786	2.855	0.091
	3.785	3.830	3.729	4.018	3.605	4.152	3.730	3.791	3.865	3.607	3.811	0.170
	5.108	5.321	4.978	5.810	4.956	5.840	5.108	5.296	5.199	4.837	5.245	0.340
$G^{range}_{excel,12}$	0.495	0.547	0.490	0.568	0.477	0.568	0.454	0.504	0.506	0.479	0.509	0.039
	0.895	0.914	0.872	0.989	0.822	1.043	0.873	0.898	0.927	0.823	0.906	0.069
	1.424	1.508	1.372	1.701	1.363	1.713	1.424	1.498	1.460	1.316	1.478	0.135
$\nu^{range}_{excel,12}$	0.572	0.553	0.574	0.546	0.579	0.546	0.588	0.568	0.567	0.578	0.567	0.015
	0.467	0.464	0.471	0.452	0.481	0.444	0.471	0.467	0.462	0.481	0.466	0.012
	0.402	0.395	0.407	0.381	0.408	0.381	0.402	0.396	0.399	0.412	0.399	0.011
$\nu^{range}_{excel,13}$	0.444	0.440	0.444	0.438	0.445	0.438	0.447	0.443	0.443	0.445	0.443	0.003
	0.417	0.416	0.418	0.411	0.421	0.409	0.418	0.417	0.415	0.421	0.416	0.004
	0.390	0.387	0.393	0.379	0.393	0.379	0.390	0.387	0.389	0.395	0.388	0.005

Table 6: Material parameters $E_{excel,1}$, $E_{excel,3}$ and $G_{excel,12}$ in [GPa], and $\nu_{excel,12}$ and $\nu_{excel,13}$ in [-] of the bone threshold, landmark and maxium values for the OVX rats

Samples	**1**	**2**	**3**	**4**	**5**	**6**	**7**	**8**	**9**	**10**	**mean**	**STD**
$E^{range}_{excel,1}$	1.661	1.566	1.476	1.735	1.493	1.593	1.634	1.504	1.440	1.559	1.566	0.092
	2.692	2.571	2.384	2.744	2.439	2.830	2.744	2.474	2.348	2.550	2.578	0.168
	4.062	4.135	3.720	4.477	3.720	4.449	4.395	3.886	3.720	3.819	4.038	0.312
$E^{range}_{excel,3}$	2.939	2.859	2.785	3.002	2.799	2.882	2.916	2.808	2.755	2.853	2.860	0.077
	3.872	3.758	3.584	3.921	3.635	4.003	3.921	3.668	3.550	3.738	3.765	0.157
	5.201	5.273	4.864	5.612	4.864	5.585	5.531	5.028	4.864	4.961	5.178	0.308
$G^{range}_{excel,12}$	0.533	0.498	0.465	0.560	0.472	0.508	0.523	0.476	0.453	0.496	0.498	0.033
	0.919	0.873	0.802	0.939	0.823	0.972	0.939	0.836	0.788	0.865	0.876	0.064
	1.450	1.479	1.317	1.613	1.317	1.602	1.581	1.381	1.317	1.355	1.441	0.122
$\nu^{range}_{excel,12}$	0.559	0.572	0.585	0.550	0.583	0.569	0.563	0.581	0.591	0.573	0.573	0.013
	0.464	0.472	0.486	0.461	0.482	0.456	0.460	0.479	0.489	0.474	0.472	0.012
	0.401	0.398	0.413	0.388	0.413	0.389	0.390	0.407	0.413	0.409	0.402	0.010
$\nu^{range}_{excel,13}$	0.441	0.444	0.446	0.439	0.446	0.443	0.442	0.445	0.447	0.444	0.444	0.003
	0.416	0.418	0.423	0.415	0.422	0.413	0.415	0.421	0.424	0.419	0.418	0.004
	0.390	0.388	0.395	0.383	0.395	0.384	0.384	0.393	0.395	0.394	0.390	0.005

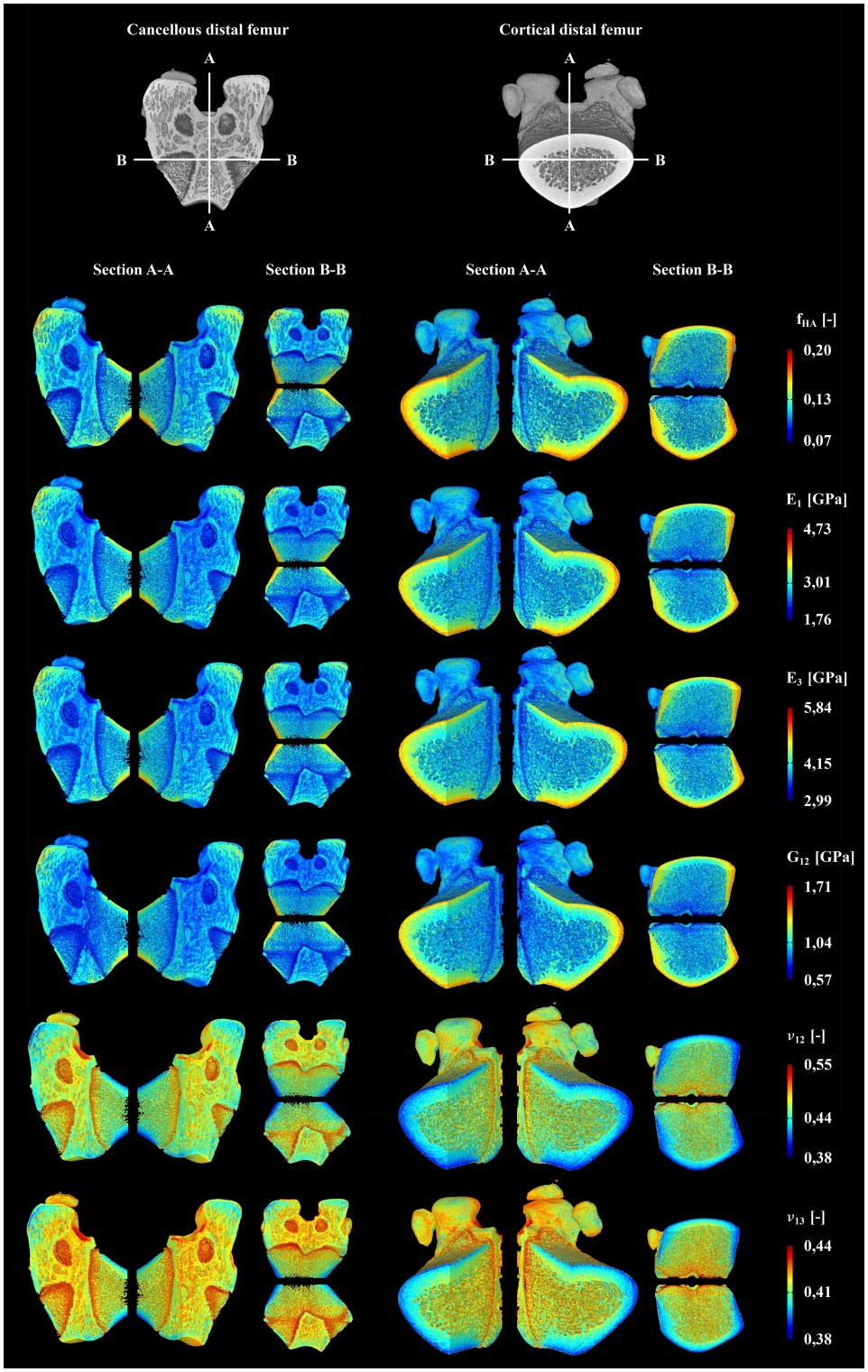

Figure 12: Distribution of the mineral volume fraction and of the material parameters within the distal femur of sham rat 6 under specification of the bone threshold, landmark and maximum values

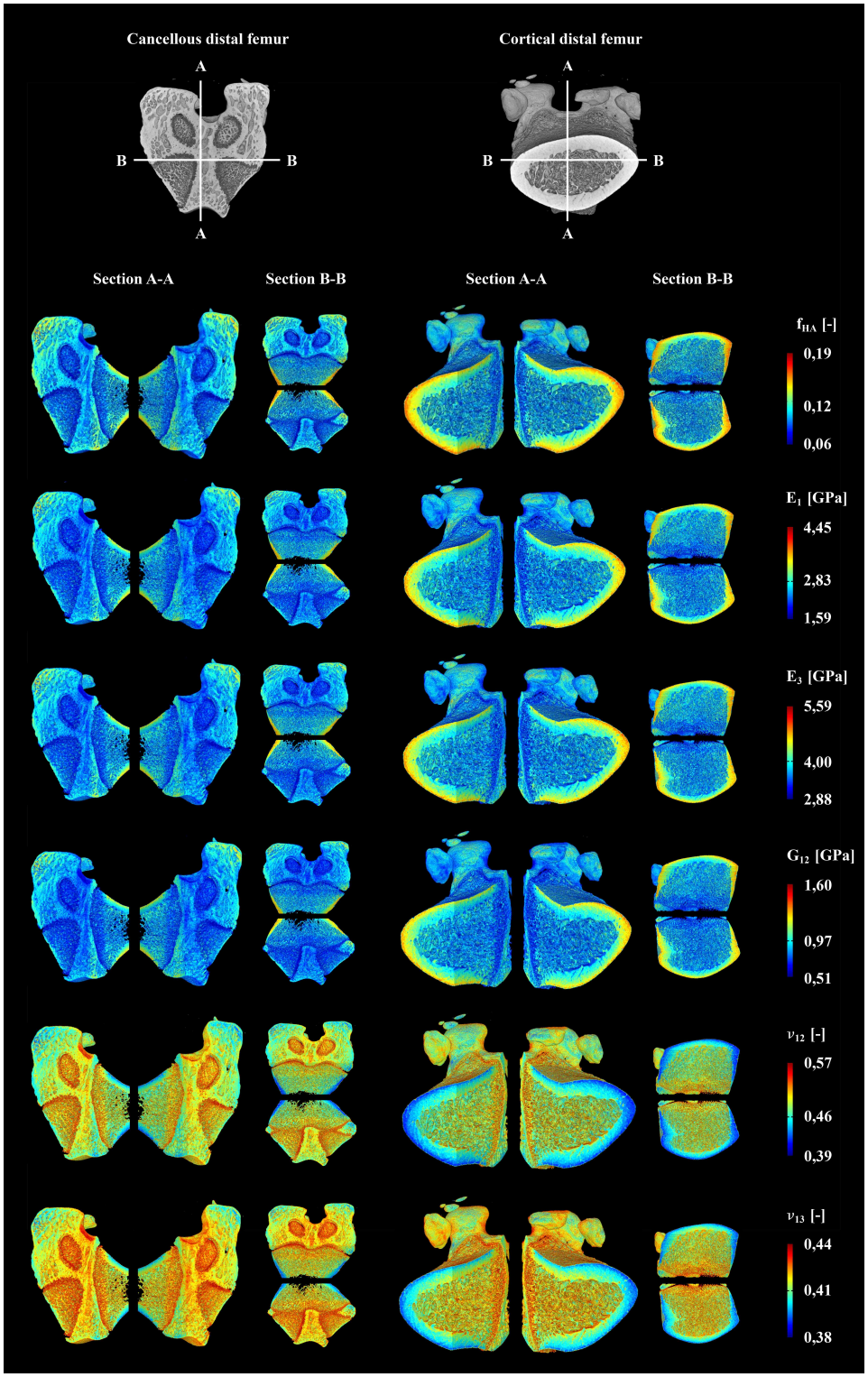

Figure 13: Distribution of the mineral volume fraction and of the material parameters within the distal femur of OVX rat 6 under specification of the bone threshold, landmark and maximum values

2.5 Discussion

While traditional approaches of micro-CT evaluation target at morphometric analysis of the entire image stacks based on a variety of different quantities such as bone mineral density (BMD), bone mineral content (BMC), bone/tissue volume (BV/TV), trabecular separation (Tb.Sp), trabecular number (Tb.N), trabecular thickness (Tb.Th), structure model index (SMI) and connectivity density (ConnD) (Fanti et al., 1998; Laib et al., 2000; Borah et al., 2001; Wang et al., 2001; Lesclous et al., 2004; Campbell et al., 2008; Saito et al., 2009; Donnelly, 2011; Francisco et al., 2011; Böcker et al., 2014; Govindarajan et al., 2014; Yang et al., 2014), the present contribution focussed on the information contained in each and every voxel, beyond a producer- and user-dependent grey value representing a mixture of physical properties and tunable regression parameters. Therefore, the linear relation between grey values and attenuation coefficients, the energy-dependence of the latter, and the average rule they obey to, were appropriately combined with drying and ashing tests on bones similar to those scanned - namely femurs from sham and OVX rats. As results, the average photon energy of the light source was quantified, as were the voxel-dependent mineral, organic, water volume fractions, i.e. the composition of each and every voxel. Feeding the latter information into a validated micro elastic model yielded maps of elastic properties across the organ, as valuable source for potential structural analyses. The compositional data, in combination with the mass densities of mineral, organics, and water, give access to the voxel-specific mass density of bony voxels, and the average value of the latter, amounting to about 1.3 g/cm^3 according to our analysis based on CT images and ashing/drying tests, agrees very well with independent, direct mass density measurements on rat femurs (Hammett, 1925; Anamula et al., 2010), delivering an average value of 1.3 g/cm^3. This good agreement gives additional confidence in our new method.

Secondly, it becomes evident that the inter-group variations (within the OVX and sham rat groups), of all studied variables, such as grey values, attenuation coefficients, volume fractions, and elastic properties, are much larger than the differences between the OVX and the sham group. To underline this effect, we performed an ANOVA testing the null hypothesis that the OVX data and the sham rat data belong to the same statistical population. This null hypothesis can be actually retained at high probability values, amounting to p=29.29 % for the grey values, p=22.59 % for

the attenuation coefficients, p=22.41 % for the mineral volume fraction and p=53.40 % for the axial Young's modulus. Hence, OVX animals are not always successful in mimicking osteoporosis, as is also reported in the open literature: Looking into the details, the null hypothesis is particularly valid for the axial Young's modulus of the bone tissue, $E_{excel,3}$, indicating that the used OVX model behaves least effectively when induction of changes in mechanical properties at the bone tissue level are concerned.

In this sense, our results somehow support those who warn that OVX animal models may not always be successful in mimicking human osteoporosis. Reasons for that the lost function of the ovaries in rats does not always provoke similar effects as in humans were reviewed by Kalu (1991): (i) rats exhibit a stable bone mass, or even gain bone, throughout most of their lifetime (in contrast to humans), and (ii) bone remodeling patterns in rats differ from those in humans, e.g. the former do not exhibit Haversian cortical bone.

The remodeling activities can also be traced in terms of mineralization states at the bone tissue scale (Roschger et al., 2008), where higher attenuation would be related to lower remodeling activities (indicating osteoporosis). However, the OVX rats exhibit lower bone attenuation properties (and smaller mineral volume fractions) when compared to the sham rats - and the latter properties can even be more easily distinguished between the OVX and the sham rat groups, relative to Young's modulus and grey values. As a further measure for "OVX-induced osteoporosis", the overall bone (tissue) mass in the investigated rats can be estimated by counting the voxels with $GV > GV_{thr}$. We observed that the rat femurs do not show any statistically significant difference (p=99.95 %) between OVX and sham rats. This result is in line with the findings of (Francisco et al., 2011), showing that the femur is the least OVX-effected bone, when compared to tibia and spine. We summarize that our new method, beyond giving access to X-ray energy, and voxel-specific bone compositional and elastic informations, also allows for deeper scrutiny into the functioning of any bony construct having been micro-CT-scanned, including widely studied, FDA-approved animal models such as the OVX rat (Thompson et al., 1995).

3 Summary and future outlook

Due to its high temporal and spacial resolution, micro-CT has become a major tool in preclinical investigations of osteoporosis in small animals (Kapadia et al., 1998; Holdsworth and Thornton, 2002; Schambach et al., 2010). The non-destructive and by now rapid technique enables to monitor and precisely measure the pathophysiological alterations within the bone tissue of in vivo and in vitro specimens at any given moment (Holdsworth and Thornton, 2002; Genant et al., 2008). Among these bone quality characterising parameters obtained by a histomorphometric analysis are the bone mineral density (BMD), the bone mineral content (BMC), the bone/tissue volume (BV/TV), the trabecular separation (Tb.Sp), the trabecular number (Tb.N), the trabecular thickness (Tb.Th), the structure model index (SMI) and the connectivity density (ConnD) (Fanti et al., 1998; Laib et al., 2000; Borah et al., 2001; Wang et al., 2001; Lesclous et al., 2004; Campbell et al., 2008; Saito et al., 2009; Donnelly, 2011; Francisco et al., 2011; Böcker et al., 2014; Govindarajan et al., 2014; Yang et al., 2014).

The histomorphometric analysis itself is usually based on the statistical evaluation of the three-dimensional CT "image" data with histograms of the bit depth-specific grey values assigned to the voxels, and used to identify material thresholds and landmarks (Taleb-Ahmed et al., 2003; Tabor and Latała, 2014). The grey values are linearly related to the photon energy dependent X-ray attenuation coefficients of the scanned materials (Skyscan, 2010; Fritsch et al., 2011; Blanchard et al., 2013; Czenek et al., 2014) which describe the decrease of X-ray beam intensity per length of pervaded matter and are published by NIST (Hubbell and Seltzer, 1996). For a composite material, this physical quantity can be expressed by the sum of the respective attenuation coefficients of the single constituents - in case of bone tissue: water, organic matter and mineral (Blanchard et al., 2013) - weighted over their spatial distribution within the voxel (Jackson and Hawkes, 1981,Crawley et al., 1988; Hellmich et al., 2008). Therefore, the novel method to gain the applied X-ray energy introduced by Czenek et al. (2014) and adapted to the extracellular bone tissue (Blanchard et al., 2013), not only directly connects the scientifically established X-ray attenuation coefficients with the grey values obtained from CT images, but additionally considers the heterogeneous conditions within the voxels.

Utilization of predetermined mean mineral-to-organic ratios for the sham and OVX

rats gained from ashing experiments (Kim et al., 2009) results in mean organic volume fractions providing the initial position for the investigation of the demineralization within the bone ultrastructure due to osteoporosis, and a solid foundation for a precise determination of the voxel-specific bone mass densities based on the identified X-ray energy. Applied from the nanostructure up to the ultrastructure, the Mori-Tanaka homogenization scheme (Mori and Tanaka, 1973; Benveniste, 1987) delivers the estimated voxel-specific mechanical behaviour mathematically derived from known estimated elastic properties and morphologies of the elementary components (Hellmich et al., 2004a; Fritsch and Hellmich, 2007; Fritsch et al., 2009a; Morin and Hellmich, 2014).

Although the used method is predicated on profound scientific findings, no pathophysiological alterations could be demonstrated within the bone tissue due to oestrogen-deficiency induced osteoporosis. The occurring similarity between OVX and sham rats in respect to bone density and material properties primarily relies on the grey values and attenuation coefficients of bone (see 2.4) obtained by image processing using a specific bit depth, whose increase might enhance the technique's sensitivity to bone loss.

Besides, the applied OVX rat model in principle has to be questioned, as the literature provides no standardised procedure dictating the age of rats at ovariectomy, the length of time post-OVX until sacrifice and the considered skeletal site all contributing to the bone's deterioration (Thompson et al., 1995; Francisco et al., 2011; Liu et al., 2014).

In studies quantifying bone loss, the OVX rat usually exhibits a decrease in BMD, BV/TV, Tb.N, Conn.D and an increase in Tb.Sp , Tb.Pf and SMI, indicating a reduced trabecular connectivity and a trabecular shape-shifting from plate-like to more vulnerable rod-like compared to their sham-operated counterparts (Francisco et al., 2011; Govindarajan et al., 2014; Liu et al., 2014).

Considering the age of the rats at ovariectomy, Kalu (1991) recommended after extensive research to use rats ovariectomized at the age of approximately 3 months when sexually maturity (mature rat model) is reached, or up from the age of 6 months when a skeletal maturity (aged rat model) is attained expressed by minimal changes in femur density and calcium and in return no ageing effect influences the modification of the bone structure (Francisco et al., 2011).

However, Francisco et al. (2011) discovered that 24 weeks is a promising age to get a stable and clear response to ovarian hormone-deficiency induced osteoporosis

in the tested microarchitectural parameters, whereas 12 weeks aged rats showed a reduced response. The applied findings of Kim et al. (2009) refer to rats aged 10 weeks at their operation which should already make them capable of responding appropriately to sex hormone deficiency (Kalu, 1991) and to an experiment length of 6 weeks.

In respect to the skeletal site, the literature states that the distal femur showed significant differences between OVX and sham in most of the tested microarchitectural parameters, among them BMD, Tb.SP and Tb.N (Francisco et al., 2011; Liu et al., 2014). However, the significance of femurs used from 6 month old rats occurred at different times post-OVX; in Liu et al. (2014) from about week 4-12 going on till week 36 and in Francisco et al. (2011) from about weeks 15-20 until week 30.

In addition, Kalu (1991) postulated that the observation period from operation to sacrifice depends on the age of the animals and the sensitivity of the technique to mineral losses and changes in the microarchitecture. Therefore, according to Kalu (1991), Thompson et al. (1995) and Anamula et al. (2010) bone ash determination is not an appropriate method to quantify bone loss in OVX rats as the ash content remains constant; however, Kim et al. (2009) discovered otherwise.

Despite all these inconsistencies and the therefore missing reliability, the OVX rat model is the most widely used animal model for osteoporosis research - especially to evaluate new, potential agents for osteoporosis prevention and therapy - and recommended by the FDA (Thompson et al., 1995). However, with an ageing population, postmenopausal osteoporosis will become a growing public health issue (Rachner et al., 2011) demanding for a universal procedure in OVX rat models to evaluate the process of deterioration and to deliver comparable results in the future. As the applied method shows realistic densities when compared to the literature (Hammett, 1925; Anamula et al., 2010), it might further enhance a precise and standardised evaluation of the bone structure in respect to post-menopausal osteoporosis research. Future work could include the investigation of the mechanical properties in respect to fracture risk assessment (Blanchard, 2014).

A Figures of all rat stacks

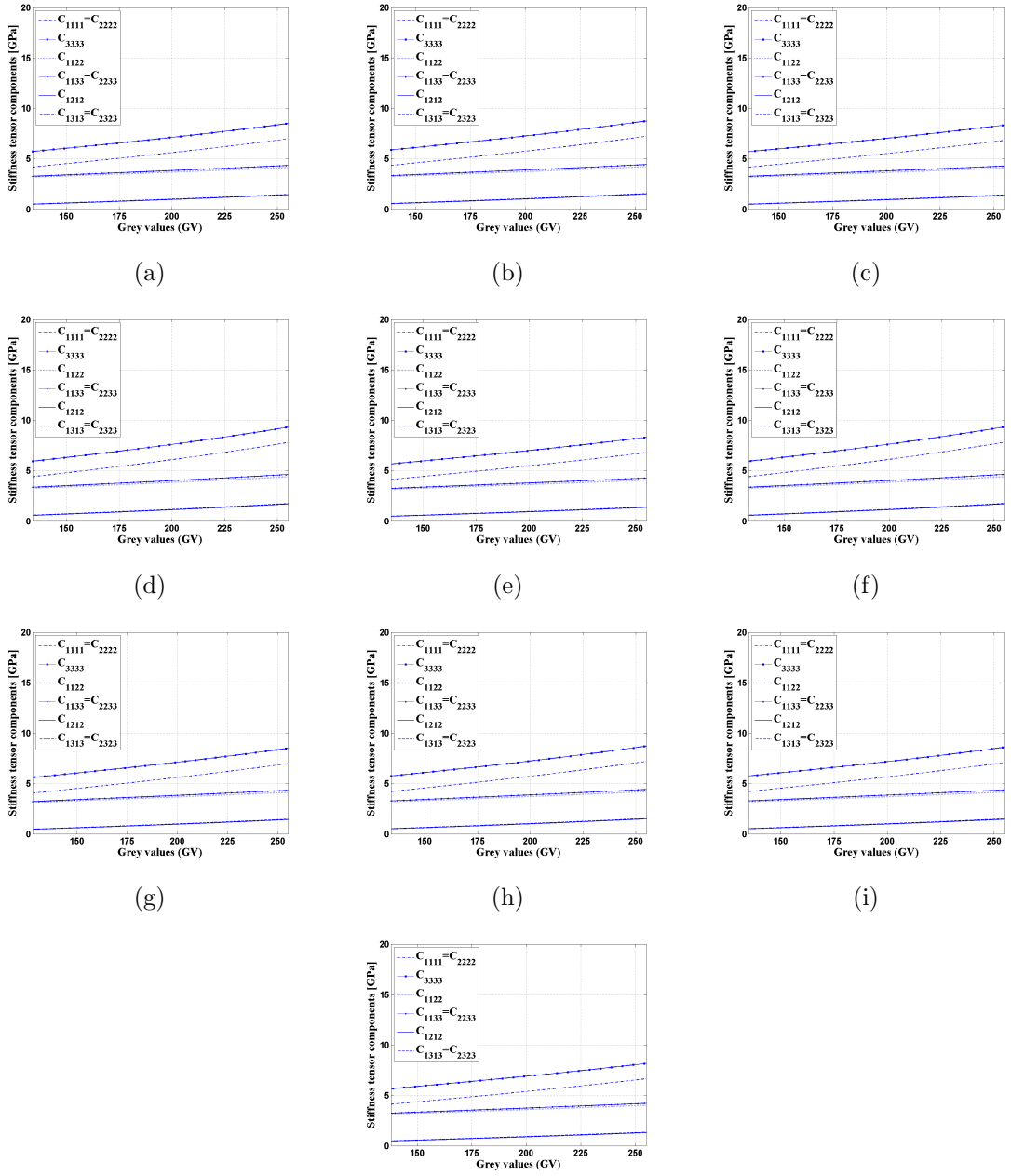

Figure 14: Stiffness tensor at the apparent photon energy against grey values: (a)-(j) sham rats 1-10

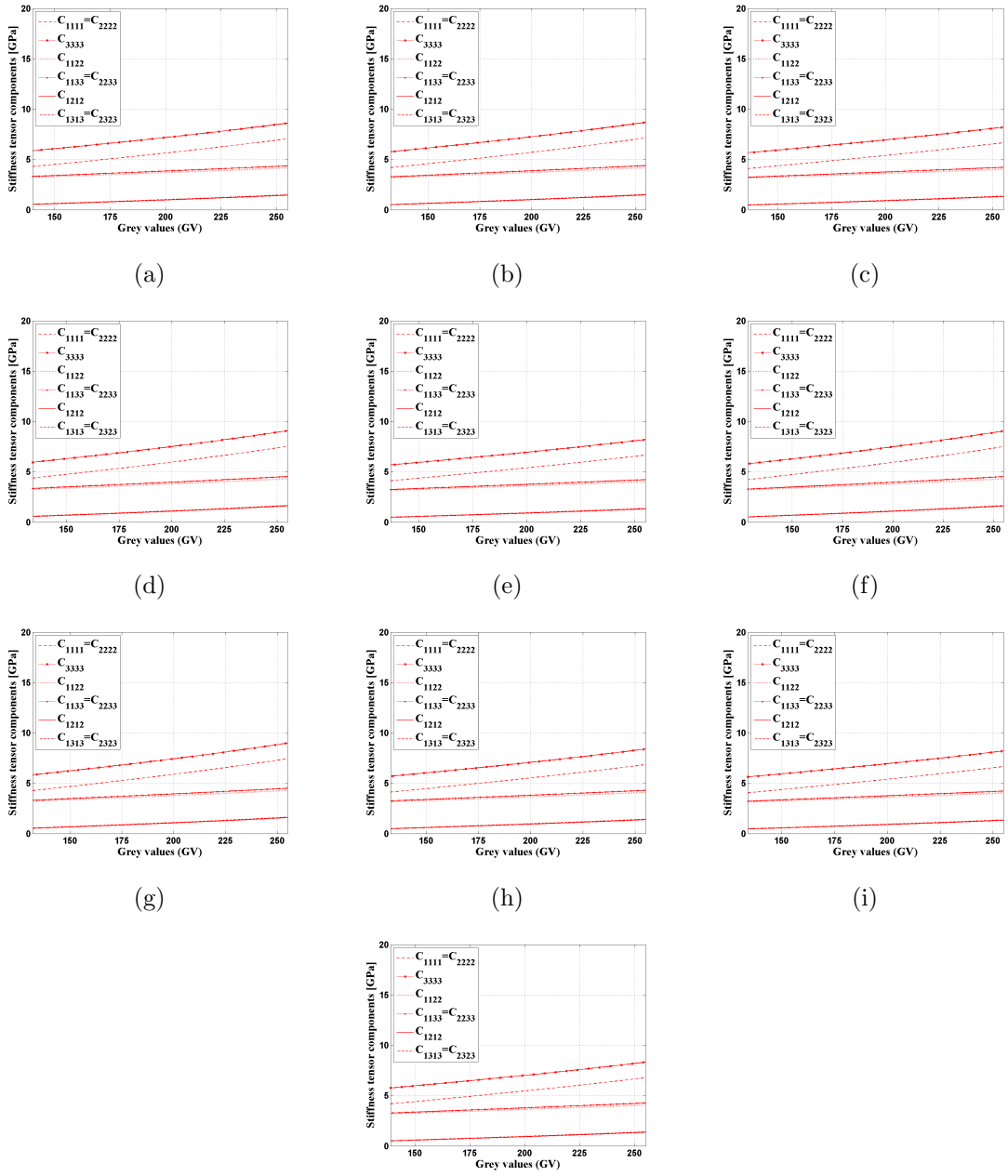

Figure 15: Stiffness tensor at the apparent photon energy against grey values: (a)-(j) OVX rats 1-10

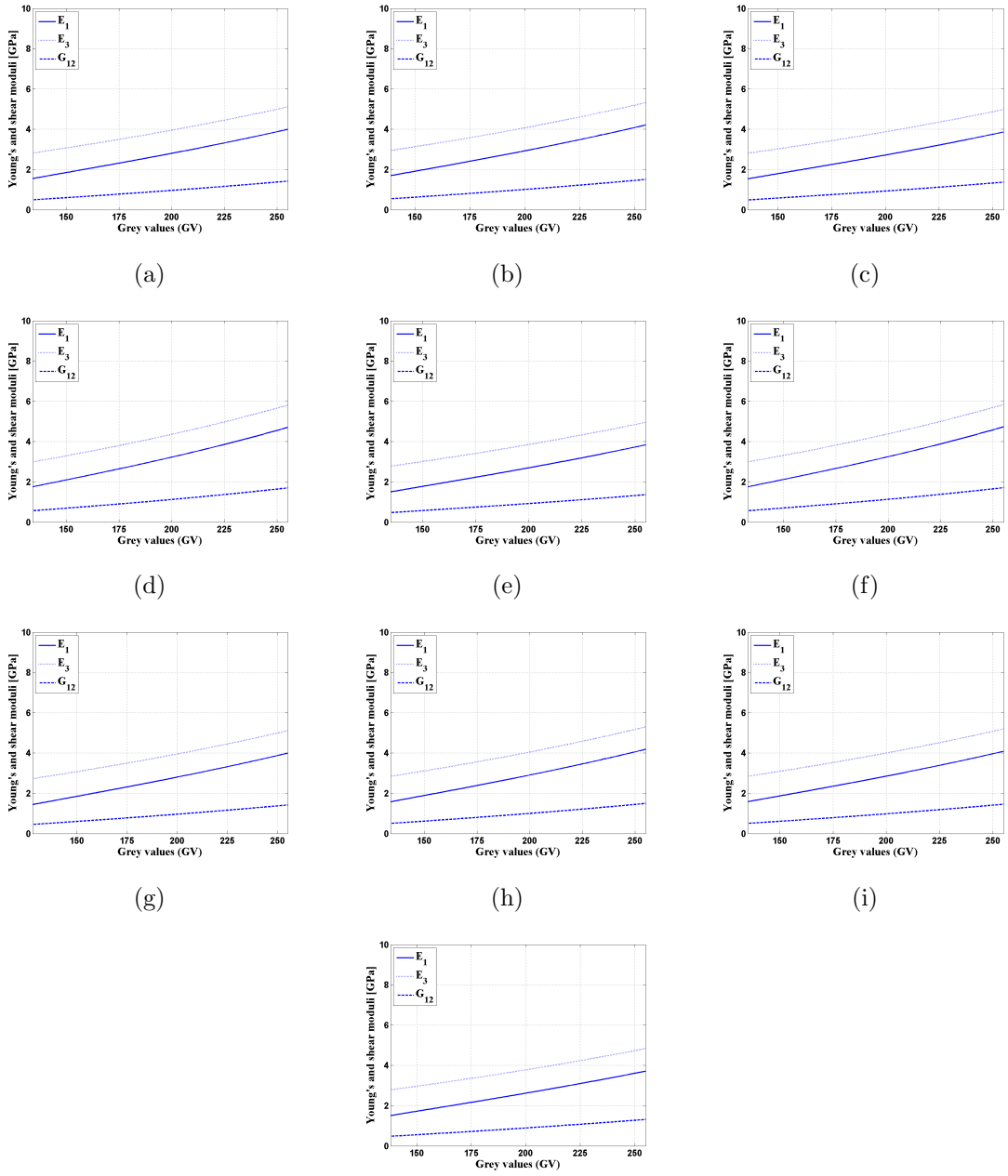

Figure 16: Young's and shear moduli at the apparent photon energy against grey values: (a)-(j) sham rats 1-10

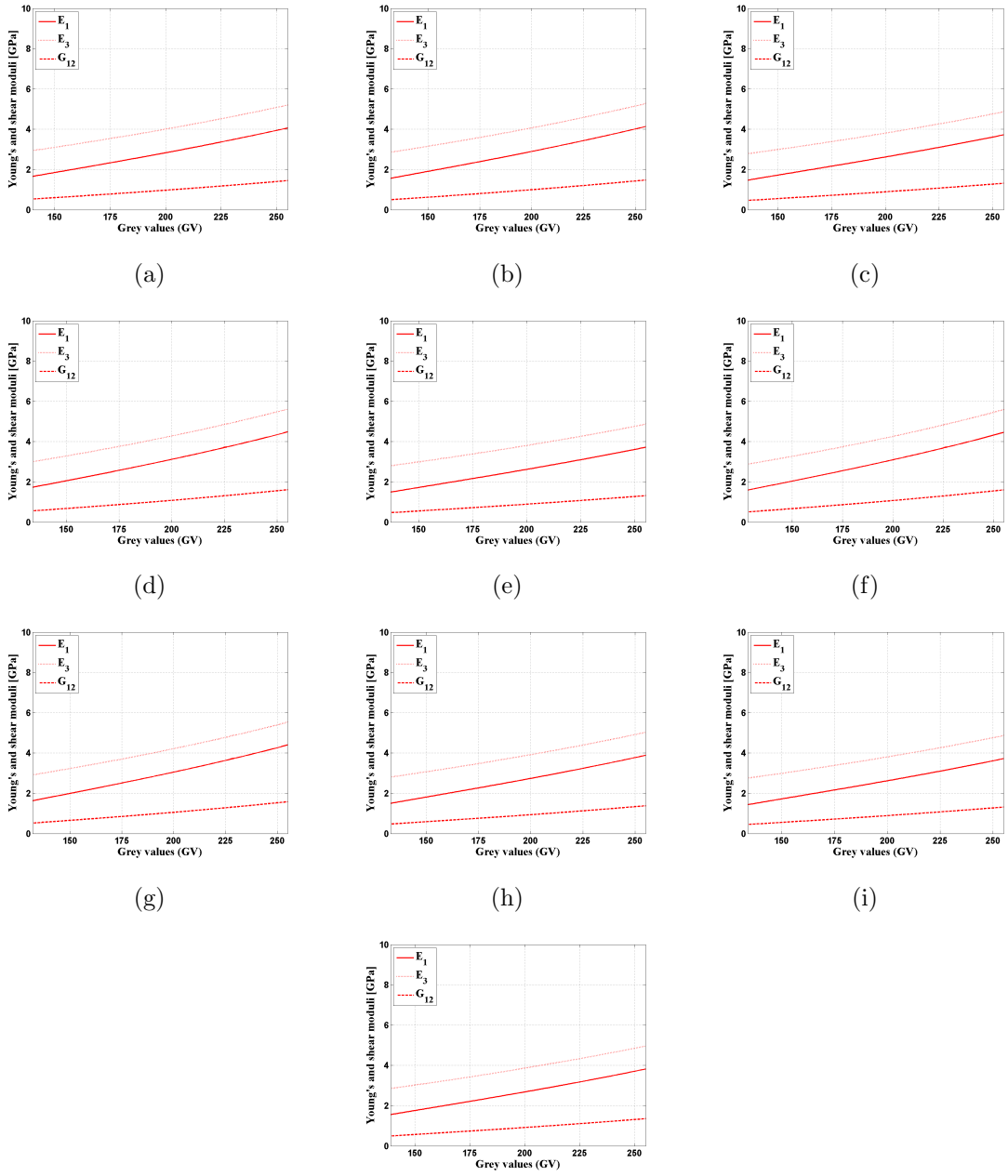

Figure 17: Young's and shear moduli at the apparent photon energy against grey values: (a)-(j) OVX rats 1-10

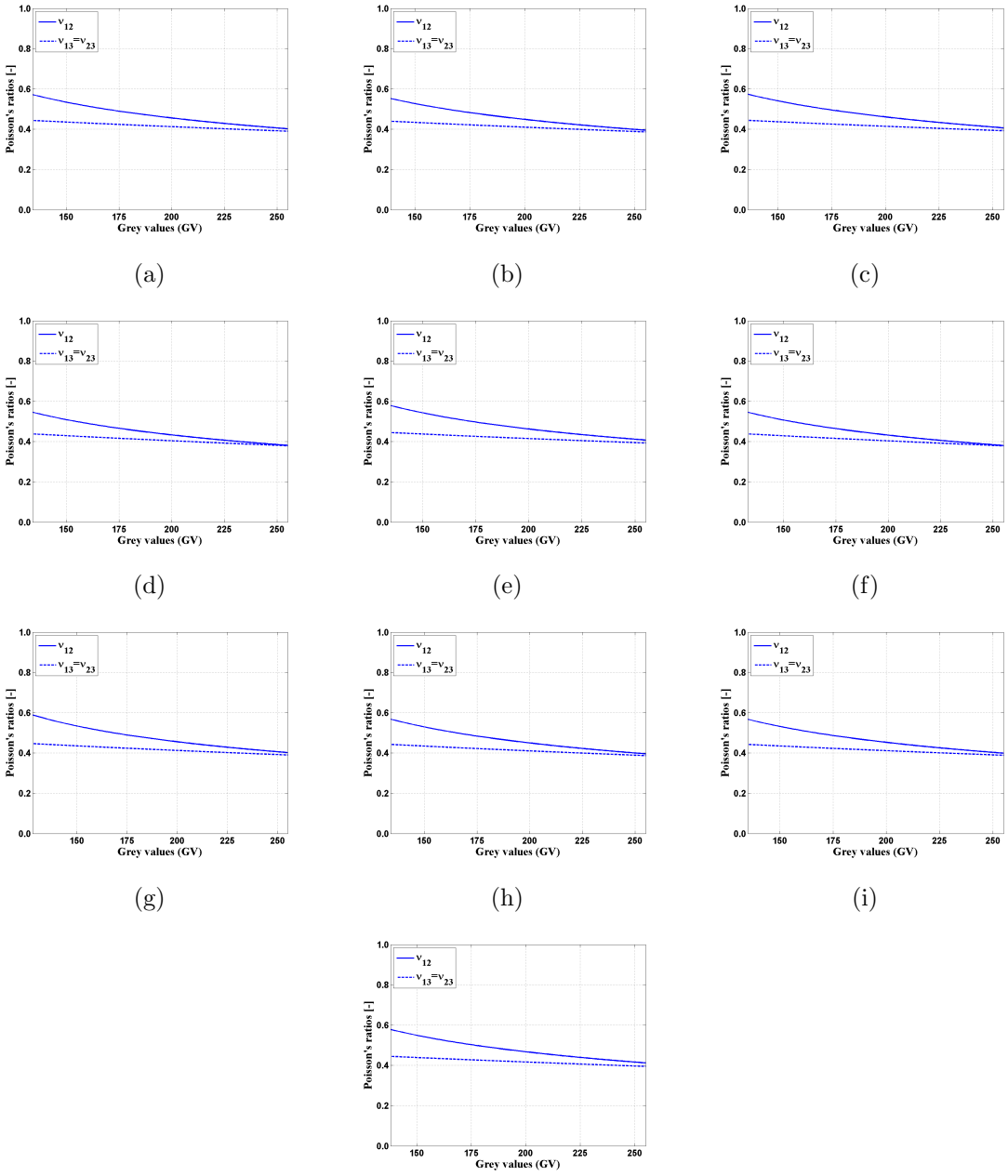

Figure 18: Poisson's ratios at the apparent photon energy against grey values: (a)-(j) sham rats 1-10

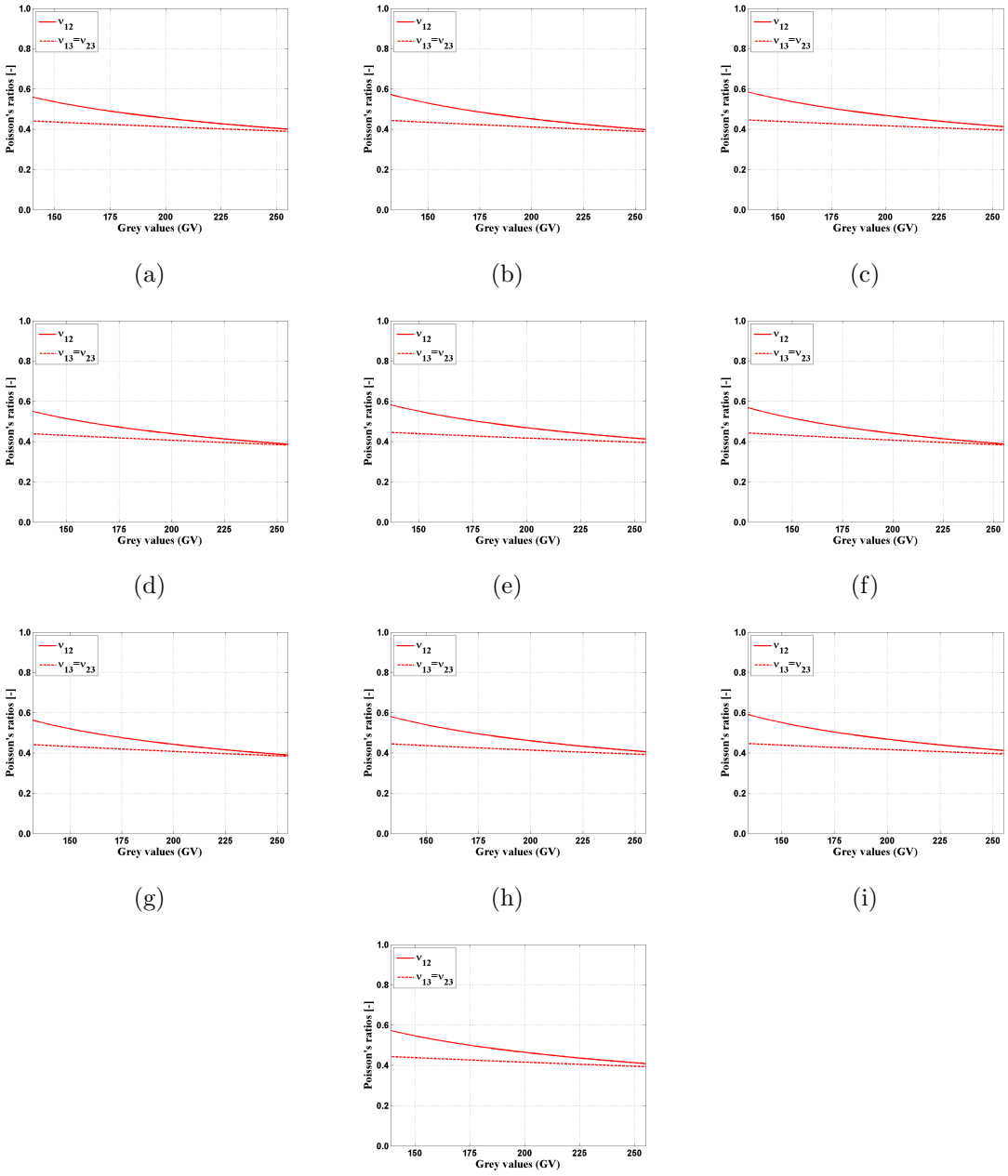

Figure 19: Poisson's ratios at the apparent photon energy against grey values: (a)-(j) OVX rats 1-10

B Analysis of variance (ANOVA)

In the following five tables the headings "Source of Variation", "Dregrees of Freedom" and "Sum of Squares" are abbreviated by "SV", "DF" and "SS".

Table 7: ANOVA for the most frequently occurring mineral volume fraction of sham and OVX rats

f_{HA}	**SV**	**DF**	**SS**	**F**	**P-Value**	$\mathbf{F}_{crit}$
Difference between sham and OVX rats	0.0001	1	0.0001	1.5854	0.2241	4.4139
Difference within sham and OVX rats	0.0012	18	0.0001			
Total	0.0013	19				

Table 8: ANOVA for the bone grey values $GV > GV_{thr}$ of sham and OVX rats

$GV > GV_{thr}$	**SV**	**DF**	**SS**	**F**	**P-Value**	$\mathbf{F}_{crit}$
Difference between sham and OVX rats	6026.7258	19	317.1961	0.2554	0.9995	1.5908
Difference within sham and OVX rats	0.0012	2409	1241.7854			
Total	2997487.7260	2428				

Table 9: ANOVA for the most frequently occurring bone grey values of sham and OVX rats

GV_{bone}	**SV**	**DF**	**SS**	**F**	**P-Value**	$\mathbf{F}_{crit}$
Difference between sham and OVX rats	11.2500	1	11.2500	1.1739	0.2929	4.4139
Difference within sham and OVX rats	172.5000	18	9.5833			
Total	183.7500	19				

Table 10: ANOVA for the most frequently occurring bone attenuation-coefficient of sham and OVX rats

μ_{bone}	**SV**	**DF**	**SS**	**F**	**P-Value**	$\mathbf{F}_{crit}$
Difference between sham and OVX rats	0.2829	1	0.2829	1.5725	0.2259	4.4139
Difference within sham and OVX rats	3.2382	18	0.1799			
Total	3.5211	19				

Table 11: ANOVA for the most frequently occurring axial Young's moduli of sham and OVX rats

$E_{excel,3}$	**SV**	**DF**	**SS**	**F**	**P-Value**	$\mathbf{F}_{crit}$
Difference between sham and OVX rats	0.0108	1	0.0108	0.4021	0.5340	4.4139
Difference within sham and OVX rats	0.4831	18	0.0268			
Total	0.4939	19				

C Matlab Codes

C.1 Attenuation coefficients of air, water, collagen and hydroxyapatite as functions of the X-ray energy

```
% Table mu_NIST:
% Extracted from the database of the
% National Institute of Standards and Technology (NIST)
% (Hubbell and Seltzer, 1996)
% column 1   = photon energy [MeV]
% columns 2-5= mass attenuation coefficients [cm^2/g]
%              of air (chem. composition acc. to Bolz and Tuve, 1973),
%              water, collagen (C2H5NO2) and hydroxyapatite (Ca5(PO4)3(OH))
%              (without coherent scattering)

mu_NIST=...
       [1.000E-03   3.605E+03   4.076E+03   3.281E+03   4.193E+03
        2.000E-03   5.270E+02   6.162E+02   4.811E+02   6.606E+02
        3.000E-03   1.617E+02   1.919E+02   1.479E+02   4.017E+02
        4.000E-03   7.721E+01   8.207E+01   6.273E+01   1.827E+02
        5.000E-03   3.975E+01   4.203E+01   3.196E+01   3.120E+02
        6.000E-03   2.298E+01   2.419E+01   1.833E+01   1.913E+02
        7.000E-03   1.443E+01   1.513E+01   1.143E+01   1.258E+02
        8.000E-03   9.624E+00   1.006E+01   7.592E+00   8.712E+01
        9.000E-03   6.735E+00   7.025E+00   5.297E+00   6.273E+01
        1.000E-02   4.897E+00   5.099E+00   3.846E+00   4.661E+01
        1.100E-02   3.677E+00   3.823E+00   2.887E+00   3.556E+01
        1.200E-02   2.836E+00   2.946E+00   2.229E+00   2.773E+01
        1.300E-02   2.239E+00   2.325E+00   1.765E+00   2.204E+01
        1.400E-02   1.805E+00   1.874E+00   1.428E+00   1.780E+01
        1.500E-02   1.483E+00   1.539E+00   1.179E+00   1.458E+01
        1.600E-02   1.238E+00   1.286E+00   9.905E-01   1.209E+01
        1.700E-02   1.049E+00   1.091E+00   8.457E-01   1.014E+01
        1.800E-02   9.014E-01   9.385E-01   7.328E-01   8.587E+00
        1.900E-02   7.844E-01   8.179E-01   6.435E-01   7.337E+00
        2.000E-02   6.905E-01   7.213E-01   5.720E-01   6.320E+00
        2.100E-02   6.144E-01   6.430E-01   5.143E-01   5.484E+00
        2.200E-02   5.521E-01   5.789E-01   4.670E-01   4.791E+00
        2.300E-02   5.006E-01   5.261E-01   4.281E-01   4.212E+00
        2.400E-02   4.577E-01   4.821E-01   3.958E-01   3.724E+00
        2.500E-02   4.217E-01   4.452E-01   3.686E-01   3.310E+00
        2.600E-02   3.912E-01   4.141E-01   3.458E-01   2.958E+00
        2.700E-02   3.654E-01   3.876E-01   3.263E-01   2.655E+00
        2.800E-02   3.432E-01   3.650E-01   3.097E-01   2.394E+00
        2.900E-02   3.241E-01   3.455E-01   2.954E-01   2.168E+00
        3.000E-02   3.076E-01   3.286E-01   2.830E-01   1.970E+00
        3.100E-02   2.933E-01   3.140E-01   2.723E-01   1.798E+00
```

3.200E-02	2.807E-01	3.012E-01	2.628E-01	1.646E+00
3.300E-02	2.697E-01	2.899E-01	2.546E-01	1.512E+00
3.400E-02	2.600E-01	2.800E-01	2.473E-01	1.394E+00
3.500E-02	2.514E-01	2.713E-01	2.408E-01	1.289E+00
3.600E-02	2.437E-01	2.635E-01	2.351E-01	1.195E+00
3.700E-02	2.368E-01	2.565E-01	2.299E-01	1.111E+00
3.800E-02	2.307E-01	2.502E-01	2.253E-01	1.036E+00
3.900E-02	2.252E-01	2.446E-01	2.211E-01	9.679E-01
4.000E-02	2.202E-01	2.395E-01	2.174E-01	9.068E-01
4.100E-02	2.157E-01	2.349E-01	2.139E-01	8.516E-01
4.200E-02	2.116E-01	2.308E-01	2.108E-01	8.016E-01
4.300E-02	2.079E-01	2.269E-01	2.080E-01	7.562E-01
4.400E-02	2.044E-01	2.235E-01	2.053E-01	7.148E-01
4.500E-02	2.013E-01	2.203E-01	2.029E-01	6.771E-01
4.600E-02	1.984E-01	2.173E-01	2.007E-01	6.426E-01
4.700E-02	1.958E-01	2.146E-01	1.987E-01	6.110E-01
4.800E-02	1.933E-01	2.121E-01	1.967E-01	5.821E-01
4.900E-02	1.910E-01	2.097E-01	1.950E-01	5.554E-01
5.000E-02	1.889E-01	2.076E-01	1.933E-01	5.309E-01
5.100E-02	1.869E-01	2.055E-01	1.917E-01	5.083E-01
5.200E-02	1.851E-01	2.037E-01	1.903E-01	4.873E-01
5.300E-02	1.834E-01	2.019E-01	1.889E-01	4.680E-01
5.400E-02	1.817E-01	2.002E-01	1.876E-01	4.501E-01
5.500E-02	1.802E-01	1.986E-01	1.864E-01	4.334E-01
5.600E-02	1.788E-01	1.972E-01	1.852E-01	4.180E-01
5.700E-02	1.774E-01	1.957E-01	1.841E-01	4.036E-01
5.800E-02	1.762E-01	1.944E-01	1.830E-01	3.902E-01
5.900E-02	1.749E-01	1.932E-01	1.820E-01	3.776E-01
6.000E-02	1.738E-01	1.920E-01	1.810E-01	3.659E-01
6.100E-02	1.727E-01	1.908E-01	1.801E-01	3.550E-01
6.200E-02	1.716E-01	1.897E-01	1.792E-01	3.447E-01
6.300E-02	1.706E-01	1.887E-01	1.784E-01	3.351E-01
6.400E-02	1.697E-01	1.877E-01	1.776E-01	3.261E-01
6.500E-02	1.688E-01	1.867E-01	1.768E-01	3.176E-01
6.600E-02	1.679E-01	1.858E-01	1.760E-01	3.096E-01
6.700E-02	1.670E-01	1.849E-01	1.753E-01	3.021E-01
6.800E-02	1.662E-01	1.840E-01	1.746E-01	2.950E-01
6.900E-02	1.654E-01	1.832E-01	1.739E-01	2.884E-01
7.000E-02	1.647E-01	1.824E-01	1.732E-01	2.820E-01
7.100E-02	1.639E-01	1.816E-01	1.725E-01	2.761E-01
7.200E-02	1.632E-01	1.808E-01	1.719E-01	2.704E-01
7.300E-02	1.625E-01	1.801E-01	1.713E-01	2.651E-01
7.400E-02	1.619E-01	1.794E-01	1.707E-01	2.600E-01
7.500E-02	1.612E-01	1.787E-01	1.701E-01	2.552E-01
7.600E-02	1.606E-01	1.780E-01	1.695E-01	2.506E-01
7.700E-02	1.600E-01	1.774E-01	1.689E-01	2.463E-01
7.800E-02	1.594E-01	1.767E-01	1.684E-01	2.422E-01
7.900E-02	1.588E-01	1.761E-01	1.678E-01	2.382E-01
8.000E-02	1.582E-01	1.755E-01	1.673E-01	2.345E-01
8.100E-02	1.577E-01	1.749E-01	1.668E-01	2.309E-01
8.200E-02	1.571E-01	1.743E-01	1.663E-01	2.275E-01
8.300E-02	1.566E-01	1.737E-01	1.657E-01	2.243E-01

```
        8.400E-02   1.561E-01   1.732E-01   1.653E-01   2.212E-01
        8.500E-02   1.556E-01   1.726E-01   1.648E-01   2.182E-01
        8.600E-02   1.550E-01   1.721E-01   1.643E-01   2.154E-01
        8.700E-02   1.546E-01   1.716E-01   1.638E-01   2.126E-01
        8.800E-02   1.541E-01   1.710E-01   1.633E-01   2.100E-01
        8.900E-02   1.536E-01   1.705E-01   1.629E-01   2.075E-01
        9.000E-02   1.531E-01   1.700E-01   1.624E-01   2.051E-01
        9.100E-02   1.527E-01   1.695E-01   1.620E-01   2.028E-01
        9.200E-02   1.522E-01   1.690E-01   1.615E-01   2.006E-01
        9.300E-02   1.518E-01   1.686E-01   1.611E-01   1.985E-01
        9.400E-02   1.513E-01   1.681E-01   1.607E-01   1.965E-01
        9.500E-02   1.509E-01   1.676E-01   1.603E-01   1.945E-01
        9.600E-02   1.505E-01   1.672E-01   1.598E-01   1.926E-01
        9.700E-02   1.501E-01   1.667E-01   1.594E-01   1.908E-01
        9.800E-02   1.497E-01   1.663E-01   1.590E-01   1.890E-01
        9.900E-02   1.493E-01   1.658E-01   1.586E-01   1.873E-01
        1.000E-01   1.489E-01   1.654E-01   1.582E-01   1.857E-01
        1.500E-01   1.332E-01   1.481E-01   1.420E-01   1.426E-01
        2.000E-01   1.220E-01   1.356E-01   1.302E-01   1.254E-01
        3.000E-01   1.061E-01   1.180E-01   1.133E-01   1.068E-01
        4.000E-01   9.514E-02   1.058E-01   1.016E-01   9.521E-02
        5.000E-01   8.690E-02   9.665E-02   9.278E-02   8.683E-02
        6.000E-01   8.040E-02   8.940E-02   8.583E-02   8.027E-02
        8.000E-01   7.065E-02   7.857E-02   7.542E-02   7.049E-02
        1.000E+00   6.353E-02   7.066E-02   6.782E-02   6.338E-02];


% Mass densities [g/cm^3]
rho_air = 0.0012;   % air (Searle, 1934)
rho_H2O = 1.00;     % water
rho_org = 1.41;     % organic matter (Katz and Li, 1973; Lees, 1987)
rho_HA  = 3.000;    % hydroxyapatite (Gong et al., 1964; Lees, 1987)


% X-ray attenuation coefficients [cm^(-1)]
mu_per_rho_air = mu_NIST(:,2);
mu_air         = mu_per_rho_air*rho_air;

mu_per_rho_H2O = mu_NIST(:,3);
mu_H2O         = mu_per_rho_H2O*rho_H2O;

mu_per_rho_col = mu_NIST(:,4);
mu_org         = mu_per_rho_col*rho_col;

mu_per_rho_HA  = mu_NIST(:,5);
mu_HA          = mu_per_rho_HA*rho_HA;

photon_energy  = mu_NIST(:,1)*1000; % -> [keV]


% Figure
figure1=figure
```

```
plot=semilogy(photon_energy,mu_HA,'k -.',photon_energy,mu_org,'k -',...
     photon_energy,mu_H2O,'k --',photon_energy,mu_air,'k .','LineWidth',3);
set(gca,'FontSize',16)
set(gcf,'Units','Inches','Position',[0, 0, 11, 8],'PaperUnits','Inches',...
        'PaperSize', [11, 8])
legend({'hydroxyapatite','collagen','water','air'},'Fontname','Times',...
        'Fontsize', 20);
xlabel('Photon energy [keV]','FontSize', 20, 'FontName', 'Times');
ylabel('\mu_{i} [cm^{-1}]','FontSize', 20, 'FontName', 'Times');
axis([5 40 10^(-4) 1000]);
grid on;
```

C.2 Probability density functions of the attenuation-related grey values of the sham rats

```
% Created by:           Patricia Hasslinger
% Based on code by:     Alexander Dejaco, Stefan Scheiner

folderpath = 'C:\Users\Patricia\Documents\Studium\Diplomarbeit\GrI_sham\';
fpath      = 'C:\Users\Patricia\Documents\Studium\Diplomarbeit\Figures';


% Loop over image stack folders
for k=1:10

    % Path to images within folders
    folder     = sprintf('%s%d%s',folderpath, k,'\*.tif');
    images     = dir(folder);
    num_images = length(images);

    hist_all   = zeros(1,256); % zero vector with length of 8-bit integers

    % Loop over images within folders
    for i=1:num_images
        % Imread images
        fname          = images(i).name;
        foldername     = sprintf('%s%d%s',folderpath, k, '\');
        s              = ([foldername fname]);
        slice          = imread(s);

        dim_x          = size(slice,1);
        dim_y          = size(slice,2);
        dim_z          = num_images;
        pixels         = dim_x*dim_y;
        voxels         = pixels*dim_z;

        volumes        = zeros(dim_x,dim_y,dim_z,'uint8');
        volumes(:,:,i) = double(uint8(slice));
        disp(['imported ',num2str(i),'/',num2str(num_images)]);

        slice_vec      = reshape(volumes(:,:,i),pixels,1);  % make vector
        n              = hist(slice_vec, 0:255);  % n...frequency count
        hist_all       = n+hist_all;
        eval( [['hist_all_' int2str(k)] '= hist_all'] );
    end


    % Plots of the histograms
    hist_gsc = figure
    axes_gsc = axes('Parent',hist_gsc,'FontWeight','bold','FontSize',16,...
                    'FontName', 'Times');
```

```
    a        = bar(0:255,hist_all/(voxels),'r');
    box(axes_gsc,'on');
    grid(axes_gsc,'on');
    hold(axes_gsc,'all');
    axis([0 255 0 0.04]);
    % Set yticks
    set(gca,'yTick', 0.00:0.01:0.04,'YTickLabel',...
        str2mat('0.00','0.01','0.02','0.03','0.04'))
    % Create xlabel
    xlabel('X-ray attenuation [GV]','FontSize',20,'FontWeight','bold',...
           'FontName', 'Times');
    % Create ylabel
    ylabel('Probability density [-]','FontSize',20,'FontWeight','bold',...
           'FontName','Times');
    % Save figures
    figlist=findobj('type','figure');
        for i=1:numel(figlist)
            saveas(figlist(i),fullfile(fpath,...
                   ['Histogram-GV_sham_' num2str(figlist(i)) '.fig']));
            saveas(figlist(i),fullfile(fpath,...
                   ['Histogram-GV_sham_' num2str(figlist(i)) '.jpeg']));
        end


    % Extract landmark grey values
    data       = hist_all/(voxels);
    [pks,locs] = findpeaks(data,'minpeakheight',0.002,'minpeakdistance',30)

    GV_air_k        = locs(1)
    GV_H2O_k        = locs(2)
    GV_bone_k       = locs(3)

    GV_air(k)       = [GV_air_k]
    GV_H2O(k)       = [GV_H2O_k]
    GV_bone(k)      = [GV_bone_k]

    GVm_air         = mean(GV_air)
    GVm_H2O         = mean(GV_H2O)
    GVm_bone        = mean(GV_bone)


    % Extract bone threshold grey values
    dataInv         = 1.01*max(data) - data;
    [Min,MinIdx]    = findpeaks(dataInv,'minpeakdistance',80);
    GV_threshold_k  = MinIdx(2) % GV_thr = 2nd minimum within 80GV
    GV_threshold(k) = [GV_threshold_k]
    GVm_threshold   = mean(GV_threshold)
end
```

C.3 Probability density functions of the attenuation-related grey values of the OVX rats

```
% Created by:           Patricia Hasslinger
% Based on code by:     Alexander Dejaco, Stefan Scheiner

folderpath = 'C:\Users\Patricia\Documents\Studium\Diplomarbeit\GrII_OVX\';
fpath      = 'C:\Users\Patricia\Documents\Studium\Diplomarbeit\Figures';


% Loop over image stack folders
for k=1:10

    % Path to images within folders
    folder     = sprintf('%s%d%s',folderpath, k,'\*.tif');
    images     = dir(folder);
    num_images = length(images);

    hist_all   = zeros(1,256); % zero vector with length of 8-bit integers

    % Loop over images within folders
    for i=1:num_images
        % Imread images
        fname          = images(i).name;
        foldername     = sprintf('%s%d%s',folderpath, k, '\');
        s              = ([foldername fname]);
        slice          = imread(s);

        dim_x          = size(slice,1);
        dim_y          = size(slice,2);
        dim_z          = num_images;
        pixels         = dim_x*dim_y;
        voxels         = pixels*dim_z;

        volumes        = zeros(dim_x,dim_y,dim_z,'uint8');
        volumes(:,:,i) = double(uint8(slice));
        disp(['imported ',num2str(i),'/',num2str(num_images)]);

        slice_vec      = reshape(volumes(:,:,i),pixels,1);  % make vector
        n              = hist(slice_vec, 0:255);  % n...frequency count
        hist_all       = n+hist_all;
        eval( [['hist_all_' int2str(k)] '= hist_all'] );
    end


    % Plots of the histograms
    hist_gsc = figure
    axes_gsc = axes('Parent',hist_gsc,'FontWeight','bold','FontSize',16,...
                    'FontName', 'Times');
```

```
    a        = bar(0:255,hist_all/(voxels),'r');
    box(axes_gsc,'on');
    grid(axes_gsc,'on');
    hold(axes_gsc,'all');
    axis([0 255 0 0.04]);
    % Set yticks
    set(gca,'yTick', 0.00:0.01:0.04,'YTickLabel',...
        str2mat('0.00','0.01','0.02','0.03','0.04'))
    % Create xlabel
    xlabel('X-ray attenuation [GV]','FontSize',20,'FontWeight','bold',...
           'FontName', 'Times');
    % Create ylabel
    ylabel('Probability density [-]','FontSize',20,'FontWeight','bold',...
           'FontName','Times');
    % Save figures
    figlist=findobj('type','figure');
        for i=1:numel(figlist)
            saveas(figlist(i),fullfile(fpath,...
                   ['Histogram-GV_OVX_' num2str(figlist(i)) '.fig']));
            saveas(figlist(i),fullfile(fpath,...
                   ['Histogram-GV_OVX_' num2str(figlist(i)) '.jpeg']));
        end


    % Extract landmark grey values
    data      = hist_all/(voxels);
    [pks,locs]= findpeaks(data,'minpeakheight',0.002,'minpeakdistance',35)

    GV_air_k       = locs(1)
    GV_H2O_k       = locs(2)
    GV_bone_k      = locs(3)

    GV_air(k)      = [GV_air_k]
    GV_H2O(k)      = [GV_H2O_k]
    GV_bone(k)     = [GV_bone_k]

    GVm_air        = mean(GV_air)
    GVm_H2O        = mean(GV_H2O)
    GVm_bone       = mean(GV_bone)


    % Extract bone threshold grey values
    dataInv        = 1.01*max(data) - data;
    [Min,MinIdx]   = findpeaks(dataInv,'minpeakdistance',80);
    GV_threshold_k = MinIdx(2) % GV_thr = 2nd minimum within 80GV
    GV_threshold(k)= [GV_threshold_k]
    GVm_threshold  = mean(GV_threshold)
end
```

C.4 Applied X-ray energy, a and b values and densities and attenuation coefficients of bone

```
clear all;

load('Attcoeff_NIST.mat', 'rho_HA', 'rho_H2O', 'rho_col',...
     'mu_HA', 'mu_H2O','mu_col', 'mu_air', 'photon_energy')

% Loop over sham or OVX rats
for t=1:2
    switch t
        case 1 % sham
            load('Histograms_GV_sham.mat','GV_air','GV_H2O','GV_bone')
            % Ash per organic weight acc. to Kim et al. (2009)
            WF_HA2org = 1.65*1.018; % factor considers volatizing mineral
        case 2 % OVX
            load('Histograms_GV_OVX.mat','GV_air', 'GV_H2O', 'GV_bone')
            % Ash per organic weight acc. to Kim et al. (2009)
            WF_HA2org = 1.55*1.018; % factor considers volatizing mineral
    end

    % Loop over image stack folders
    disp(['loop over image stacks...']);
    for k=1:10
        GV_air(k);
        GV_H2O(k);
        GV_bone(k);

        % Loop over the energies (keV)
        disp(['loop over energy...']);
        array=photon_energy;
        for ii = 1:length(array)
            element = array(ii);
            mu_H2O(ii);
            mu_air(ii);
            mu_col(ii);

            % Slope a and intersection b as functions of the X-ray energy
            % Initial equations:
            % mu_air = a*GV_air+b
            % mu_H2O = a*GV_H2O+b
            a(k,ii) = (mu_H2O(ii)-mu_air(ii))/(GV_H2O(k)-GV_air(k));
            b(k,ii) = (GV_H2O(k)*mu_air(ii)-GV_air(k)*mu_H2O(ii))/...
                        (GV_H2O(k)-GV_air(k));

            mu_bone(k,ii) = a(k,ii)*GV_bone(k)+b(k,ii);

            % Volume fraction of mineral within the solid bone tissue
            B         = WF_HA2org*rho_col/rho_HA;
```

```
            f_HA_bar  = 1/(1+1/B);

            % Attenuation coefficient & density of the solid bone tissue
            mu_solid(ii) = f_HA_bar*mu_HA(ii)+(1-f_HA_bar)*mu_col(ii);
            rho_solid    = f_HA_bar*rho_HA+(1-f_HA_bar)*rho_col;

            % Volume fractions
            % Initial equations:
            % mu_bone =a*GV_bone+b
            % mu_bone = f_H2O * mu_H2O + (1-f_H2O)*mu_solid (-> f_H2O)
            f_H2O(k,ii)  = (mu_bone(k,ii)-mu_solid(ii))/...
                           (mu_H2O(ii)-mu_solid(ii));
            f_org(k,ii)  = (1-f_HA_bar)*(1-f_H2O(k,ii));
            f_HA(k,ii)   = (mu_bone(k,ii)-mu_col(ii)*f_org(k,ii)-...
                        mu_H2O(ii)*(1-f_org(k,ii)))/(mu_HA(ii)-mu_H2O(ii));

            % Density of bone as function of the X-ray energy
            rhobone(k,ii)=f_H2O(k,ii)*rho_H2O+(1-f_H2O(k,ii))*rho_solid;
        end
    end

    % Assign results to sham or OVX rats
    if t==1
      rhobone_h=rhobone; rho_solid_h=rho_solid; mu_bone_h=mu_bone;
      mu_solid_h=mu_solid; a_h=a; b_h=b; f_org_h=f_org; f_H2O_h=f_H2O;
    else
      rhobone_o=rhobone; rho_solid_o=rho_solid; mu_bone_o=mu_bone;
      mu_solid_o=mu_solid; a_o=a; b_o=b; f_org_o=f_org; f_H2O_o=f_H2O;
    end
end


% Plot of rhobone as function of the X-ray energy
figure0=figure;
axes0 = axes('Parent',figure0,'FontWeight','bold','FontSize',16);
hold(axes0,'all');
grid (axes0,'on');
xaxis=photon_energy;
plot(xaxis,rhobone_h(1,:),'LineWidth',3,'Color',[0 0 0]);
plot(xaxis,rhobone_h(2,:),'LineWidth',1,'Color',[0 0 1]);
plot(xaxis,rhobone_h(3,:),'LineWidth',2,'LineStyle','--','Color',[0 0 1]);
plot(xaxis,rhobone_h(4,:),'LineWidth',2,'LineStyle','-.','Color',[0 0 1]);
plot(xaxis,rhobone_h(5,:),'LineWidth',3,'LineStyle',':','Color',[0 0 1]);
plot(xaxis,rhobone_h(6,:),'LineWidth',3,'Color',[0 0 0.6]);
plot(xaxis,rhobone_h(7,:),'LineWidth',1,'Color',[0 0 0.6]);
plot(xaxis,rhobone_h(8,:),'LineWidth',2,'LineStyle','--','Color',[0 0 0.6]);
plot(xaxis,rhobone_h(9,:),'LineWidth',2,'LineStyle','-.','Color',[0 0 0.6]);
plot(xaxis,rhobone_h(10,:),'LineWidth',3,'LineStyle',':','Color',[0 0 0.6]);
plot(xaxis,rhobone_o(1,:),'LineWidth',3,'Color',[1 0 0]);
plot(xaxis,rhobone_o(2,:),'LineWidth',1,'Color',[1 0 0]);
plot(xaxis,rhobone_o(3,:),'LineWidth',2,'LineStyle','--','Color',[1 0 0]);
plot(xaxis,rhobone_o(4,:),'LineWidth',2,'LineStyle','-.','Color',[1 0 0]);
```

```
plot(xaxis,rhobone_o(5,:),'LineWidth',3,'LineStyle',':','Color',[1 0 0]);
plot(xaxis,rhobone_o(6,:),'LineWidth',3,'Color',[0.7 0 0]);
plot(xaxis,rhobone_o(7,:),'LineWidth',1,'Color',[0.7 0 0]);
plot(xaxis,rhobone_o(8,:),'LineWidth',2,'LineStyle','--','Color',[0.7 0 0]);
plot(xaxis,rhobone_o(9,:),'LineWidth',2,'LineStyle','-.','Color',[0.7 0 0]);
plot(xaxis,rhobone_o(10,:),'LineWidth',3,'LineStyle',':','Color',[0.7 0 0]);
xlim([5 40]);
ylim([1.0 2.0]);
% Create xlabel
xlabel({'X-ray energy [keV]'},'FontWeight','bold','FontSize',20,...
    'FontName','Times');
% Create ylabel
set(gca,'yTick', 1.0:0.2:2.0)
set(gca,'YTickLabel',...
    char('1.0','1.2','1.4','1.6','1.8','2.0'))
ylabel({'\rho_{bone} [g/cm^3]'},'FontWeight','bold','FontSize',20,...
    'FontName','Times');
Create legend
legend0 = legend({'sham 1','sham 2','sham 3','sham 4','sham 5','sham 6',...
    'sham 7','sham 8','sham 9','sham 10','OVX 1','OVX 2','OVX 3',...
    'OVX 4', 'OVX 5','OVX 6', 'OVX 7', 'OVX 8', 'OVX 9','OVX 10'},...
    'Fontname', 'Times', 'Location', 'NorthEastOutside', 'Fontsize', 16);
hold off;

% Applied X-ray energy (e) and corresponding bone densities of the
% ultrastructure (rhobone)
data    = [rhobone_h(:,:); rhobone_o(:,:)]
[rho,e] = min(data,[],2);
e       = min(e)


%  Plot of slope a as function of the X-ray energy
figure0=figure;
axes0 = axes('Parent',figure0,'FontWeight','bold','FontSize',16);
hold(axes0,'all');
grid (axes0,'on');
xaxis=photon_energy;
plot(xaxis, a_h(1,:),'LineWidth',3,'Color',[0 0 1]);
plot(xaxis, a_h(2,:),'LineWidth',1,'Color',[0 0 1]);
plot(xaxis, a_h(3,:),'LineWidth',2,'LineStyle','--','Color',[0 0 1]);
plot(xaxis, a_h(4,:),'LineWidth',2,'LineStyle','-.','Color',[0 0 1]);
plot(xaxis, a_h(5,:),'LineWidth',3,'LineStyle',':','Color',[0 0 1]);
plot(xaxis, a_h(6,:),'LineWidth',3,'Color',[0 0 0.6]);
plot(xaxis, a_h(7,:),'LineWidth',1,'Color',[0 0 0.6]);
plot(xaxis, a_h(8,:),'LineWidth',2,'LineStyle','--','Color',[0 0 0.6]);
plot(xaxis, a_h(9,:),'LineWidth',2,'LineStyle','-.','Color',[0 0 0.6]);
plot(xaxis, a_h(10,:),'LineWidth',3,'LineStyle',':','Color',[0 0 0.6]);
plot(xaxis, a_o(1,:),'LineWidth',3,'Color',[1 0 0]);
plot(xaxis, a_o(2,:),'LineWidth',1,'Color',[1 0 0]);
plot(xaxis, a_o(3,:),'LineWidth',2,'LineStyle','--','Color',[1 0 0]);
plot(xaxis, a_o(4,:),'LineWidth',2,'LineStyle','-.','Color',[1 0 0]);
plot(xaxis, a_o(5,:),'LineWidth',3,'LineStyle',':','Color',[1 0 0]);
```

```
plot(xaxis, a_o(6,:),'LineWidth',3,'Color',[0.7 0 0]);
plot(xaxis, a_o(7,:),'LineWidth',1,'Color',[0.7 0 0]);
plot(xaxis, a_o(8,:),'LineWidth',2,'LineStyle','--','Color',[0.7 0 0]);
plot(xaxis, a_o(9,:),'LineWidth',2,'LineStyle','-.','Color',[0.7 0 0]);
plot(xaxis, a_o(10,:),'LineWidth',3,'LineStyle',':','Color',[0.7 0 0]);
xlim([0 40]);
ylim([0 110]);
% Create xlabel
xlabel({'Photon energy [keV]'},'FontWeight','bold','FontSize',20,...
    'FontName','Times');
% Create ylabel
ylabel({'Constant a'},'FontWeight','bold','FontSize',20,...
    'FontName','Times');
% Create legend
legend0 = legend({'sham 1','sham 2','sham 3','sham 4','sham 5','sham 6',...
    'sham 7','sham 8','sham 9','sham 10','OVX 1','OVX 2','OVX 3',...
    'OVX 4', 'OVX 5','OVX 6', 'OVX 7', 'OVX 8', 'OVX 9','OVX 10'},...
    'Fontname', 'Times', 'Location', 'NorthEast', 'Fontsize', 16);
hold off;

% Plot of intersection b as function of the X-ray energy
figure0=figure;
axes0 = axes('Parent',figure0,'FontWeight','bold','FontSize',16);
hold(axes0,'all');
grid (axes0,'on');
xaxis=photon_energy;
plot(xaxis, b_h(1,:),'LineWidth',3,'Color',[0 0 1]);
plot(xaxis, b_h(2,:),'LineWidth',1,'Color',[0 0 1]);
plot(xaxis, b_h(3,:),'LineWidth',2,'LineStyle','--','Color',[0 0 1]);
plot(xaxis, b_h(4,:),'LineWidth',2,'LineStyle','-.','Color',[0 0 1]);
plot(xaxis, b_h(5,:),'LineWidth',3,'LineStyle',':','Color',[0 0 1]);
plot(xaxis, b_h(6,:),'LineWidth',3,'Color',[0 0 0.6]);
plot(xaxis, b_h(7,:),'LineWidth',1,'Color',[0 0 0.6]);
plot(xaxis, b_h(8,:),'LineWidth',2,'LineStyle','--','Color',[0 0 0.6]);
plot(xaxis, b_h(9,:),'LineWidth',2,'LineStyle','-.','Color',[0 0 0.6]);
plot(xaxis, b_h(10,:),'LineWidth',3,'LineStyle',':','Color',[0 0 0.6]);
plot(xaxis, b_o(1,:),'LineWidth',3,'Color',[1 0 0]);
plot(xaxis, b_o(2,:),'LineWidth',1,'Color',[1 0 0]);
plot(xaxis, b_o(3,:),'LineWidth',2,'LineStyle','--','Color',[1 0 0]);
plot(xaxis, b_o(4,:),'LineWidth',2,'LineStyle','-.','Color',[1 0 0]);
plot(xaxis, b_o(5,:),'LineWidth',3,'LineStyle',':','Color',[1 0 0]);
plot(xaxis, b_o(6,:),'LineWidth',3,'Color',[0.7 0 0]);
plot(xaxis, b_o(7,:),'LineWidth',1,'Color',[0.7 0 0]);
plot(xaxis, b_o(8,:),'LineWidth',2,'LineStyle','--','Color',[0.7 0 0]);
plot(xaxis, b_o(9,:),'LineWidth',2,'LineStyle','-.','Color',[0.7 0 0]);
plot(xaxis, b_o(10,:),'LineWidth',3,'LineStyle',':','Color',[0.7 0 0]);
xlim([0 40]);
ylim([-4500 0]);
% Create xlabel
xlabel({'Photon energy [keV]'},'FontWeight','bold','FontSize',20,...
    'FontName','Times');
% Create ylabel
```

```
ylabel({'Constant b'},'FontWeight','bold','FontSize',20,...
    'FontName','Times');
% Create legend
legend0 = legend({'sham 1','sham 2','sham 3','sham 4','sham 5','sham 6',...
    'sham 7','sham 8','sham 9','sham 10','OVX 1','OVX 2','OVX 3',...
    'OVX 4', 'OVX 5','OVX 6', 'OVX 7', 'OVX 8', 'OVX 9','OVX 10'},...
    'Fontname', 'Times', 'Location', 'SouthEast', 'Fontsize', 16);
hold off;

% Plot of fH2O as function of the X-ray energy
figure0=figure;
axes0 = axes('Parent',figure0,'FontWeight','bold','FontSize',16);
hold(axes0,'all');
grid (axes0,'on');
xaxis=photon_energy;
plot(xaxis, f_H2O_h(1,:),'LineWidth',3,'Color',[0 0 1]);
plot(xaxis, f_H2O_h(2,:),'LineWidth',1,'Color',[0 0 1]);
plot(xaxis, f_H2O_h(3,:),'LineWidth',2,'LineStyle','--','Color',[0 0 1]);
plot(xaxis, f_H2O_h(4,:),'LineWidth',2,'LineStyle','-.','Color',[0 0 1]);
plot(xaxis, f_H2O_h(5,:),'LineWidth',3,'LineStyle',':','Color',[0 0 1]);
plot(xaxis, f_H2O_h(6,:),'LineWidth',3,'Color',[0 0 0.6]);
plot(xaxis, f_H2O_h(7,:),'LineWidth',1,'Color',[0 0 0.6]);
plot(xaxis, f_H2O_h(8,:),'LineWidth',2,'LineStyle','--','Color',[0 0 0.6]);
plot(xaxis, f_H2O_h(9,:),'LineWidth',2,'LineStyle','-.','Color',[0 0 0.6]);
plot(xaxis, f_H2O_h(10,:),'LineWidth',3,'LineStyle',':','Color',[0 0 0.6]);
plot(xaxis, f_H2O_o(1,:),'LineWidth',3,'Color',[1 0 0]);
plot(xaxis, f_H2O_o(2,:),'LineWidth',1,'Color',[1 0 0]);
plot(xaxis, f_H2O_o(3,:),'LineWidth',2,'LineStyle','--','Color',[1 0 0]);
plot(xaxis, f_H2O_o(4,:),'LineWidth',2,'LineStyle','-.','Color',[1 0 0]);
plot(xaxis, f_H2O_o(5,:),'LineWidth',3,'LineStyle',':','Color',[1 0 0]);
plot(xaxis, f_H2O_o(6,:),'LineWidth',3,'Color',[0.7 0 0]);
plot(xaxis, f_H2O_o(7,:),'LineWidth',1,'Color',[0.7 0 0]);
plot(xaxis, f_H2O_o(8,:),'LineWidth',2,'LineStyle','--','Color',[0.7 0 0]);
plot(xaxis, f_H2O_o(9,:),'LineWidth',2,'LineStyle','-.','Color',[0.7 0 0]);
plot(xaxis, f_H2O_o(10,:),'LineWidth',3,'LineStyle',':','Color',[0.7 0 0]);
xlim([5 40]);
ylim([0.0 1.0]);
% Create xlabel
xlabel({'Photon energy [keV]'},'FontWeight','bold','FontSize',20,...
    'FontName','Times');
% Create ylabel
set(gca,'yTick', 0.0:0.2:1.0)
set(gca,'YTickLabel',...
    char('0.0','0.2','0.4','0.6','0.8','1.0'))
ylabel({'f_{H2O} [-]'},'FontWeight','bold','FontSize',20,...
    'FontName','Times');
% Create legend
legend0 = legend({'sham 1','sham 2','sham 3','sham 4','sham 5','sham 6',...
    'sham 7','sham 8','sham 9','sham 10','OVX 1','OVX 2','OVX 3',...
    'OVX 4', 'OVX 5','OVX 6', 'OVX 7', 'OVX 8', 'OVX 9','OVX 10'},...
    'Fontname', 'Times', 'Location', 'NorthEastOutside', 'Fontsize', 16);
hold off;
```

C.5 Probability density functions of the attenuation coefficients of the sham and OVX rats

```
clc; clear all;

load('Rhobone_vs_Photonenergy_KIM_neu.mat', 'a_h', 'b_h', 'a_o', 'b_o', 'e')
fpath      = 'C:\Users\Patricia\Documents\Studium\Diplomarbeit\Figures\';
filepath   = 'C:\Users\Patricia\Documents\Studium\Diplomarbeit\'

% Loop over sham or OVX rats
for t=1:2
    switch t
        case 1 % sham
            a=a_h; b=b_h;
            folderpath = [filepath '\GrI_healthy\']
            color      = 'b'
            imname     = 'Attcoeff_sham';
        case 2 % OVX
            a=a_o; b=b_o;
            folderpath = [filepath '\GrII_ovariectomized\']
            color      = 'r'
            imname     = 'Attcoeff_OVX';
    end

    % Loop over image stack folders
    for k = 1:10
        disp(['loop over image stacks...']);
        folder      = sprintf('%s%d%s',folderpath, k,'\*.tif');
        foldername  = sprintf('%s%d%s',folderpath, k, '\');
        images      = dir(folder);
        num_images  = length(images);
        hist_all    = zeros(1,256);

        for i = 1:num_images
        % Imread images
            fname          = images(i).name;
            s              = ([foldername fname]);
            slice          = imread(s);

            dim_x          = size(slice,1);
            dim_y          = size(slice,2);
            dim_z          = num_images;
            pixels         = dim_x*dim_y;
            voxels         = pixels*dim_z;

            volumes        = zeros(dim_x,dim_y,dim_z,'uint8');
            volumes(:,:,i) = double(uint8(slice));
            disp(['imported ',num2str(i),'/',num2str(num_images)]);
```

```
            slice_vec      = reshape(volumes(:,:,i),pixels,1);
            n              = hist(slice_vec, 0:255);
            hist_all       = n+hist_all;
            eval( [['hist_all_' int2str(k)] '= hist_all'] );
        end

        % Plots of the histograms
        bins=0:255;
        hist_attcoeff=figure
        axes_attcoeff=axes('Parent', hist_attcoeff, 'FontWeight',...
                           'bold', 'FontSize', 16, 'FontName', 'Times');
        bar(a(k,e)*bins+b(k,e), hist_all/(voxels), color);
        box(axes_attcoeff,'on');
        grid(axes_attcoeff,'on');
        hold(axes_attcoeff,'all');
        axis([0 15 0 0.04]);
        % Set yticks
        set(gca,'yTick', 0.00:0.01:0.04)
        set(gca,'YTickLabel', str2mat('0.00','0.01','0.02','0.03','0.04'))
        % Create xlabel
        xlabel('X-ray attenuation coefficient \mu [cm^{-1}]',...
               'FontSize', 20, 'FontWeight', 'bold', 'FontName', 'Times');
        % Create ylabel
        ylabel('Probability density [-]', 'FontSize',20, 'FontWeight',...
               'bold', 'FontName', 'Times');
        % Save figure as .png
        saveas(hist_attcoeff,[fpath, imname num2str(k), '.png'], 'png');
    end
end
```

C.6 Voxel-specific volume fractions

```
clear all
clc

% File path for figures
fpath='C:\Users\Patricia\Documents\Studium\Diplomarbeit\Figures\'

% Import data
load('Attcoeff_NIST.mat', 'rho_HA','rho_H2O','rho_col','mu_HA','mu_H2O',...
     'mu_col','mu_air')
load('Values_depon_Photonenergy.mat', 'e','f_org_h','f_org_o','a_h',...
     'a_o','b_h','b_o','mu_solid_h','mu_solid_o','mu_bone_h','mu_bone_o')

% Loop over image stack folders
for k=1:10
    % Loop over sham or OVX rats
    for t=1:2
        switch t
           case 1 % sham
                load('Histograms_GV_sham.mat', 'GV_threshold')

                % Spec. of the imorted data for the identified X-ray energy
                GV_thr_h   = GV_threshold;
                a_h        = a_h(k,e);
                b_h        = b_h(k,e);
                forg_h     = mean(f_org_h(:,e));
                mu_solid_h = mu_solid_h(e);
                mu_bone_h  = mu_bone_h(k,e);

                % Voxel-specific attenuation coefficient of bone
                rangeGS    = 0:255;
                rangemu_h  = rangeGS*a_h + b_h;

                % Voxel-specific volume fractions
                for i=1:length(rangemu_h)
                    mu_h   = rangemu_h(i);

                    fH2O_h(i)       = (mu_h-forg_h*mu_col(e)-(1-forg_h)...
                                        *mu_HA(e))/(mu_H2O(e)-mu_HA(e))
                    fHA_h(i)        = 1-forg_h-fH2O_h(i);
                    rhobone_h(i)    = fH2O_h(i)*rho_H2O+forg_h*rho_col+...
                                        fHA_h(i)*rho_HA;

                    f_HA_h(k,i)     = fHA_h(i);
                    f_H2O_h(k,i)    = fHA_h(i);
                    rho_bone_h(k,i) = rhobone_h(i);
                end

%%%%%%%%%%%%%%%%%%%%%%%%%%%%%%%%%%%%%%%%%%%%%%%%%%%%%%%%%%%%%%%%%%%%%%%%%%%%%%%
```

```
% Plot of the voxel-specific volume fractions of the sham rats
x=rangeGS
figure0=figure;
axes0 = axes('Parent', figure0, 'FontWeight', 'bold', 'FontSize', 16);
hold(axes0,'all');
box(axes0,'on');
grid(axes0,'on');
plot(x, fH2O_h, 'LineStyle', ':', 'Color', [0 0 1], 'LineWidth', 2);
plot(x, forg_h*ones(1,256),'LineStyle','--','Color',[0 0 1],'LineWidth',2);
plot(x, fHA_h,'LineStyle','-','Color',[0 0 1],'LineWidth',2);
% Set xlim and xticks
xlim([GV_thr_h(k)+1 255]);
set(gca, 'XTick', 125:25:250, 'XTicklabel',...
        {'125','150','175','200','225','250'});
% Set ylim and yticks
ylim([0 1]);
set(gca, 'YTick', 0:0.2:1, 'YTicklabel',...
        {'0.0','0.2', '0.4','0.6', '0.8','1.0'});
% Create legend
legend({'f_{H_2O}','f_{org}','f_{HA}'}, 'Fontname', 'Times', 'Location',...
        'NorthWest','Fontsize',20)
% Create xlabel
xlabel({'Grey values (GV)'}, 'FontWeight', 'bold', 'FontSize', 20,...
        'FontName', 'Times');
% Create ylabel
ylabel({'Volume fractions [-]'}, 'FontWeight', 'bold', 'FontSize', 20,...
        'FontName', 'Times');
hold off;
% Save figure as .png
saveas(gcf,[fpath, 'Volume_fractions_sham' num2str(k), '.png'], 'png');
%%%%%%%%%%%%%%%%%%%%%%%%%%%%%%%%%%%%%%%%%%%%%%%%%%%%%%%%%%%%%%%%%%%%%%%%%%%%%%%

            case 2 % OVX
                load('Histograms_GV_OVX.mat', 'GV_threshold')

                % Spec. of the imorted data for the identified X-ray energy
                GV_thr_o   = GV_threshold;
                a_o        = a_o(k,e);
                b_o        = b_o(k,e);
                forg_o     = mean(f_org_o(:,e));
                mu_solid_o = mu_solid_o(e);
                mu_bone_o  = mu_bone_o(k,e);

                % Voxel-specific attenuation coefficient of bone
                rangemu_o  = rangeGS*a_o + b_o;

                % Voxel-specific volume fractions
                for i=1:length(rangemu_o)
                    mu_o   = rangemu_o(i);

                    fH2O_o(i)       = (mu_o-forg_o*mu_col(e)-(1-forg_o)...
                                        *mu_HA(e))/(mu_H2O(e)-mu_HA(e));
```

```
                    fHA_o(i)        = 1-forg_o-fH2O_o(i);
                    rhobone_o(i)    = fH2O_o(i)*rho_H2O+forg_o*rho_col+...
                                      fHA_o(i)*rho_HA;

                    f_HA_o(k,i)     = fHA_o(i);
                    f_H2O_o(k,i)    = fHA_o(i);
                    rho_bone_o(k,i) = rhobone_o(i);
                end

%%%%%%%%%%%%%%%%%%%%%%%%%%%%%%%%%%%%%%%%%%%%%%%%%%%%%%%%%%%%%%%%%%%%%%%%%%%%%%%
% Plot of the voxel-specific volume fractions of the OVX rats
figure0=figure;
axes0 = axes('Parent', figure0, 'FontWeight', 'bold', 'FontSize', 16);
hold(axes0,'all');
box(axes0,'on');
grid(axes0,'on');
plot(x, fH2O_o, 'LineStyle', ':', 'Color', [1 0 0], 'LineWidth', 2);
plot(x, forg_o*ones(1,256),'LineStyle','--','Color',[1 0 0],'LineWidth',2);
plot(x, fHA_o, 'LineStyle', '-', 'Color', [1 0 0], 'LineWidth', 2);
% Set xlim and xticks
xlim([GV_thr_o(k)+1 255]);
set(gca, 'XTick', 125:25:250, 'XTicklabel',...
       {'125','150','175','200','225','250'});
% Set ylim and yticks
ylim([0 1]);
set(gca, 'YTick', 0:0.2:1, 'YTicklabel',...
       {'0.0','0.2', '0.4','0.6', '0.8','1.0'});
% Create legend
legend({'f_{H_2O}','f_{org}','f_{HA}'}, 'Fontname', 'Times', 'Location',...
       'NorthWest', 'Fontsize', 20)
% Create xlabel
xlabel({'Grey values (GV)'}, 'FontWeight', 'bold','FontSize', 20,...
       'FontName','Times');
% Create ylabel
ylabel({'Volume fractions [-]'}, 'FontWeight', 'bold', 'FontSize', 20,...
       'FontName', 'Times');
hold off;
% Save figure as .png
saveas(gcf, [fpath, 'Volume_fractions_OVX' num2str(k) , '.png'], 'png');
%%%%%%%%%%%%%%%%%%%%%%%%%%%%%%%%%%%%%%%%%%%%%%%%%%%%%%%%%%%%%%%%%%%%%%%%%%%%%%%
        end
    end
end
```

C.7 Voxel-specific elastic properties for sham and OVX rats

```
% Created by: Claire Morin, 2012
% Adapted by: Patricia Hasslinger, Viktoria Vass

clear all

% DEFINITIONS
%-------------------------------------------------------------------------
rhowater = 1 ;
% Unity tensor
I = [1 0 0 0 0 0; 0 1 0 0 0 0; 0 0 1 0 0 0;...
     0 0 0 1 0 0; 0 0 0 0 1 0; 0 0 0 0 0 1];
% Volumetric part
J = [1/3 1/3 1/3 0 0 0; 1/3 1/3 1/3 0 0 0; 1/3 1/3 1/3 0 0 0;...
     0 0 0 0 0 0; 0 0 0 0 0 0; 0 0 0 0 0 0];
% Deviatoric part
K = I-J;
% Second-order unit tensor
one2=eye(3);

% NEEDLE FAMILIES HA
%-------------------------------------------------------------------------
% Total number of families between 0..pi/2 and for phi between 0 and pi
max_fam_theta = 20;
max_fam_phi   = 20;
max_fam       = max_fam_theta*max_fam_phi ;
% Increments theta and phi for integration
incr_theta    = pi/max_fam_theta;
incr_phi      = 2*pi/max_fam_phi;
% Families: support points for calculation of strain
vector_theta_fam_i = [(incr_theta/2):incr_theta:(pi-incr_theta/2)];
vector_phi_fam_i   = [(incr_phi/2):incr_phi:(2*pi-incr_phi/2)];


% DETERMINATION OF THE VOXEL-SPECIFIC ELASTIC STIFFNESS
%-------------------------------------------------------------------------
% Import voxel-specific volume fractions (=input)
load('Volume_fractions','f_HA_h','f_H2O_h','forg_h','GV_thr_h')
fpath= 'C:\Users\Patricia\Documents\Studium\Diplomarbeit\Figures\'

% Loop over image stack folders
for k=1:10
    % Loop over bone range
    for i=(GV_thr_h(k)+1):256
        barfHA    = f_HA_h(k,i);
        barfcol   = forg_h;
        barfwater = f_H2O_h(k,i) ;

        calcbonestiffness;
```

```
    dultra=inv(cultra) % inverse of stiffness tensor

    C1111(k,i)= cultra(1,1);   %=C2222
    C3333(k,i)= cultra(3,3);
    C1122(k,i)= cultra(1,2);
    C1133(k,i)= cultra(1,3);   %=C2233
    C2323(k,i)= cultra(4,4)/2; %=C1313
    C1212(k,i)= cultra(6,6)/2;
    E1(k,i)   = 1/(dultra(1,1));
    E3(k,i)   = 1/(dultra(3,3));
    nu12(k,i) = -dultra(1,2)*E1(k,i);
    nu13(k,i) = -dultra(1,3)*E3(k,i);
    G12(k,i)  = E1(k,i)/(2*(1+nu12(k,i)));
end


% Figure: Stiffness tensor components
x=0:255;
xm = nan(size(x));
xm(5:5:255) = x(5:5:255);
xn = nan(size(x));
xn(3:3:255) = x(3:3:255);
figure0=figure;
axes0 = axes('Parent', figure0, 'FontWeight', 'bold', 'FontSize', 16);
hold(axes0,'all');
box(axes0,'on');
grid(axes0,'on');
plot(x, C1111(k,:), 'LineStyle', '-.', 'Color', 'b', 'LineWidth', 1);
plot(xm, C3333(k,:), 'Marker', 's', 'MarkerSize', 3,...
    'MarkerFaceColor', 'b', 'Color', 'b');
    hA=plot(x, C3333(k,:), 'Color', 'b', 'LineWidth', 1);
plot(x, C1122(k,:), 'LineStyle', ':', 'Color', 'b', 'LineWidth', 2);
plot(xn, C1133(k,:),'Marker','d', 'MarkerSize', 3,...
    'MarkerFaceColor', 'b', 'Color', 'b');
    hB= plot(x, C1133(k,:), 'Color','b', 'LineWidth', 1);
plot(x, C1212(k,:), 'Color','b', 'LineWidth', 1);
plot(x, C2323(k,:), 'LineStyle', '--', 'Color', 'b', 'LineWidth', 1);
% Set xlim and xticks
xlim([GV_thr_h(k) 255]);
set(gca, 'XTick', 125:25:250, 'XTicklabel',...
        {'125','150','175','200','225','250'});
% Set ylim and yticks
ylim([0 20]);
set(gca, 'YTick', 0:5:20, 'YTicklabel', {'0','5','10','15','20'});
% Create legend
legend({'C_{1111}=C_{2222}','C_{3333}','C_{1122}',...
    'C_{1133}=C_{2233}','C_{1212}','C_{1313}=C_{2323}'},...
        'Fontname', 'Times', 'Location', 'NorthWest','Fontsize', 20)
% Create xlabel
xlabel({'Grey values (GV)'}, 'FontWeight', 'bold','FontSize', 20,...
        'FontName','Times');
% Create ylabel
```

```
ylabel({'Stiffness tensor components [GPa]'}, 'FontWeight','bold',...
        'FontSize', 20, 'FontName', 'Times');
% No extra legend entry for marker
set(get(get(hB,'Annotation'),'LegendInformation'),...
    'IconDisplayStyle','off');
set(get(get(hA,'Annotation'),'LegendInformation'),...
    'IconDisplayStyle','off');
hold off;
% Save figure as .png
saveas(gcf, [fpath 'Ctensor_GV_h' num2str(k) , '.png'], 'png');

% Figure: Young's and shear moduli E1, E3 and G12
figure0=figure;
axes0 = axes('Parent',figure0,'FontWeight','bold','FontSize',16);
hold(axes0,'all');
box(axes0,'on');
grid(axes0,'on');
plot(x, E1(k,:), 'Color', 'b', 'LineWidth', 2);
plot(x, E3(k,:), 'LineStyle', ':', 'Color', 'b', 'LineWidth', 2);
plot(x, G12(k,:), 'LineStyle', '--', 'Color', 'b', 'LineWidth', 2);
% Set xlim and xticks
xlim([GV_thr_h(k) 255]);
set(gca, 'XTick', 125:25:250, 'XTicklabel',...
        {'125','150','175','200','225','250'});
% Set ylim and yticks
ylim([0 10]);
set(gca, 'YTick', 0:2:10, 'YTicklabel', {'0','2','4','6','8','10'});
% Create legend
legend({'E_1','E_3','G_{12}'}, 'Fontname','Times', 'Location',...
        'NorthWest','Fontsize', 20)
% Create xlabel
xlabel({'Grey values (GV)'}, 'FontWeight', 'bold', 'FontSize', 20,...
        'FontName', 'Times');
% Create ylabel
ylabel({'Young''s and shear moduli [GPa]'}, 'FontWeight', 'bold',...
        'FontSize', 20, 'FontName', 'Times');
hold off;
% Save figure as .png
saveas(gcf, [fpath, 'E-G_Moduli_h' num2str(k) , '.png'], 'png');

% Figure: Poisson's ratios nu12 and nu13
figure0=figure;
axes0 = axes('Parent',figure0,'FontWeight','bold','FontSize',16);
hold(axes0,'all');
box(axes0,'on');
grid(axes0,'on');
plot(x, nu12(k,:),'Color','b', 'LineWidth', 2);
plot(x, nu13(k,:),'LineStyle','--','Color','b', 'LineWidth', 2);
% Set xlim and xticks
xlim([GV_thr_h(k) 255]);
set(gca, 'XTick', 125:25:250, 'XTicklabel',...
        {'125','150','175','200','225','250'});
```

```
    % Set ylim and yticks
    ylim([0 1]);
    set(gca, 'YTick',0:0.2:1, 'YTicklabel',...
            {'0.0','0.2', '0.4','0.6', '0.8','1.0'});
    % Create legend
    legend({'\nu_{12}','\nu_{13}=\nu_{23}'}, 'Fontname', 'Times',...
        'Location', 'NorthWest', 'Fontsize', 20)
    % Create xlabel
    xlabel({'Grey values (GV)'}, 'FontWeight', 'bold', 'FontSize', 20,...
        'FontName','Times');
    % Create ylabel
    ylabel({'Poisson''s ratios [-]'}, 'FontWeight', 'bold', 'FontSize',...
        20, 'FontName', 'Times');
    hold off;
    % Save figure as .png
    saveas(gcf, [fpath, 'Poisson-ratios_h' num2str(k) , '.png'], 'png');
end
```

```
% Created by: Claire Morin, 2012
% Adapted by: Patricia Hasslinger, Viktoria Vass
clear all

% DEFINITIONS
%-------------------------------------------------------------------------
rhowater = 1 ;
% Unity tensor
I = [1 0 0 0 0 0; 0 1 0 0 0 0; 0 0 1 0 0 0;...
     0 0 0 1 0 0; 0 0 0 0 1 0; 0 0 0 0 0 1];
% Volumetric part
J = [1/3 1/3 1/3 0 0 0; 1/3 1/3 1/3 0 0 0; 1/3 1/3 1/3 0 0 0;
     0 0 0 0 0 0; 0 0 0 0 0 0; 0 0 0 0 0 0];
% Deviatoric part
K = I-J;
% Second-order unit tensor
one2=eye(3);

% NEEDLE FAMILIES HA
%-------------------------------------------------------------------------
% Total number of families between 0..pi/2 and for phi between 0 and pi
max_fam_theta = 20;
max_fam_phi   = 20;
max_fam       = max_fam_theta*max_fam_phi;

% Increments theta and phi for integration
incr_theta    = pi/max_fam_theta;
incr_phi      = 2*pi/max_fam_phi;

% Families: support points for calculation of strain
vector_theta_fam_i = [(incr_theta/2):incr_theta:(pi-incr_theta/2)];
vector_phi_fam_i   = [(incr_phi/2):incr_phi:(2*pi-incr_phi/2)];


% DETERMINATION OF THE VOXEL-SPECIFIC ELASTIC STIFFNESS
%-------------------------------------------------------------------------
% Import voxel-specific volume fractions (=input)
load('Volume_fractions','f_HA_o','f_H2O_o','forg_o','GV_thr_o')
fpath= 'C:\Users\Patricia\Documents\Studium\Diplomarbeit\Figures\'

% Loop over image stack folders
for k=1:10
    % Loop over bone range
    for i=(GV_thr_o(k)+1):256
        barfHA    = f_HA_o(k,i);
        barfcol   = forg_o;
        barfwater = f_H2O_o(k,i) ;

        calcbonestiffness;
        dultra=inv(cultra) % inverse of stiffness tensor

        C1111(k,i)= cultra(1,1);   %=C2222
```

```
    C3333(k,i)= cultra(3,3);
    C1122(k,i)= cultra(1,2);
    C1133(k,i)= cultra(1,3);   %=C2233
    C2323(k,i)= cultra(4,4)/2; %=C1313
    C1212(k,i)= cultra(6,6)/2;
    E1(k,i)   = 1/(dultra(1,1));
    E3(k,i)   = 1/(dultra(3,3));
    nu12(k,i) = -dultra(1,2)*E1(k,i);
    nu13(k,i) = -dultra(1,3)*E3(k,i);
    G12(k,i)  = E1(k,i)/(2*(1+nu12(k,i)));
end


% Figure: Stiffness tensor components
x=0:255;
xm = nan(size(x));
xm(5:5:255) = x(5:5:255);
xn = nan(size(x));
xn(3:3:255) = x(3:3:255);
figure0=figure;
axes0 = axes('Parent', figure0, 'FontWeight', 'bold', 'FontSize', 16);
hold(axes0,'all');
box(axes0,'on');
grid(axes0,'on');
plot(x, C1111(k,:), 'LineStyle', '-.', 'Color', 'r', 'LineWidth', 1);
plot(xm, C3333(k,:), 'Marker', 's', 'MarkerSize', 3,...
    'MarkerFaceColor', 'r', 'Color', 'r');
    hA=plot(x, C3333(k,:), 'Color', 'r', 'LineWidth', 1);
plot(x, C1122(k,:), 'LineStyle',':','Color','r', 'LineWidth', 2);
plot(xn, C1133(k,:), 'Marker', 'd', 'MarkerSize', 3,...
    'MarkerFaceColor', 'r', 'Color', 'r');
    hB= plot(x, C1133(k,:), 'Color', 'r', 'LineWidth', 1);
plot(x, C1212(k,:), 'Color', 'r', 'LineWidth', 1);
plot(x, C2323(k,:), 'LineStyle', '--', 'Color', 'r', 'LineWidth', 1);
% Set xlim and xticks
xlim([GV_thr_o(k) 255]);
set(gca, 'XTick', 125:25:250, 'XTicklabel',...
        {'125','150','175','200','225','250'});
% Set ylim and yticks
ylim([0 20]);
set(gca, 'YTick', 0:5:20, 'YTicklabel', {'0','5','10','15','20'});
% Create legend
legend({'C_{1111}=C_{2222}', 'C_{3333}', 'C_{1122}',...
        'C_{1133}=C_{2233}', 'C_{1313}=C_{2323}'},...
        'Fontname', 'Times', 'Location', 'NorthWest','Fontsize', 20)
% Create xlabel
xlabel({'Grey values (GV)'}, 'FontWeight', 'bold','FontSize', 20,...
        'FontName','Times');
% Create yxlabel
ylabel({'Stiffness tensor components [GPa]'}, 'FontWeight', 'bold',...
        'FontSize', 20, 'FontName', 'Times');
% No extra legend entry for marker
```

```
set(get(get(hB,'Annotation'),'LegendInformation'),...
    'IconDisplayStyle','off');
set(get(get(hA,'Annotation'),'LegendInformation'),...
    'IconDisplayStyle','off');
hold off;
% Save figure as .png
saveas(gcf, [fpath, 'Ctensor_GV_o' num2str(k) , '.png'], 'png');

% Figure: Young's and shear moduli E1, E3 and G12
figure0=figure;
axes0 = axes('Parent',figure0,'FontWeight','bold','FontSize',16);
hold(axes0,'all');
box(axes0,'on');
grid(axes0,'on');
plot(x, E1(k,:),'Color','r', 'LineWidth', 2);
plot(x, E3(k,:),'LineStyle',':','Color','r', 'LineWidth', 2);
plot(x, G12(k,:),'LineStyle','--','Color','r', 'LineWidth', 2);
% Set xlim and xticks
xlim([GV_thr_o(k) 255]);
set(gca, 'XTick', 125:25:250, 'XTicklabel',...
       {'125','150','175','200','225','250'});
% Set ylim and yticks
ylim([0 10]);
set(gca, 'YTick', 0:2:10, 'YTicklabel', {'0','2','4','6','8','10'});
% Create legend
legend({'E_1','E_3','G_{12}'}, 'Fontname','Times', 'Location',...
       'NorthWest','Fontsize', 20)
% Create xlabel
xlabel({'Grey values (GV)'}, 'FontWeight', 'bold','FontSize', 20,...
       'FontName','Times');
% Create ylabel
ylabel({'Young''s and shear moduli [GPa]'}, 'FontWeight','bold',...
       'FontSize', 20, 'FontName', 'Times');
hold off;
% Save figure as .png
 saveas(gcf, [fpath, 'E-G_Moduli_OVX' num2str(k) , '.png'], 'png');

% Figure: Poisson's ratios nu12 and nu13
figure0=figure;
axes0 = axes('Parent',figure0,'FontWeight','bold','FontSize',16);
hold(axes0,'all');
box(axes0,'on');
grid(axes0,'on');
plot(x, nu12(k,:), 'Color', 'r', 'LineWidth', 2);
plot(x, nu13(k,:), 'LineStyle', '--', 'Color', 'r', 'LineWidth', 2);
% Set xlim and xticks
xlim([GV_thr_o(k) 255]);
set(gca, 'XTick', 125:25:250, 'XTicklabel',...
        {'125','150','175','200','225','250'});
% Set ylim and yticks
ylim([0 1]);
set(gca, 'YTick', 0:0.2:1, 'YTicklabel',...
```

```
            {'0.0','0.2', '0.4','0.6', '0.8','1.0'});
    % Create legend
    legend({'\nu_{12}','\nu_{13}=\nu_{23}'}, 'Fontname', 'Times',...
        'Location', 'NorthWest', 'Fontsize', 20)
    % Create xlabel
    xlabel({'Grey values (GV)'}, 'FontWeight', 'bold', 'FontSize', 20,...
        'FontName','Times');
    % Create ylabel
    ylabel({'Poisson''s ratios [-]'}, 'FontWeight', 'bold', 'FontSize',...
        20, 'FontName', 'Times');
    hold off;
    % Save figure as .png
     saveas(gcf, [fpath, 'Poisson-ratios_OVX' num2str(k) , '.png'], 'png');
end
```

C.7.1 Calculation of the bone stiffness of the ultrastructure

```
% Created by: Claire Morin, 2012

% 4-step-homogeniziation-model: wet collagen (MT), fibrils (SCS),
%               extrafibrillar space (SCS), ultrastructure (SCS)


% STIFFNESSES of the elementary components
%-------------------------------------------------------------------------
% Collagen
load ccol1.mat ;

% Hydroxyapatite
kHA  = 82.6;
muHA = 44.9;
cHA  = 2*muHA*K+3*kHA*J;

% Micropores
k_mupores  = 2.3;
mu_mupores = 0;
c_mupores  = 3*k_mupores*J;

% Intercrystalline space
kic  = 2.3;
muic = 0.;
cic  = 3*kic*J;

% Water in intermolecular space
cim = cic;


% VOLUME FRACTIONS
%-------------------------------------------------------------------------
% Extravascular bone material | tildeflac defined in main file |
rhocol   = 1.42 ;
rhowater = 1.0 ;
rhoHA    = 3.0 ;
ddry     = 1.09 ;
dmax     = 1.52 ;

% Extracellular bone density
rhoult = rhoHA * barfHA + rhocol * barfcol + rhowater * barfwater;

% Conversion to mass fractions
phiHAm = rhoHA ./ rhoult .* barfHA ;

% Step 3: Volumes before mineralization
% Volume change due to mineralization
VNMvm = 1 + (rhoHA / rhowater - 1) * barfHA ;
```

```
fwaterNM = (rhoHA/rhowater*barfHA + barfwater)./VNMvm ;
fcolNM   = barfcol./VNMvm ;

% Step 4: fibrils/extrafibrillar space in non mineralized tissue - use of
% the swelling rule for non mineralized tissue
% wWater-to-organic mass ratio:
R      = fwaterNM./ fcolNM * rhowater/rhocol;
% volume fraction of the fibrils
ffibNM = 1/0.88 * (dmax/ddry)^2*rhowater./(R*rhocol + rhowater);
fefNM  = 1 - ffibNM ;

% Volume fraction of collagen inside the fibrils
tildefcolNM = 0.88*(ddry/dmax)^2 ;

% Diffraction spacing in the non mineralized state
dwNM  = dmax ;

% Mass density of the non mineralized fibrils
rhotissuNM = rhowater./(R*rhocol + rhowater)*(rhocol - rhowater) +rhowater;

% Volume fraction of the fibrils / extrafibrillar space in the mineralized
% tissue
barffib = 1 - barfef ;

% Volume fractions extrafibrillar space; Eq.(37), (39)
phiHAef  = (1-barffib)/(1-barfcol);
checkfHA = phiHAef*barfHA/barfef;
checkfic = 1-checkfHA;

% Volume fractions fibril; Eq.(38)
brevefHA     = barfHA*(1-phiHAef)/barffib;
brevefwetcol = 1-brevefHA;

% Volume fractions wet collagen; CORRECTED
circlefcol = barfcol/(barffib*brevefwetcol);
circlefuw  = 1-circlefcol;


% HOMOGENIZATION
%-------------------------------------------------------------------------
% Homogenization of wet collagen
hom_wetcol_MT;

% Homogenization of fibrils
hom_fib_SCS;

% Homogenization of extrafibrillar matrix
hom_ef_needles;

% Homogenization of ultrastructure
hom_ultra_SCS;
```

C.7.2 Homogenization of wet collagen

```
% Created by: Claire Morin, 2012

% Mori-Tanaka-scheme, collagen matrix with cylindrical water inclusions
% needed variables: circlefuw, circlefcol

% Evaluate P-tensor for cyl. inclusions in transversely isotr. matrix
Pcyl_col = P_isotrans_cyl(ccol);

% Evaluate [I+P:(c-C0)]^-1 for uw
helpuw   = inv(I+Pcyl_col*(cim-ccol)); % cylindrical inclusions!!!

Acol     = inv(circlefcol*I + circlefuw*helpuw);

% Evaluate homogenized stiffness
cwetcol  = (circlefcol*ccol + circlefuw*cim*helpuw)*...
           inv(circlefcol*I + circlefuw*helpuw);
```

C.7.3 Homogenization of fibrils

```
% Created by: Claire Morin, 2012

% Self-consistent-scheme:
% wetcol=cylindrical, transversely isotropic inclusions
% HA=isotropic, cylindrical inclusions

% Start with cwetcol as the C0-matrix
C0=cwetcol;
C0_old=0;

% Iteration for calculation of self-consistent stiffness
%-------------------------------------------------------------------------
while abs((norm(C0)-norm(C0_old))/norm(C0))>0.000001

% Evaluate P-tensor for spherical inclusions in transversely isotr. matrix
Psph_fib   = P_isotrans_sph(C0);

% Evaluate P-tensor for cyl. inclusions in transversely isotr. matrix
Pcyl_fib   = P_isotrans_cyl(C0);

% Evaluate [I+P:(c-C0)]^-1 for wetcol
helpwetcol = inv(I+Pcyl_fib*(cwetcol-C0));

% Evaluate [I+P:(c-C0)]^-1 for HA
helpHAfib  = inv(I+Psph_fib*(cHA-C0));

% Homogenization
cfib       = (brevefwetcol*cwetcol*helpwetcol + brevefHA*cHA*helpHAfib)*...
              inv(brevefwetcol*helpwetcol + brevefHA*helpHAfib);
C0_old     = C0;
C0         = cfib;
end

Awetcol    = helpwetcol*inv(brevefwetcol*helpwetcol + brevefHA*helpHAfib);
```

C.7.4 Homogenization of extrafibrillar space

```
% created by: Claire Morin, 2012

% Self-consistent-scheme:
% HA=isotropic, uniformly distributed needles
% uw=sph. water-filled pores

% Start with Mori-Tanaka as the C0-matrix
Psph=P_iso_sph(cHA,J,K);

C0=checkfHA*cHA*inv(checkfHA*I+checkfic*inv(I+Psph*(cic-cHA)));
C0_old=0;

% Iteration for calculation of self-consistent stiffness
%--------------------------------------------------------------------------
while abs((norm(C0)-norm(C0_old))/norm(C0))>0.00001
% CONTRIBUTION OF NEEDLES

% Local and global coordinates initiation
help_IPcHA = zeros(6,6);
helpic     = zeros(6,6);

% Stroud's integration formulae
weight = 1/15;
r      = 1/2;
s      = (sqrt(5)+1)/4;
t      = (sqrt(5)-1)/4;

vector_cos_theta         = [t t t t s s s s r r r r 0 0 1];
vector_sin_theta_sin_phi = [+s -s +s -s +r -r +r -r +t -t +t -t 0 1 0];
vector_sin_theta_cos_phi = [+r +r -r -r +t +t -t -t +s +s -s -s 1 0 0];

for r=1:15
    coor1 = vector_sin_theta_cos_phi(r);
    coor2 = vector_sin_theta_sin_phi(r);
    coor3 = vector_cos_theta(r);

 % Evaluate P-tensor for oriented cylinders in anisotropic matrix
 Pcyl_HA  = P_iso_cyl(coor1,coor2,coor3,C0,J);

 % Calculation in global base
 % Evaluate [I+P:(cHA-C0)]^-1 for solid phase (HA)
 % Evaluate cHA:[I+P:(cHA-C0)]^-1 for solid phase (HA)
 A1         = inv(I+Pcyl_HA*(cHA-C0));
 help_IPcHA = help_IPcHA + weight*A1;
end

% CONTRIBUTION OF PORES
% Evaluate P-tensor for spherical inclusions in anisotropic matrix
```

```
Psph_ef     = P_iso_sph(C0,J,K);
% Evaluate [I+P:(c-C0)]^-1 for pores (without integration)
helpic      = inv(I+Psph_ef*(cic-C0));

cef         = (checkfHA*cHA*help_IPcHA + checkfic*cic*helpic)*...
               inv(checkfHA*help_IPcHA + checkfic*helpic);
C0_old      = C0;
C0          = cef;
end   % next iteration step (while loop)

PHA     = cell(max_fam_theta,max_fam_phi);
AHA_inf = cell(max_fam_theta,max_fam_phi);
helpHA  = zeros(6,6);
APHA    = zeros(6,6);

for kk  = 1:max_fam_theta
    for ll = 1:max_fam_phi
    coor1  = sin(vector_theta_fam_i(kk))*cos(vector_phi_fam_i(ll));
    coor2  = sin(vector_theta_fam_i(kk))*sin(vector_phi_fam_i(ll));
    coor3  = cos(vector_theta_fam_i(kk));
        PHA(kk,ll)     = {P_iso_cyl(coor1,coor2,coor3,C0,J)};
        AHA_inf(kk,ll) = {inv(I+cell2mat(PHA(kk,ll))*(cHA-cef))};
        helpHA = helpHA + cell2mat(AHA_inf(kk,ll))*...
                    sin(vector_theta_fam_i(kk))*incr_theta*incr_phi/(4*pi);
        APHA = APHA + cell2mat(AHA_inf(kk,ll))*cell2mat(PHA(kk,ll))*...
                sin(vector_theta_fam_i(kk))*incr_theta*incr_phi/(4*pi);
    end
end

helpHA  = inv(checkfHA*helpHA + checkfic*helpic);
AP      = checkfHA*APHA + checkfic*helpic*Psph_ef ;
DCAP    = inv(checkfHA*(cef-cHA)*APHA+checkfic*(cef-cic)*helpic*Psph_ef);
```

C.7.5 Homogenization of ultrastructure

```
% Created by: Claire Morin, 2012

% Self-consistent-scheme: ef=matrix, fib = inclusions

% Start with cwetcol as the C0-matrix
C0=cef;
C0_old=0;

% Iteration for calculation of self-consistent stiffness
%-------------------------------------------------------------------------
while abs((norm(C0)-norm(C0_old))/norm(C0))>0.000001

% Evaluate P-tensor for cyl. inclusions in transversely isotr. matrix
Pcyl_ef  = P_isotrans_cyl(C0);

% Evaluate [I+P:(c-C0)]^-1 for the fibrils
helpfib  = inv(I+Pcyl_ef*(cfib-C0));

% Evaluate [I+P:(c-C0)]^-1 for the extrafibrillar space
helpef   = inv(I+Pcyl_ef*(cef-C0));

% Homogenization
cultra   = (barffib*cfib*helpfib+barfef*cef*helpef)*...
            inv(barffib*helpfib+barfef*helpef);
C0_old   = C0;
C0       = cultra;
end

Aef      = helpef * inv(barfef*helpef + barffib*helpfib);
Afib     = helpfib* inv(barfef*helpef + barffib*helpfib);
```

C.8 Color images for the maps of f_{HA} (sham and OVX rats)

```
clear all; close all;


load('import_images_GV_healthy.mat', 'GV_threshold', 'GV_bone')
load('Material_properties_sham_neu.mat', 'f_HA_h')

% Specification for OVX rat 6
GV_thr      = GV_threshold(6)
GV_bone     = GV_bone(6)
f_HA        = f_HA_h(6,:)

% Image paths
image_path  = 'C:\Users\Patricia\Documents\Studium\Diplomarbeit\GrI_SHAM\*.tif'
folder_path = 'C:\Users\Patricia\Documents\Studium\Diplomarbeit\GrI_SHAM\'
fpath       = 'C:\Users\Patricia\Documents\Studium\Diplomarbeit\Figures\'
images      = dir(image_path);
num_images  = length(images);

% Specifications for fHA
f_HA_min    = min(f_HA((GV_thr+1):256)); % minimum of fHA in bone tissue
f_HA_max    = max(f_HA((GV_thr+1):256)); % maximum of fHA in bone tissue
range       = f_HA_max - f_HA_min;       % range of fHA in bone tissue
x           = 254/range                  % factor for nu13
f_HA_round  = round(f_HA*x)              % round to whole numbers

% Define new values for image matrix (+1 ... so that minimum value is not 0)
f_HA_new    = f_HA_round+1 - min(f_HA_round((GV_thr+1):256))*ones(1,256)
f_HAnew_min = min(f_HA_new((GV_thr+1):256));
f_HAnew_max = max(f_HA_new((GV_thr+1):256));

% Loop over images
for z = 1:num_images
    filename         = [num2str(z) '.tif'];
    s                = ([folder_path filename]);

    % Imread images
    slice            = imread(s);
    dim_x            = size(slice,1);
    dim_y            = size(slice,2);
    data2D           = zeros(dim_x, dim_y, 'uint16');
    data2D(:,:)      = double(uint16(slice));

    % Replace grey values from image matrix with nu13(GV)
    data2D           = f_HA_new(data2D+1); % shift index (there is no index 0)
    data2D(data2D<1) = 0;

    % Define colormap
    maxVal           = max(data2D(:));
```

```
    minVal           = 1;
    range            = maxVal - minVal;
    map              = jet(range);
    cmap             = [zeros(minVal,3); jet(range)];

    % Create colorbar to mark most frequently occurring fHA
%     hcb            = colorbar;
%     set(hcb, 'YTick', [f_HA_new(GV_bone+1)]);
%     imshow(data2D,colormap(cmap));

    % Imwrite images
    imwrite(data2D, colormap(cmap), [num2str(fpath), num2str(z),'.tiff'])
    disp(['saved ',num2str(z),'/',num2str(num_images)])
end
```

```
clear all; close all;

load('import_images_GV_ovariectomized.mat', 'GV_threshold', 'GV_bone')
load('Material_properties_OVX_neu.mat', 'f_HA_o')

% Specification for OVX rat 6
GV_thr      = GV_threshold(6)
GV_bone     = GV_bone(6)
f_HA        = f_HA_o(6,:)

% Image paths
image_path  = 'C:\Users\Patricia\Documents\Studium\Diplomarbeit\GrII_OVX\*.tif'
folder_path = 'C:\Users\Patricia\Documents\Studium\Diplomarbeit\GrII_OVX\'
fpath       = 'C:\Users\Patricia\Documents\Studium\Diplomarbeit\Figures\'
images      = dir(image_path);
num_images  = length(images);

% Specifications for fHA
f_HA_min    = min(f_HA((GV_thr+1):256)); % minimum of fHA in bone tissue
f_HA_max    = max(f_HA((GV_thr+1):256)); % maximum of fHA in bone tissue
range       = f_HA_max - f_HA_min;       % range of fHA in bone tissue
x           = 254/range                  % factor for nu13
f_HA_round  = round(f_HA*x)              % round to whole numbers

% Define new values for image matrix (+1 ... so that minimum value is not 0)
f_HA_new    = f_HA_round+1 - min(f_HA_round((GV_thr+1):256))*ones(1,256)
f_HAnew_min = min(f_HA_new((GV_thr+1):256));
f_HAnew_max = max(f_HA_new((GV_thr+1):256));

% Loop over images
for z = 1:num_images
    filename         = [num2str(z) '.tif'];
    s                = ([folder_path filename]);

    % Imread images
    slice            = imread(s);
    dim_x            = size(slice,1);
    dim_y            = size(slice,2);
    data2D           = zeros(dim_x, dim_y, 'uint16');
    data2D(:,:)      = double(uint16(slice));

    % Replace grey values from image matrix with nu13(GV)
    data2D           = f_HA_new(data2D+1); % shift index (there is no index 0)
    data2D(data2D<1) = 0;

    % Define colormap
    maxVal           = max(data2D(:));
    minVal           = 1;
    range            = maxVal - minVal;
    map              = jet(range);
    cmap             = [zeros(minVal,3); jet(range)];
```

```
    % Create colorbar to mark most frequently occurring fHA
%     hcb            = colorbar;
%     set(hcb, 'YTick', [f_HA_new(GV_bone+1)]);
%     imshow(data2D,colormap(cmap));

    % Imwrite images
    imwrite(data2D,colormap(cmap), [num2str(fpath), num2str(z),'.tiff'])
    disp(['saved ',num2str(z),'/',num2str(num_images)])
end
```

C.9 Color images for the maps of E_1 (sham and OVX rats)

```
clear all; close all;

load('import_images_GV_healthy.mat', 'GV_threshold', 'GV_bone')
load('Material_properties_sham_neu.mat', 'E1')

% Specification for sham rat 6
GV_thr      = GV_threshold(6)
GV_bone     = GV_bone(6)
E1          = E1(6,:)

% Image paths
image_path  = 'C:\Users\Patricia\Documents\Studium\Diplomarbeit\GrI_SHAM\*.tif'
folder_path = 'C:\Users\Patricia\Documents\Studium\Diplomarbeit\GrI_SHAM\'
fpath       = 'C:\Users\Patricia\Documents\Studium\Diplomarbeit\Figures\'
images      = dir(image_path);
num_images  = length(images);

% Specifications for E1
E1_min      = min(E1((GV_thr+1):256)); % minimum of E1 in bone tissue
E1_max      = max(E1((GV_thr+1):256)); % maximum of E1 in bone tissue
range       = E1_max - E1_min;         % range of E1 in bone tissue
x           = 254/range;               % factor for E1
E1_round    = round(E1*x);             % round to whole numbers

% Define new values for image matrix (+1 ... so that minimum value is not 0)
E1_new      = E1_round+1 - min(E1_round((GV_thr+1):256))*ones(1,256);
E1new_min   = min(E1_new((GV_thr+1):256));
E1new_max   = max(E1_new((GV_thr+1):256));

% Loop over images
for z= 1: num_images
    filename         = [num2str(z) '.tif'];
    s                = ([folder_path filename]);

    % Imread images
    slice            = imread(s);
    dim_x            = size(slice,1);
    dim_y            = size(slice,2); %
    data2D           = zeros(dim_x, dim_y, 'uint16');
    data2D(:,:)      = double(uint16(slice));

    % Replace grey values from image matrix with E1(GV)
    data2D           = E1_new(data2D+1); % shift index (there is no index 0)
    data2D(data2D<1) = 0;

    % Define colormap
    maxVal           = max(data2D(:));
    minVal           = 1;
```

```
    range             = maxVal - minVal;
    map               = jet(range);
    cmap              = [zeros(minVal,3); jet(range)];

    % Create colorbar to mark most frequently occurring E1
%     hcb             = colorbar;
%     set(hcb, 'YTick', [E1_new(GV_bone+1)]);
%     imshow(data2D,colormap(cmap));

    % Imwrite images
    imwrite(data2D, colormap(cmap), [num2str(fpath), num2str(z),'.tiff'])
    disp(['saved ',num2str(z),'/',num2str(num_images)])
end
```

```
clear all; close all;

load('import_images_GV_ovariectomized.mat', 'GV_threshold', 'GV_bone')
load('Material_properties_OVX_neu.mat', 'E1')

% Specification for OVX rat 6
GV_thr      = GV_threshold(6)
GV_bone     = GV_bone(6)
E1          = E1(6,:)

% Image paths
image_path  = 'C:\Users\Patricia\Documents\Studium\Diplomarbeit\GrII_OVX\*.tif'
folder_path = 'C:\Users\Patricia\Documents\Studium\Diplomarbeit\GrII_OVX\'
fpath       = 'C:\Users\Patricia\Documents\Studium\Diplomarbeit\Figures\'
images      = dir(image_path);
num_images  = length(images);

% Specifications for E1
E1_min      = min(E1((GV_thr+1):256)); % minimum of E1 in bone tissue
E1_max      = max(E1((GV_thr+1):256)); % maximum of E1 in bone tissue
range       = E1_max - E1_min;         % range of E1 in bone tissue
x           = 254/range;               % factor for E1
E1_round    = round(E1*x);             % round to whole numbers

% Define new values for image matrix (+1 ... so that minimum value is not 0)
E1_new      = E1_round+1 - min(E1_round((GV_thr+1):256))*ones(1,256);
E1new_min   = min(E1_new((GV_thr+1):256));
E1new_max   = max(E1_new((GV_thr+1):256));

% Loop over images
for z = 1:num_images
    filename         = [num2str(z) '.tif'];
    s                = ([folder_path filename]);

    % Imread images
    slice            = imread(s);
    dim_x            = size(slice,1);
    dim_y            = size(slice,2);
    data2D           = zeros(dim_x, dim_y, 'uint16');
    data2D(:,:)      = double(uint16(slice));

    % Replace grey values from image matrix with E1(GV)
    data2D           = E1_new(data2D+1); % shift index (there is no index 0)
    data2D(data2D<1) = 0;

    % Define colormap
    maxVal           = max(data2D(:));
    minVal           = 1;
    range            = maxVal - minVal;
    map              = jet(range);
    cmap             = [zeros(minVal,3); jet(range)];
```

```
    % Create colorbar to mark most frequently occurring E1
%     hcb            = colorbar;
%     set(hcb, 'YTick', [E1_new(GV_bone+1)]);
%     imshow(data2D, colormap(cmap));

    % Imwrite images
    imwrite(data2D, colormap(cmap), [num2str(fpath), num2str(z),'.tiff'])
    disp(['saved ',num2str(z),'/',num2str(num_images)])
end
```

C.10 Color images for the maps of E_3 (sham and OVX rats)

```
clear all; close all;

load('import_images_GV_healthy.mat', 'GV_threshold', 'GV_bone')
load('Material_properties_sham_neu.mat', 'E3')

% Specification for sham rat 6
GV_thr      = GV_threshold(6)
GV_bone     = GV_bone(6)
E3          = E3(6,:)

% Image paths
image_path  = 'C:\Users\Patricia\Documents\Studium\Diplomarbeit\GrI_SHAM\*.tif'
folder_path = 'C:\Users\Patricia\Documents\Studium\Diplomarbeit\GrI_SHAM\'
fpath       = 'C:\Users\Patricia\Documents\Studium\Diplomarbeit\Figures\'
images      = dir(image_path);
num_images  = length(images);

% Specifications for E1
E3_min      = min(E3((GV_thr+1):256)); % minimum of E3 in bone tissue
E3_max      = max(E3((GV_thr+1):256)); % maximum of E3 in bone tissue
range       = E3_max - E3_min;         % range of E3 in bone tissue
x           = 254/range                % factor for E3
E3_round    = round(E3*x)              % round to whole numbers

% Define new values for image matrix (+1 ... so that minimum value is not 0)
E3_new      = E3_round+1 - min(E3_round((GV_thr+1):256))*ones(1,256);
E3new_min   = min(E3_new((GV_thr+1):256));
E3new_max   = max(E3_new((GV_thr+1):256));

% Loop over images
for z = 1:num_images
    filename         = [num2str(z) '.tif'];
    s                = ([folder_path filename]);

    % Imread images
    slice            = imread(s);
    dim_x            = size(slice,1);
    dim_y            = size(slice,2);
    data2D           = zeros(dim_x, dim_y, 'uint16');
    data2D(:,:)      = double(uint16(slice));

    % Replace grey values from image matrix with E3(GV)
    data2D           = E3_new(data2D+1); % shift index (there is no index 0)
    data2D(data2D<1) = 0;

    % Define colormap
    maxVal           = max(data2D(:));
    minVal           = 1;
```

```
    range             = maxVal - minVal;
    map               = jet(range);
    cmap              = [zeros(minVal,3); jet(range)];

    % Create colorbar to mark most frequently occurring E3
%     hcb             = colorbar;
%     set(hcb, 'YTick', [E3_new(GV_bone+1)]);
%     imshow(data2D, colormap(cmap));

    % Imwrite images
    imwrite(data2D, colormap(cmap), [num2str(fpath), num2str(z),'.tiff'])
    disp(['saved ',num2str(z),'/',num2str(num_images)])
end
```

```
clear all; close all;

load('import_images_GV_ovariectomized.mat', 'GV_threshold', 'GV_bone')
load('Material_properties_OVX_neu.mat', 'E3')

% Specification for OVX rat 6
GV_thr      = GV_threshold(6)
GV_bone     = GV_bone(6)
E3          = E3(6,:)

% Image paths
image_path  = 'C:\Users\Patricia\Documents\Studium\Diplomarbeit\GrII_OVX\*.tif'
folder_path = 'C:\Users\Patricia\Documents\Studium\Diplomarbeit\GrII_OVX\'
fpath       = 'C:\Users\Patricia\Documents\Studium\Diplomarbeit\Figures\'
images      = dir(image_path);
num_images  = length(images);

% Specifications for E3
E3_min      = min(E3((GV_thr+1):256)); % minimum of E3 in bone tissue
E3_max      = max(E3((GV_thr+1):256)); % maximum of E3 in bone tissue
range       = E3_max - E3_min;         % range of E3 in bone tissue
x           = 254/range;               % factor for E3
E3_round    = round(E3*x);             % round to whole numbers

% Define new values for image matrix (+1 ... so that minimum value is not 0)
E3_new      = E3_round+1-min(E3_round((GV_thr+1):256))*ones(1,256);
E3new_min   = min(E3_new((GV_thr+1):256));
E3new_max   = max(E3_new((GV_thr+1):256));

% Loop over images
for z = 1:num_images
    filename         = [num2str(z) '.tif'];
    s                = ([folder_path filename]);

    % Imread images
    slice            = imread(s);
    dim_x            = size(slice,1);
    dim_y            = size(slice,2);
    data2D           = zeros(dim_x, dim_y, 'uint16');
    data2D(:,:)      = double(uint16(slice));

    % Replace grey values from image matrix with E3(GV)
    data2D           = E3_new(data2D+1); % shift index (there is no index 0)
    data2D(data2D<1) = 0;

    % Define colormap
    maxVal           = max(data2D(:));
    minVal           = 1;
    range            = maxVal-minVal;
    map              = jet(range);
    cmap             = [zeros(minVal,3); jet(range)];
```

```
    % Create colorbar to mark most frequently occurring E3
%     hcb            = colorbar;
%     set(hcb, 'YTick' , [E3_new(GV_bone+1)]);
%     imshow(data2D, colormap(cmap));

    % Imwrite images
    imwrite(data2D, colormap(cmap), [num2str(fpath), num2str(z),'.tiff'])
    disp(['saved ',num2str(z),'/',num2str(num_images)])
end
```

C.11 Color images for the maps of G_{12} (sham and OVX rats)

```
clear all; close all;

load('import_images_GV_healthy.mat', 'GV_threshold', 'GV_bone')
load('Material_properties_sham_neu.mat', 'G12')

% Specification for sham rat 6
GV_thr      = GV_threshold(6)
GV_bone     = GV_bone(6)
G12         = G12(6,:)

% Image paths
image_path  = 'C:\Users\Patricia\Documents\Studium\Diplomarbeit\GrI_SHAM\*.tif'
folder_path = 'C:\Users\Patricia\Documents\Studium\Diplomarbeit\GrI_SHAM\'
fpath       = 'C:\Users\Patricia\Documents\Studium\Diplomarbeit\Figures\'
images      = dir(image_path);
num_images  = length(images);

% Specifications for G12
G12_min     = min(G12((GV_thr+1):256)); % minimum of G12 in bone tissue
G12_max     = max(G12((GV_thr+1):256)); % maximum of G12 in bone tissue
range       = G12_max - G12_min;        % range of G12 in bone tissue
x           = 254/range;                % factor for G12
G12_round   = round(G12*x)              % round to whole numbers

% Define new values for image matrix (+1 ... so that minimum value is not 0)
G12_new     = G12_round+1 - min(G12_round((GV_thr+1):256))*ones(1,256);
G12new_min  = min(G12_new((GV_thr+1):256));
G12new_max  = max(G12_new((GV_thr+1):256));

% Loop over image
for z = 1:num_images
    filename         = [num2str(z) '.tif'];
    s                = ([folder_path filename]);

    % Imread images
    slice            = imread(s);
    dim_x            = size(slice,1);
    dim_y            = size(slice,2);
    data2D           = zeros(dim_x, dim_y, 'uint16');
    data2D(:,:)      = double(uint16(slice));

    % Replace grey values from image matrix with G12(GV)
    data2D           = G12_new(data2D+1); % shift index (there is no index 0)
    data2D(data2D<1) = 0;

    % Define colormap
```

```
    maxVal           = max(data2D(:));
    minVal           = 1;
    range            = maxVal - minVal;
    map              = jet(range);
    cmap             = [zeros(minVal,3); jet(range)];

    % Create colorbar to mark most frequently occurring G12
%     hcb            = colorbar;
%     set(hcb, 'YTick', [G12_new(GV_bone+1)]);
%     imshow(data2D, colormap(cmap));

    % Imwrite images
    imwrite(data2D, colormap(cmap), [num2str(fpath), num2str(z),'.tiff'])
    disp(['saved ',num2str(z),'/',num2str(num_images)])
end
```

```
clear all; close all;

load('import_images_GV_ovariectomized.mat', 'GV_threshold', 'GV_bone')
load('Material_properties_OVX_neu.mat', 'G12')

% Specification for OVX rat 6
GV_thr      = GV_threshold(6)
GV_bone     = GV_bone(6)
G12         = G12(6,:)

% Image paths
image_path  = 'C:\Users\Patricia\Documents\Studium\Diplomarbeit\GrII_OVX\*.tif'
folder_path = 'C:\Users\Patricia\Documents\Studium\Diplomarbeit\GrII_OVX\'
fpath       = 'C:\Users\Patricia\Documents\Studium\Diplomarbeit\Figures\'
images      = dir(image_path);
num_images  = length(images);

% Specifications for G12
G12_min     = min(G12((GV_thr+1):256)); % minimum of G12 in bone tissue
G12_max     = max(G12((GV_thr+1):256)); % maximum of G12 in bone tissue
range       = G12_max - G12_min;        % range of G12 in bone tissue
x           = 254/range;                % factor for G12
G12_round   = round(G12*x);             % round to whole numbers

% Define new values for image matrix (+1 ... so that minimum value is not 0)
G12_new     = G12_round+1 - min(G12_round((GV_thr+1):256))*ones(1,256);
G12new_min  = min(G12_new((GV_thr+1):256));
G12new_max  = max(G12_new((GV_thr+1):256));

% Loop over the images
for z = 1:num_images
    filename         = [num2str(z) '.tif'];
    s                = ([folder_path filename]);

    % Imread images
    slice            = imread(s);
    dim_x            = size(slice,1);
    dim_y            = size(slice,2);
    data2D           = zeros(dim_x,dim_y,'uint16');
    data2D(:,:)      = double(uint16(slice));

    % Replace grey values from image matrix with G12(GV)
    data2D           = G12_new(data2D+1); % shift index (there is no index 0)
    data2D(data2D<1) = 0;

    % Define colormap
    maxVal           = max(data2D(:));
    minVal           = 1;
    range            = maxVal - minVal;
    map              = jet(range);
    cmap             = [zeros(minVal,3); jet(range)];
```

```
    % Create colorbar to mark most frequently occurring G12
%     hcb            = colorbar;
%     set(hcb, 'YTick', [G12_new(GV_bone+1)]);
%     imshow(data2D, colormap(cmap));

    % Imwrite images
    imwrite(data2D, colormap(cmap), [num2str(fpath), num2str(z),'.tiff'])
    disp(['saved ',num2str(z),'/',num2str(num_images)])
end
```

C.12 Color images for the maps of ν_{12} (sham and OVX rats)

```
clear all; close all;

load('import_images_GV_healthy.mat', 'GV_threshold', 'GV_bone')
load('Material_properties_sham_neu.mat', 'nu12')

% Specification for sham rat 6
GV_thr      = GV_threshold(6)
GV_bone     = GV_bone(6)
nu12        = nu12(6,:)

% Image paths
image_path  = 'C:\Users\Patricia\Documents\Studium\Diplomarbeit\GrI_SHAM\*.tif'
folder_path = 'C:\Users\Patricia\Documents\Studium\Diplomarbeit\GrI_SHAM\'
fpath       = 'C:\Users\Patricia\Documents\Studium\Diplomarbeit\Figures\'
images      = dir(image_path);
num_images  = length(images);

% Specifications for nu12
nu12_min    = min(nu12((GV_thr+1):256)); % minimum of nu12 in bone tissue
nu12_max    = max(nu12((GV_thr+1):256)); % maximum of nu12 in bone tissue
range       = nu12_max - nu12_min;       % range of nu12 in bone tissue
x           = 254/range;                 % factor for nu12
nu12_round  = round(nu12*x)              % round to whole numbers

% Define new values for image matrix (+1 ... so that minimum value is not 0)
nu12_new    = nu12_round+1 - min(nu12_round((GV_thr+1):256))*ones(1,256);
nu12new_min = min(nu12_new((GV_thr+1):256));
nu12new_max = max(nu12_new((GV_thr+1):256));

% Loop over images
for z = 1:num_images
    filename         = [num2str(z) '.tif'];
    s                = ([folder_path filename]);

    % Imread images
    slice            = imread(s);
    dim_x            = size(slice,1);
    dim_y            = size(slice,2);
    data2D           = zeros(dim_x, dim_y, 'uint16');
    data2D(:,:)      = double(uint16(slice));

    % Replace grey values from image matrix with nu12(GV)
    data2D           = nu12_new(data2D+1); % shift index (there is no index 0)
    data2D(data2D<1) = 0;

    % Define colormap
    maxVal           = max(data2D(:));
    minVal           = 1;
```

```
    range             = maxVal - minVal;
    map               = jet(range);
    cmap              = [zeros(minVal,3); jet(range)];

    % Create colorbar to mark most frequently occurring nu12
%     hcb             = colorbar;
%     set(hcb,'YTick',[nu12_new(GV_bone+1)]);
%     imshow(data2D,colormap(cmap));

    % Imwrite images
    imwrite(data2D, colormap(cmap), [num2str(fpath), num2str(z),'.tiff'])
    disp(['saved ',num2str(z),'/',num2str(num_images)])
end
```

```
clear all; close all;

load('import_images_GV_ovariectomized.mat', 'GV_threshold', 'GV_bone')
load('Material_properties_OVX_neu.mat', 'nu12')

% Specification for OVX rat 6
GV_thr      = GV_threshold(6)
GV_bone     = GV_bone(6)
nu12        = nu12(6,:)

% Image paths
image_path  = 'C:\Users\Patricia\Documents\Studium\Diplomarbeit\GrII_OVX\*.tif'
folder_path = 'C:\Users\Patricia\Documents\Studium\Diplomarbeit\GrII_OVX\'
fpath       = 'C:\Users\Patricia\Documents\Studium\Diplomarbeit\Figures\'
images      = dir(image_path);
num_images  = length(images);

% Specifications for nu12
nu12_min    = min(nu12((GV_thr+1):256)); % minimum of nu12 in bone tissue
nu12_max    = max(nu12((GV_thr+1):256)); % maximum of nu12 in bone tissue
range       = nu12_max - nu12_min;       % range of nu12 in bone tissue
x           = 254/range;                 % factor for nu12
nu12_round  = round(nu12*x);             % round to whole numbers

% Define new values for image matrix (+1 ... so that minimum value is not 0)
nu12_new    = nu12_round+1 - min(nu12_round((GV_thr+1):256))*ones(1,256)
nu12new_min = min(nu12_new((GV_thr+1):256));
nu12new_max = max(nu12_new((GV_thr+1):256));

% Loop over images
for z = 1:num_images
    filename         = [num2str(z) '.tif'];

    % Imread images
    s                = ([folder_path filename]);
    slice            = imread(s);
    dim_x            = size(slice,1);
    dim_y            = size(slice,2);
    data2D           = zeros(dim_x, dim_y, 'uint16');
    data2D(:,:)      = double(uint16(slice));

    % Replace grey values from image matrix with nu12(GV)
    data2D           = nu12_new(data2D+1); % shift index (there is no index 0)
    data2D(data2D<1) = 0;

    % Define colormap
    maxVal           = max(data2D(:));
    minVal           = 1;
    range            = maxVal - minVal;
    map              = jet(range);
    cmap             = [zeros(minVal,3); jet(range)];
```

```
    % Create colorbar to mark most frequently occurring nu12
%     hcb            = colorbar;
%     set(hcb, 'YTick', [nu12_new(GV_bone+1)]);
%     imshow(data2D, colormap(cmap));

    % Imwrite images
    imwrite(data2D, colormap(cmap), [num2str(fpath), num2str(z),'.tiff'])
    disp(['saved ',num2str(z),'/',num2str(num_images)])
end
```

C.13 Color images for the maps of ν_{13} (sham and OVX rats)

```
clear all; close all;

load('import_images_GV_healthy.mat', 'GV_threshold', 'GV_bone')
load('Material_properties_sham.mat', 'nu13')

% Specification for sham rat 6
GV_thr      = GV_threshold(6)
GV_bone     = GV_bone(6)
nu13        = nu13(6,:)

% Image paths
image_path  = 'C:\Users\Patricia\Documents\Studium\Diplomarbeit\GrI_SHAM\*.tif'
folder_path = 'C:\Users\Patricia\Documents\Studium\Diplomarbeit\GrI_SHAM\'
fpath       = 'C:\Users\Patricia\Documents\Studium\Diplomarbeit\Figures\'
images      = dir(image_path);
num_images  = length(images);

% Specifications for nu13
nu13_min    = min(nu13((GV_thr+1):256)); % minimum of nu13 in bone tissue
nu13_max    = max(nu13((GV_thr+1):256)); % maximum of nu13 in bone tissue
range       = nu13_max - nu13_min;       % range of nu13 in bone tissue
x           = 254/range;                 % factor for nu12
nu13_round  = round(nu13*x);             % round to whole numbers

% Define new values for image matrix (+1 ... so that minimum value is not 0)
nu13_new    = nu13_round+1 - min(nu13_round((GV_thr+1):256))*ones(1,256)
nu13new_min = min(nu13_new((GV_thr+1):256));
nu13new_max = max(nu13_new((GV_thr+1):256));

% Loop over images
for z = 1:num_images
    filename         = [num2str(z) '.tif'];
    s                = ([folder_path filename]);

    % Imread images
    slice            = imread(s);
    dim_x            = size(slice,1);
    dim_y            = size(slice,2);
    data2D           = zeros(dim_x, dim_y, 'uint16');
    data2D(:,:)      = double(uint16(slice));

    % Replace grey values from image matrix with nu13(GV)
    data2D           = nu13_new(data2D+1); % shift index (there is no index 0)
    data2D(data2D<1) = 0;

    % Define colormap
    maxVal           = max(data2D(:));
    minVal           = 1;
```

```
    range             = maxVal - minVal;
    map               = jet(range);
    cmap              = [zeros(minVal,3); jet(range)];

    % Create colorbar to mark most frequently occurring nu13
%     hcb             = colorbar;
%     set(hcb,'YTick',[nu13_new(GV_bone+1)]);
%     imshow(data2D,colormap(cmap));

    % Imwrite images
    imwrite(data2D,colormap(cmap), [num2str(fpath), num2str(z),'.tiff'])
    disp(['saved ',num2str(z),'/',num2str(num_images)])
end
```

```
clear all; close all;

load('import_images_GV_ovariectomized.mat', 'GV_threshold', 'GV_bone')
load('Material_properties_OVX_neu.mat', 'nu13')

% Specification for OVX rat 6
GV_thr      = GV_threshold(6)
GV_bone     = GV_bone(6)
nu13        = nu13(6,:)

% Image paths
image_path  = 'C:\Users\Patricia\Documents\Studium\Diplomarbeit\GrII_OVX\*.tif'
folder_path = 'C:\Users\Patricia\Documents\Studium\Diplomarbeit\GrII_OVX\'
fpath       = 'C:\Users\Patricia\Documents\Studium\Diplomarbeit\Figures\'
images      = dir(image_path);
num_images  = length(images);

% Specifications for nu13
nu13_min    = min(nu13((GV_thr+1):256)); % minimum of nu13 in bone tissue
nu13_max    = max(nu13((GV_thr+1):256)); % maximum of nu13 in bone tissue
range       = nu13_max - nu13_min;       % range of nu13 in bone tissue
x           = 254/range;                 % factor for nu13
nu13_round  = round(nu13*x);             % round to whole numbers

% Define new values for image matrix (+1 ... so that minimum value is not 0)
nu13_new    = nu13_round+1 - min(nu13_round((GV_thr+1):256))*ones(1,256)
nu13new_min = min(nu13_new((GV_thr+1):256));
nu13new_max = max(nu13_new((GV_thr+1):256));

% Loop over images
for z = 1:num_images
    filename         = [num2str(z) '.tif'];
    s                = ([folder_path filename]);

    % Imread images
    slice = imread(s);
    dim_x            = size(slice,1);
    dim_y            = size(slice,2);
    data2D           = zeros(dim_x, dim_y, 'uint16');
    data2D(:,:)      = double(uint16(slice));

    % Replace grey values from image matrix with nu13(GV)
    data2D           = nu13_new(data2D+1); % shift index (there is no index 0)
    data2D(data2D<1) = 0;

    % Define colormap
    maxVal           = max(data2D(:));
    minVal           = 1;
    range            = maxVal - minVal;
    map              = jet(range);
    cmap             = [zeros(minVal,3); jet(range)];
```

```
    % Create colorbar to mark most frequently occurring nu13
%     hcb            = colorbar;
%     set(hcb, 'YTick', [nu13_new(GV_bone+1)]);
%     imshow(data2D, colormap(cmap));

    % Imwrite images
    imwrite(data2D, colormap(cmap), [num2str(fpath), num2str(z),'.tiff'])
    disp(['saved ',num2str(z),'/',num2str(num_images)])
end
```

Bibliography

Anamula, S., Wehrli, S., Magland, J., Wright, A., Wehrli, F., 2010. Ultra-short echo-time MRI detects changes in bone mineralization and water content in OVX rat bone in response to alendronate treatment. Bone 46, 1391–1399.

Baca, V., Horak, Z., Mikulenka, P., Dzupa, V., 2008. Comparison of an inhomogeneous orthotropic and isotropic material models used for {fe} analyses. Medical Engineering & Physics 30 (7), 924 – 930.

Benveniste, Y., 1987. A new approach to the application of Mori-Tanaka's theory in composite materials. Mechanics of materials 6, 147–157.

Beyerer, J., Puente León, F., 2002. Die Radontransformation in der digitalen Bildverarbeitung. Automatisierungstechnik (at) 50, 472–480.

Blanchard, R., 2014. Multiscale coupling of X-ray physics and engineering mechanics, for supporting computed tomography-based orthopedics and bone remodeling. Ph.D. thesis, Institut für Mechanik der Werkstoffe und Strukturen, TU Wien, Begutachter/in(nen): Ch. Hellmich, M-C. Ho Ba Tho, Rigorosum: 02.09.2014.

Blanchard, R., Dejaco, A., Bongaers, E., Hellmich, C., 2013. Intravoxel bone micromechanics for microCT-based finite elements simulations. Journal of Biomechanics 46, 2710–2721.

Böcker, W., El Khassawna, T., Bauer, N., Brodsky, K., Weisweiler, D., Govindarajan, P., Schlewitz, G., Kampschulte, M., Dürselen, L., Thormann, U., Szalay, G., Schnettler, R., Langheinrich, A., Heiss, C., 2014. Short-term glucocorticoid treatment causes spinal osteoporosis in ovariectomized rats. European Spine Journal 23 (11), 2437–2448.

Bolz, R., Tuve, G. e., 1973. CRC handbook of tables for applied engineering science, 2nd Edition. Vol. Internet Version 2005. CRC Press, Cleveland, Ohio.

Borah, B., Gross, G., Dufresne, T., Smith, T., Cockman, M., Chmielewsky, P., Lundy, M., Hartke, J., Sod, W., 2001. Three-dimensional microimaging (MRµI and µCT), einite element modeling, and rapid prototyping provide unique insights into bone architecture in osteoporosis. The Anatomical Record 265 (2), 101–110.

Buckwalter, J., Glimcher, M., Cooper, R., Recker, R., 1995. Bone biology, Part i: Structure, blood supply, cells, matrix, and mineralization. The Journal of Bone and Joint Surgery 77-A, 1256–1275.

Buie, H., Campbell, G., Klinck, R., MacNeil, J., Boyd, S., 2007. Automatic segmentation of cortical and trabecular compartments based on a dual threshold technique for in vivo micro-CT bone analysis. Bone 41 (4), 505–515.

Campbell, G., Buie, H., Boyd, S., 2008. Signs of irreversible architectural changes occur early in the development of experimental osteoporosis as assessed by in vivo

micro-CT. Osteoporosis International 19, 1409–1419.

Cancedda, R., Cedola, A., Giuliani, A., Komlev, V., Lagomarsino, S., Mastrogiacomo, M., Peyrin, F., Rustichelli, F., 2007. Bulk and interface investigations of scaffolds and tissue-engineered bones by X-ray microtomography and X-ray microdiffraction. Biomaterials 28, 2505–2524, imaging Techniques for Biomaterials Characterization.

Clarke, B., 2008. Normal bone anatomy and physiology. Clinical Journal of the American Society of Nephrology 3 (3), 131–139.

Cong, A., Op Den Buijs, J., Dragomir-Daescu, D., 2011. In situ parameter identification of optimal density–elastic modulus relationships in subject-specific finite element models of the proximal femur. Medical Engineering & Physics 33 (2), 164–173.

Crawley, E., Evans, W., Owen, G., 1988. A theoretical analysis of the accuracy of single-energy CT bone-mineral measurements. Physics in Medicine and Biology 33 (10), 1113–1127.

Cusack, S., Miller, A., 1979. Determination of the elastic constants of collagen by Brillouin light scattering. Journal of Molecular Biology 135 (1), 39 – 51.

Czenek, A., Blanchard, R., Dejaco, A., Sigurjónsson, Ó., Örlygsson, G., Gargiulo, P., Hellmich, C., 2014. Quantitative intravoxel analyses of microct-scanned resorbing ceramic biomaterials - perspectives for computer-aided biomaterial design. Journal of Materials Research 29 (23), 2757–2772.

Dejaco, A., Komlev, V., Jaroszewicz, J., Swieszkowski, W., Hellmich, C., 2012. Micro CT-based multiscale elasticity of double-porous (pre-cracked) hydroxyapatite granules for regenerative medicine. Journal of Biomechanics 45 (6), 1068–1075.

Del Grosso, V., Mader, C., 1972. Speed of sound in pure water. Journal of the Acoustical Society of America 52 (5B), 1442–1446.

Donnelly, E., 2011. Methods for assessing bone quality: A review. Clinical Orthopaedics and Related Research 469 (8), 2128–2138.

Dormieux, L., Kondo, D., Ulm, F.-J., 2006. Microporomechanics. John Wiley & Sons, Ltd, Chichester, West Sussex, England.

Drugan, W., Willis, J., 1996. A micromechanics-based nonlocal constitutive equation and estimates of representative volume element size for elastic composites. Journal of the Mechanics and Physics of Solids 44 (4), 497–524.

Eastoe, J., 1955. The amino acid composition of mammalian collagen and gelatin. Biochemical Journal 61 (4), 589–600.

Fanti, P., Monier-Faugere, M., Geng, Z., Schmidt, J., Morris, P., Cohen, D., Malluche, H., 1998. The phytoestrogen genistein reduces bone loss in short-term ovariectomized rats. Osteoporosis International 8 (3), 274–281.

Francisco, J., Yu, Y., Oliver, R., Walsh, W., 2011. Relationship between age, skeletal site, and time post-ovariectomy on bone mineral and trabecular microarchitecture in rats. Journal of Orthopaedic Research 29 (2), 189–196.

Fritsch, A., Dejaco, A., Komlev, V., Swieszkowski, W., Jaroszewicz, J., Bongaers, E., Hellmich, C., 2011. Translation of CT data into voxel-specific micromechanics-based elasticity tensors. Micro-CT User Meeting, Abstract Book SkyScan, 2011, 108–112.

Fritsch, A., Dormieux, L., Hellmich, C., 2006. Porous polycrystals built up by uniformly and axisymmetrically oriented needles: homogenization of elastic properties. Comptes Rendus Mécanique 334 (3), 151–157.

Fritsch, A., Dormieux, L., Hellmich, C., Sanahuja, J., 2009a. Mechanical behavior of hydroxyapatite biomaterials: An experimentally validated micromechanical model for elasticity and strength. Journal of Biomedical Materials Research Part A 88 (1), 149–161.

Fritsch, A., Hellmich, C., 2007. 'Universal' microstructural patterns in cortical and trabecular, extracellular and extravascular bone materials: Micromechanics-based prediction of anisotropic elasticity. Journal of Theoretical Biology 244 (4), 597–620.

Fritsch, A., Hellmich, C., Dormieux, L., 2009b. Ductile sliding between mineral crystals followed by rupture of collagen crosslinks: Experimentally supported micromechanical explanation of bone strength. Journal of Theoretical Biology 260 (2), 230–252.

Genant, H., Engelke, K., Prevrhal, S., 2008. Advanced CT bone imaging in osteoporosis. Rheumatology 47 (4), iv9–iv16.

Gong, J., Arnold, J., Cohn, S., 1964. The density of organic and volatile and non-volatile inorganic components of bone. The Anatomical Record 149 (3), 319–324.

Govindarajan, P., Böcker, W., El Khassawna, T., Kampschulte, M., Schlewitz, G., Huerter, B., Sommer, U., Dürselen, L., Ignatius, A., Bauer, N. Szalay, G., Wenisch, S., Lips, K., Schnettler, R., Langheinrich, A., Heiss, C., 2014. Bone matrix, cellularity, and structural changes in a rat model with high-turnover osteoporosis induced by combined ovariectomy and a multiple-deficient diet. The American Journal of Pathology 184 (3), 765–777.

Hammett, F., 1925. A biochemical study of bone growth: I. Changes in the ash, organic matter and water during growth (mus norvegicus albinus). The Journal of Biological Chemistry 64 (2), 409–428.

Hellmich, C., Barthélémy, J.-F., Dormieux, L., 2004a. Mineral-collagen interactions in elasticity of bone ultrastructure-a continuum micromechanics approach. European Journal of Mechanics - A/Solids 23 (5), 783–810.

Hellmich, C., Kober, C., Erdmann, B., 2008. Micromechanics-based conversion

of CT data into anisotropic elasticity tensors, applied to FE simulations of a mandible. Annals of Biomedical Engineering 36 (1), 108–122.

Hellmich, C., Ulm, F.-J., 2002. Are mineralized tissues open crystal foams reinforced by crosslinked collagen?-some energy arguments. Journal of Biomechanics 35 (9), 1199–1212.

Hellmich, C., Ulm, F.-J., Dormieux, L., 2004b. Can the diverse elastic properties of trabecular and cortical bone be attributed to only a few tissue-independent phase properties and their interactions? Biomechanics and Modeling in Mechanobiology 2 (4), 219–238.

Hershey, A., 1954. The elasticity of an isotropic aggregate of anisotropic cubic crystals. Journal of Applied Mechanics 21, 236–240.

Hoegh-Andersen, P., Tankó, L., Andersen, T., Lundberg, C., Mo, J., Heegaard, A.-M., Delaissé, J.-M., Christgau, S., 2004. Ovariectomized rats as a model of postmenopausal osteoarthritis: validation and application. Arthritis Research & Therapy 6 (2), R169–R180.

Holdsworth, D., Thornton, M., 2002. Micro-CT in small animal and specimen imaging. Trends in Biotechnology 20 (8), 34–39.

Hubbell, J., Seltzer, S., 1996. Tables of X-ray mass attenuation coefficients and mass energy-absorption coefficients from 1 kev to 20 mev for elements z = 1 to 92 and 48 additional substances of dosimetric interest. U.S. Department of Commerce, National Institute of Standards and Technology (NIST), July 2004), `http://physics.nist.gov/PhysRefData/XrayMassCoef/cover.html`.

Jackson, D., Hawkes, D., 1981. X-ray attenuation coefficients of elements and mixtures. Physics Reports 70 (3), 169–233.

Jaecques, S., Van Oosterwyck, H., Muraru, L., Van Cleynenbreugel, T., De Smet, E., Wevers, M., Naert, I., Vander Sloten, J., 2004. Individualised, micro CT-based finite element modelling as a tool for biomechanical analysis related to tissue engineering of bone. Biomaterials 25 (9), 1683–1696, animal Models for Tissue Engineering Applications.

Jones, A., Arns, C., Sheppard, A., Hutmacher, D., Milthorpe, B., Knackstedt, M., 2007. Assessment of bone ingrowth into porous biomaterials using MICRO-CT. Biomaterials 28 (15), 2491 – 2504, imaging Techniques for Biomaterials Characterization.

Kalu, D., 1991. The ovariectomized rat model of postmenopausal bone loss. Bone and Mineral 15 (3), 175–192.

Kapadia, R., Stroup, G., Badger, A., Koller, B., Levin, J., Coatney, R., Dodds, R., Liang, X., Lark, M., Gowen, M., 1998. Applications of micro-CT and MR microscopy to study pre-clinical models of osteoporosis and osteoarthritis. Technology and health care 6 (5), 361–372.

Katz, E., Li, S.-T., 1973. Structure and function of bone collagen fibrils. Journal of Molecular Biology 80 (1), 1–15.

Katz, J., Ukraincik, K., 1971. On the anisotropic elastic properties of hydroxapatite. Journal of Biomechanics 4 (3), 221–227.

Kim, J. G., Lee, E., Kim, S. H., Whang, K. Y., Oh, S., Imm, J.-Y., 2009. Effects of a Lactobacillus casei 393 fermented milk product on bone metabolism in ovariectomised rats. International Dairy Journal 19 (11), 690–695.

Laib, A., Barou, O., Vico, L., Lafage-Proust, M., Alexandre, C., Rüegsegger, P., 2000. 3D micro-computed tomography of trabecular and cortical bone architecture with application to a rat model of immobilisation osteoporosis. Medical and Biological Engineering and Computing 38 (3), 326–332.

Landis, W., 1995. The strength of a calcified tissue depends in part on the molecular structure and organization of its constituent mineral crystals in their organic matrix. Bone 16 (5), 533–544.

Lees, S., 1987. Considerations regarding the structure of the mammalian mineralized osteoid from viewpoint of the generalized packing model. Connective Tissue Research 16 (4), 281–303.

Lees, S., 2003. Mineralization of type I collagen. Biophysical Journal 85 (1), 204–207.

Lesclous, P., Guez, D., Baroukh, B., Vignery, A., Saffar, J., 2004. Histamine participates in the early phase of trabecular bone loss in ovariectomized rats. Bone 34 (1), 91–99.

Liu, X., Li, C., Lu, W., Cai, W., Zheng, L., 2014. Skeletal site-specific response to ovariectomy in a rat model: change in bone density and microarchitecture. Clinical oral implants research, 204–207.

Lodish, H., Berk, A., Zipursky, S. L., Matsudaira, P., Baltimore, D., Darnell, J., 2000. Molecular Cell Biology, 4th Edition. W. H. Freeman, New York, Ch. 22.3, Collagen: The Fibrous Proteins of the Matrix, `http://www.ncbi.nlm.nih.gov/books/NBK21582/`.

Mori, T., Tanaka, K., 1973. Average stress in matrix and average elastic energy of materials with misfitting inclusions. Acta metallurgica 21 (5), 571– 574.

Morin, C., Hellmich, C., 2013. Mineralization-driven bone tissue evolution follows from fluid-to-solid phase transformations in closed thermodynamic systems. Journal of Theoretical Biology 335, 185–197.

Morin, C., Hellmich, C., 2014. A multiscale poromicromechanical approach to wave propagation and attenuation in bone. Ultrasonics 54 (5), 1251–1269.

Morin, C., Hellmich, C., Henits, P., 2013. Fibrillar structure and elasticity of hydrating collagen: A quantitative multiscale approach. Journal of Theoretical Biology 317, 384 – 393.

Müller, R., 2005. Long-term prediction of three-dimensional bone architecture in simulations of pre-, peri-and post-menopausal microstructural bone remodeling. Osteoporosis International 16 (2), 25–35.

Rachner, T., Khosla, S., Hofbauer, L., 2011. Osteoporosis: now and the future. The Lancet 377 (9773), 1276–1287.

Radon, J., 1917. Über die Bestimmung von Funktionen durch ihre Integralwerte längs gewisser Mannigfaltigkeiten. Berichte über die Verhandlungen der Königlich-Sächsischen Gesellschaft der Wissenschaften zu Leipzig. Mathematisch-Physische Klasse 69, 262–277.

Renders, G., Mulder, L., Langenbach, G., Van Ruijven, L., Van Eijden, T., 2008. Biomechanical effect of mineral heterogeneity in trabecular bone. Journal of Biomechanics 41 (13), 2793 – 2798.

Roschger, P., Paschalis, E., Fratzl, P., Klaushofer, K., 2008. Bone mineralization density distribution in health and disease. Bone 42 (3), 456–466.

Saito, M., Shiraishi, A., Ito, M., Sakai, S., Hayakawa, N., Mihara, M., Marumo, K., 2009. Comparison of effects of alfacalcidol and alendronate on mechanical properties and bone collagen cross-links of callus in the fracture repair rat model. Bone 46, 1170–1179.

Sambrook, P., Cooper, C., 2006. Osteoporosis. The Lancet 367 (9527), 2010–2018.

Schambach, S., Bag, S., Schilling, L., Groden, C., Brockmann, M., 2010. Application of micro-CT in small animal imaging. Methods 50 (1), 2–13.

Scheiner, S., Sinibaldi, R., Pichler, B., Komlev, V., Renghini, C., Vitale-Brovarone, C., Rustichelli, F., Hellmich, C., 2009. Micromechanics of bone tissue-engineering scaffolds, based on resolution error-cleared computer tomography. Biomaterials 30 (12), 2411–2419.

Searle, G., 1934. Experimental Physics. A selection of experiments., 1st Edition. Cambridge University Press, p279.

Skyscan, 2010. CTAn User's Guide, Version 1.10. Skycan NV, Kontich, Belgium, `www.skyscan.be`.

Tabor, Z., Latała, Z., 2014. 3D gray-level histomorphometry of trabecular bone-a methodological review. Image Analysis & Stereology 33 (1), 1–12.

Taleb-Ahmed, A., Dubois, P., Duquenoy, E., 2003. Analysis methods of CT-scan images for the characterization of the bone texture: First results. Pattern recognition letters 24 (12), 1971–1982.

Thompson, D., Simmons, H., Pirie, C., Ke, H., 1995. FDA Guidelines and animal models for osteoporosis. Bone 17 (4), 125–133.

Urist, M., DeLange, R., Finerman, G., 1983. Bone cell differentiation and growth factors. Science 220 (4598), 680–686.

Van Rietbergen, B., Müller, R., Ulrich, D., Rüegsegger, P., Huiskes, R., 1999. Tissue stresses and strain in trabeculae of a canine proximal femur can be quantified from computer reconstructions. Journal of Biomechanics 32 (2), 165–173.

Van Rietbergen, B., Weinans, H., Huiskes, R., Odgaard, A., 1995. A new method to determine trabecular bone elastic properties and loading using micromechanical finite-element models. Journal of Biomechanics 28 (1), 69–81.

Vuong, J., Hellmich, C., 2011. Bone fibrillogenesis and mineralization: Quantitative analyses and implications for tissue elasticity. Journal of Theoretical Biology 287, 115–130.

Wang, L., Orhii, P., Banu, J., Kalu, D., 2001. Effects of separate and combined therapy with growth hormone and parathyroid hormone on lumbar vertebral bone in aged ovariectomized osteopenic rats. Bone 28 (2), 202–207.

Wirtz, D., Schiffers, N., Pandorf, T., Radermacher, K., Weichert, D., Forst, R., 2000. Critical evaluation of known bone material properties to realize anisotropic FE-simulation of the proximal femur. Journal of Biomechanics 33 (10), 1325–1330.

Yang, Y., Zheng, X., Li, B., Jiang, S., Jiang, L., 2014. Increased activity of osteocyte autophagy in ovariectomized rats and its correlation with oxidative stress status and bone loss. Biochemical and Biophysical Research Communications 451 (1), 86–92.

Yosibash, Z., Trabelsi, N., Hellmich, C., 2008. Subject-specific p-FE analysis of the proximal femur utilizing micromechanics-based material properties. International Journal for Multiscale Computational Engineering 6 (5), 483–498.

Zaoui, A., 2002. Continuum micromechanics: survey. Journal of Engineering Mechanics 128 (8), 808–816.